# THE FIRST JOINT INTERNATIONAL CONFERENCE ON ASTROPHYSICS FOR YOUNG SCIENTISTS

October 3–7, 2017, Byurakan

Saint-Petersburg
Published by Peter the Great St.Petersburg Polytechnic University
2017

УДК 52.08,520,521,51-71
ББК 22.63

The First Joint International Conference on Astrophysics for Young Scientists: proceedings. – St.Petersburg: Published by Peter the Great St.Petersburg Polytechnic University, 2017. – 172 с.

The book of proceedings includes articles of contributed works of students and young scientists accepted for presentation at the international conference "The First Joint International Conference on Astrophysics for Young Scientists". Research works include results in the field of astrophysics, space technologies, radio astronomy, navigation systems and other space applications.

**ISBN 978-5-7422-5996-1**

# Section
# Astrophysics and Cosmology

## THE ORIGIN OF LIFE FROM THE ASTROPHYSICAL POINT OF VIEW

Yeghikyan, A.G.
Byurakan Astrophysical Observatory, Byurakan, Armenia
E-mail: ayarayeg@gmail.com

**Abstract:** The problem of the origin of life is discussed from the astrophysical point of view. Most biologists and geologists have believed up to the present time that Life originated on the Earth in some initial natural chemical pre-reactors, where a mixture of the water, ammonia, methane containing species and some other substances, under the influence of an energy source like, e.g. lightning, had turned into quite complex compounds such as amino acids and complex hydrocarbons. In fact, under conditions of the primordial Earth, it was not possible to obtain such pre-biological molecules by a-bio-chemical methods, as discussed in this paper. Instead, an astrophysical view of the problem of the origin of life on the Earth is proposed and it is recalled that the biological evolution on the Earth was preceded by the chemical evolution of complex chemical compounds, mostly under extraterrestrial conditions, where it is only possible to form optically active amino acids, sugars and hydrocarbons necessary for constructing the first pre-biomolecules.

**Keywords:** origin of life, chemical compounds in space, ice covers of dust grains, CR and UV induced radiation chemical polymerization of ices, chiral species.

### Introduction

Most biologists and geologists have believed up to the present time that Life originated on the Earth [1]. In fact, under conditions of the primordial Earth, it was not possible to obtain pre-biological molecules by a-bio-chemical methods, as discussed in this paper. The

origin of pre-life can be described in general terms as a kind of process of development from the simple to the complex, i.e. from simple chemical molecules to complex molecular aggregates. The case is that there is a generally accepted astrophysical point of view that a biological evolution on the Earth was preceded by a period of chemical evolution during which the formation and organization of pre-bio-organic compounds were accomplished – predominantly under extraterrestrial conditions. It should be evident that Life as we know it clearly originated in the same way in which everything originates, step by step. Let us discuss these steps of pre-biological evolution from the astrophysical point of view.

**Steps of pre-biological evolution**

Step 1: just the chemistry of simple molecules.

We limit our consideration by last 10 billion years when dust particles were abundant with gas to dust mass ratio of 100 (1000) to 1. At that time in interstellar molecular clouds behind the photo-dissociation region, the simplest but the most abundant molecular hydrogen $H_2$ might effectively originate on dust grain surfaces with the time-scale [2]

$$t(\mathrm{H_2}) = \frac{1.5 \cdot 10^9}{n}\ \mathrm{yr}\,,$$

that is in pre-stellar cores with $n \geq 10^6\ \mathrm{cm^{-3}}$, then $t(\mathrm{H_2}) \leq 1500\ \mathrm{yr}$. But under conditions of unshielded interstellar medium, molecules would be destroyed in [3]

$$t(\mathrm{photodiss.}) = \frac{1}{k_0(0)\ \mathrm{s^{-1}}} = \frac{10^9 - 10^{11}}{3 \cdot 10^7}\ \mathrm{yr} \cong 33 - 3300\ \mathrm{years}.$$

Thus, molecules might be accumulated only inside of clouds and proto-stellar disks. Almost 200 molecules have been detected up to 2017, and 61 molecules in other galaxies [4].

Step 2: dust and ice covers of dust grains.

Dust grains come now with SN ejections and AGB winds. Initial sizes of graphite and/or silicate cores were $\sim 0.01\ \mu$, on which $H_2O$, CO, $CO_2$, $CH_4$, $NH_3$, $CH_3OH$, HAC (hydrogenated amorphous carbon) and other icy mantles grew up to sizes of $\sim 0.1\ \mu$. Time-scales for dust growth in a dense cold medium [2] were:

$$t = \frac{3 \cdot 10^9}{n} \text{ years,}$$

which means a rapid growth in the star formation regions with pre-stellar clouds with $n \geq 10^6 \text{cm}^{-3}$ and $T \sim 10 - 20$ K, about in 3000 years.

Also the grain surface chemistry is very important for the origin of H, C, O, N-containing complex ices in the star formation regions [2, 3].

Step 3: complexing.

Why are ices important? The point is that complex species are more easily generated in the solid state of ice mantles of dust grains if ultraviolet (UV, 6–13.6 eV) and cosmic rays (CR, ≥ 1 MeV) radiation fields are available. A mixture of realistic ice analogues like $H_2O$:$CH_3OH$:$NH_3$:CO:$CH_4$ has produced heavy hydrocarbons (up to 30 atoms per molecule) and amino acids by UV and/or energetic particles processing in laboratory [5, 6 and references therein]. Also molecular symmetry may be broken easier in ices under molecular cloud conditions as compared with protoplanetary conditions [7]. UV- and CR-induced solid-phase radiation chemical polymerization (polycondensation) may produce complex species with time-scales about Kyrs ∼ Myrs depending on the duration of available processing. CR contribution known from laboratory experiments is as follows: complex aliphatic ≤ $C_{29}H_{60}$ and aromatic (PAH) ≤$C_{24}H_{12}$ (coronene) hydrocarbons have been synthesized in prebiotic simulation experiments by irradiation of solid $CH_4$ with 7 MeV protons and/or α-particles, [5, 6, 8, 9 and references therein], in short, the radiation chemical polycondensation of methane by MeV protons and α-particles. A radiation chemical yield of alkanes in such a process resulting in ≤ $C_{29}H_{60}$, is $Y \sim 1$ synth.mol /100 eV [6], and a monomer fraction converted to oligomer is $Q \sim Y \cdot D$ depending on irradiation dose $D$, $D_{\text{exper.}} \sim 6$ eV/molecule (0.3 eV/a.m.u.) [6, 8].

Also UV radiation induced chemical transformation of ices was revealed in experiments [5 and references therein]. A mixture of $H_2O$:$CH_3OH$:$NH_3$:CO (100:50:1:1), irradiated by far-UV, (at 15 K) resulted in $C_nH_m$ (n ≤ 22) hydrocarbons, and other complex species, like e.g. hexamethylenetetramine, HMT $C_6H_{12}N_4$ (very close to amino acids). Threshold doses in the experiments, for fluxes of about $3 \cdot 10^4$

photons/$cm^2$s (at 15 K), producing heavy hydrocarbons and HMT, were of $D_{exper.}$ ~ 25 eV/molecule ~ 1.4 eV/a.m.u [5].

Interestingly, glycolaldehyde and glycine ($C_2H_5O_2N$, 206.468 MHz) [4], were observed in hot molecular core (both were optically non-active). On the other hand, carbon containing complex species revealed in meteorites contain amino acids with enantiomeric excess, which were optically active [7, 9, 10 and references therein]!

Organics recycling in the Galaxy [11 and references therein] means, among other things, the following. Large molecules (nanoparticles like fullerens and polycyclic aromatic hydrocarbons, PAHs) originated in cold stellar outflows, scattered in the interstellar medium and then entered into molecular clouds. Molecules could also survive inside condensations in planetary nebulae evidencing the recycling of organics in the Galaxy, and showing, by the way, PAH and fullerens $C_{60}$ and $C_{70}$!

Step 4: "separation" first.

Chemically active droplets as a model for protocells on the early Earth are widely discussed and mean, in general, "membrane first" hypothesis which needs the lipid bilayer (lipids, pospholipids, etc.) [7, 10]. McCarthy and Calvin [12] were the first who mentioned about polyisoprenoid compounds as important ingredients to form such bilayers! Yeghikyan and co-workers [9, 14] discussed some details concerning creation in space and accumulation of such species on the Earth. Thus, "membranes first" hypothesis (in aqueous environment) is also connected to polyisoprenoid hydrocarbons suggested in [12] and highlights their role. One should conclude that isoprene ( ($C_5H_8$) -2-methyl-1,3-butadiene $CH_2=C(CH_3)-CH=CH_2$ ) and its derivatives play an important role as membrane forming subunits.

**Where do membrane making molecules come from?**

The surface of the newborn Earth was very hot (~800 K). The atmosphere was neutral ($CO_2+N_2$) so no direct polymerization/polycondensation was possible and also no Fischer-Tropsch synthesis above $C_{15}H_m$ might happen. There is widely accepted now that needful organics were delivered to the Earth by comets and large dust particles [9, 10, 14 and references therein].

Physical-chemical stratification in the protosolar disk revealed by models has shown that such comets and dust originated beyond the so called snow and tar lines that permits to suggest a following observational test for polyisoprenoids: the search of corresponding lines of solid polyisoprenoid hydrocarbons in the spectra of protostellar disks, that is vibrational lines of diene molecules in the range of 3.23–13.7 μm [13].

CR and VUV induced polycondensation of solid $CH_4$ followed with aliphatic heavy hydrocarbons up to $C_{29}H_{60}$ should be accounted as a key process of complexing. A probable aromatization due to VUV resulted in small PAH, e.g. $C_{24}H_{12}$ is also an important way to get species widely observed in space. Circumstellar disks show many predecessors of PAH with aliphatic bonds [14 and references therein].

**Basics of astrobiological scenarios concerning the origin of life on the Earth.**

A short summary of generally accepted scenarios is given below [7,9,10,14 and references therein].

The water for oceans was delivered by comets and dust around 4.5–3.8 Gyr ago (D/H is well agreed). The terrestrial primordial atmosphere which was also created by such a way was neutral ($CO_2$+$N_2$). Organics delivered to the Earth by comets and interstellar dust particles had already have contained chiral species because molecular symmetry could not be broken under terrestrial conditions. Comets impacting the Earth with grazing trajectories (with $\alpha \leq 5^0$, 2-3 % of all impacts) created the first biochemical reactors or „little warm ponds“. Life (on Earth) appeared 3.8 Gyr ago immediately after the cessation of the „heavy bombardment“ period.

Step 5: chiralization.

Homochirality is a key distinguisher of life and chiral molecules should be important "precursors" to first living organisms [7]. Chiral molecules older than the Earth itself have been spotted in meteors and comets. The most effective mechanism to get enantiomeric enhancement is enantiomer-selective photochemistry induced by circularly polarized light of 6–13.6 eV [7].

Terrestrial organisms use one enantiomer only. Protein synthesis, gene transcription and metabolism essentially depend on homochirality. A question is raised if Miller-type experiments ($CH_4$,

$NH_3$, $H_2O$, $H_2$ + Energy source resulting in complex species) are adequate. The answer is no! The point is that the terrestrial primitive atmosphere was not reduced (no $H_2$, $CH_4$ — no polymerization/condensation) and produced amino acids were racemic. So one should look for extraterrestrial conditions to get chiral species!

Now and again: the best way to get such complex molecules is grain surface reactions under appropriate irradiation of asymmetric agents. Astrobiologists now are urgently looking for such asymmetric agents for photoreactions. One may list corresponding advantage factors: circularly polarized VUV radiation, polarized electrons, magnetic fields, rotation, parity violation in weak interactions, surfaces of crystals (quartz) and clays (caolinit) [7]. Problems of seeding chirality and its amplification are also challenging.

So, a very important question should be "Where do prebiotic molecules come from?" Are they really from a natal cloud, or probably from a disk, or from other exoplanet? Astrophysicists need more precise observational and theoretical data to get first answers to such complicated questions.

**Conclusions**

Life on the Earth is the final product of a very long chemical evolution of matter, mainly under extraterrestrial conditions. This evolution started from the creation of the simplest molecules, survived under very hard conditions sometimes, condensed into dust when possible, began to be covered with ice and formed ice mantles of dust grains. Further, the radiation-chemical polymerization of a mixture of ices resulted in the formation of amino acids, sugars and hydrocarbons. It should be emphasized that these compounds should have been optically active, that distinguished living organisms from inanimate ones. Delivery of these substances before the birth of life on the Earth is a separate problem: most likely they were brought by comets, colliding with the Earth on grazing trajectories during the bombardment of the Earth between 4.5 and 3.8 billion years ago. There is the widely accepted point of view that Life on the Earth originated 3.8 Gyr ago [10].

This work was supported by the RA MES State Committee of Science (Armenia), in the frames of the research project № 15T-1C081.

**References**

1. Campbell, N., Rees, J., Urry, L. et al., Biology, Pearson Education, SF, 2010. pp.507-511.
2. Williams, D., Viti, S., Observational Molecular Astronomy, CUP. 2013. 192 pages
3. Yamamoto, S. Introduction to Astrochemistry, Springer. 2017. 293 pages
4. www.astro.uni-koeln.de/cdms/molecules
5. Yeghikyan, A. On dust irradiation in molecular clouds I UV doses // Astrophysics. 2009. 52, 289
6. Yeghikyan, A. On dust irradiation in molecular clouds II CR doses // Astrophysics. 2011.54,103
7. Meierhenrich, U. Amino Acids and the Asymmetry of Life, Springer, 2008. 254 pages.
8. Yeghikyan, A., Viti, S., Williams, D. The formation of heavy hydrocarbons in molecular clouds. Mon. Not. R. Astron. Soc. 2001. 326, 313-316
9. Keheyan, Y., Cataldo, F., Yeghikyan, A. Cosmic ray-induced polycondensate hydrocarbons in giant molecular clouds, Astrophysics. 2004. 47, 422-431
10. Ehrenfreund, P., Irvine, W., Becker L.et al., Astrophysical and astrochemical insights into the origin of life, Rep. Prog. Phys., 2002, 65, 1427
11. Yeghikyan, A. On dust irradiation in planetary nebulae in the context of survivability of Ices // Molecular Astrophysics. 2017. 8, 40-47
12. McCarthy, E., Calvin, M. Organic Geochemical Studies . I. Molecular Criteria For Hydrocarbon Genesis, Nature. 1967. 216, 642-647.
13. Sverdlov, L.M., Kovner, M.A., Kraynov, E.P. Vibrational spectra of polyatomic molecules, Nauka, M., in Russian, 1979. 562 pages
14. Yeghikyan, A. Astrobiology, bio-mass-extinctions, and all that // ARAS News, 2013. 64, 8

# AN ESTIMATION OF THE TEMPERATURE-DENSITY RELATION IN THE EARLY UNIVERSE

Telikova K. N.[1], Balashev S. A.[2], Shternin P. S.[2]
[1]Peter the Great St. Petersburg Polytechnic University, St. Petersburg, Russia.
[2]Ioffe Institute, St. Petersburg, Russia
[1]E-mail: ks.telikova@mail.ru

**Abstract:** We present an independent estimate of the power-law index $(\gamma - 1)$ of the temperature-density relation $T \sim \rho^{\gamma-1}$ for the intergalactic medium at intermediate redshifts $z \sim 2 - 3$. The automatic program for analyzing Ly-alpha forest in the quasars spectra using Voigt profile fitting is developed. The analysis results in $(\gamma - 1) = 0.58 \pm 0.08$ at 68 per cent confidence level which is in a broad agreement with results of other authors. The proposed method can be easily extended to study large samples of archival quasar spectral data in an automatic regime.

**Keywords:** absorption lines, quasars, intergalactic medium.

## Introduction

In the Standard Cosmology the primordial matter formed after the Big Bang was the hot optically thick fully ionized plasma. Three hundred thousand years later the temperature decreased enough and formation of atoms has started. Since that epoch the matter in the Universe had remained completely neutral until the first stars and galaxies began to produce ionizing radiation. As a consequence, at redshifts $z < 6$ the intergalactic hydrogen – the major constituent of the Universe – is almost completely ionized. The residual neutral fraction of the intergalactic medium (IGM) is easily detectable, e.g., as the Ly-alpha forest – the series of absorption lines in spectra of background quasars (QSOs). Majority of these lines correspond to Lyman series of neutral hydrogen HI (fig.1).

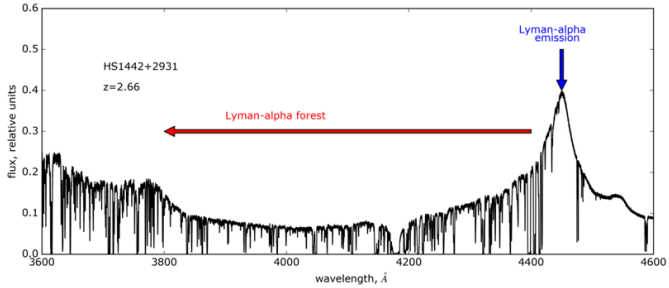


Fig.1. The spectrum of the QSO HS1442+2931 obtained using the HIRES spectrograph on the Keck telescope. The Ly-alpha forest is located in the spectral region bluewards the Ly-alpha emission line and consists of a large number of absorption lines, which correspond to IGM. To estimate the index of the IGM temperature-density power-law dependence we used Voigt profile fitting of these lines.

It is supposed [1] that the temperature and the density of the IGM are related by the power law

$$T = T_0 \left(\frac{\rho}{\bar{\rho}}\right)^{\gamma-1}, \qquad (1)$$

where $T_0$ is the temperature at the mean density $\bar{\rho}$. This form is set by the balance between an adiabatic cooling process due to cosmological expansion and photo-heating processes. It is expected that $\gamma$ depends on $z$, i.e. the equation of state changes in course of the Universe evolution. Therefore, measurements of $\gamma(z)$ give insight into physical processes occurred in the early Universe.

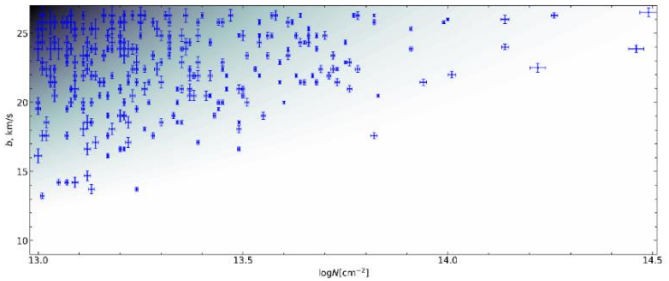


Fig.2. The gradient-filled area shows the best-fit $\boldsymbol{N-b}$ distribution (with darker parts being the denser regions). Error crosses correspond to individual absorption lines found by the automatic search procedure in the selected quasar spectra, see text for details.

One of the few possible ways to infer $\gamma(z)$ is based on an analysis of the Ly-alpha forest, and, in particular, on the estimation of the column density $N$ and the Doppler parameter $b$ for each absorption line using Voigt profile [2–8]. The line parameters $N$ and $b$ depend on the density and the temperature of the absorption system as follows. Parameter $b$ characterizes the width of the velocity distribution of neutral atoms in the system, and has contributions from thermal and turbulent motions. Under microturbulence assumption, these motions are independent and

$$b = \sqrt{\frac{2kT}{m} + b_{turb}^2}\,, \tag{2}$$

where $b_{turb}$ is the width of the turbulent velocity distribution, $k$ is the Boltzmann constant, and $m$ is the mass of the absorber's atom. In case of negligible turbulence, $b_{turb} \to 0$, measured Doppler parameter, $b$, reflects the pure thermal broadening:

$$b \to b_{th} = \sqrt{\frac{2kT}{m}}. \tag{3}$$

In conditions of uniform ionizing radiation, the line column density $N$ is related to the mass density ρ of the absorption system by the power law (e.g., [1–3]). In this case, eqs. (1) and (3) lead to the power-law dependence $b_{th} \sim N^{\Gamma-1}$, where approximately [2–3]

$$\gamma - 1 \approx 3(\Gamma - 1). \tag{4}$$

Therefore, an identification of the lower bound $b_{min}(N)$ of the $N - b$ distribution for a large sample of absorption systems allows to find the parameter $\gamma(z)$ in question. This method with some changes and improvements we use in this work.

**Data**

We selected 10 high resolution (~50000) quasar spectra with high signal-to-noise ratio (~50 – 100). The same sample was used in [2]. We downloaded 9 reduced 1D spectra from KODIAQ database (https://koa.ipac.caltech.edu/Datasets), and one spectrum, HS1442+2931, was reduced by hand.

Redshifts of the Ly-alpha emission peaks in these spectra lie in the range $z$ = 2.5 – 2.9. In each quasar spectrum we scanned for the Ly-alpha forest lines between the Ly-alpha and the Ly-beta emission lines. Therefore the redshift interval of absorption systems studied in

present work is $z$ = 2.02 – 2.87. For each quasar we estimated an unabsorbed continuum level using B-spline interpolation.

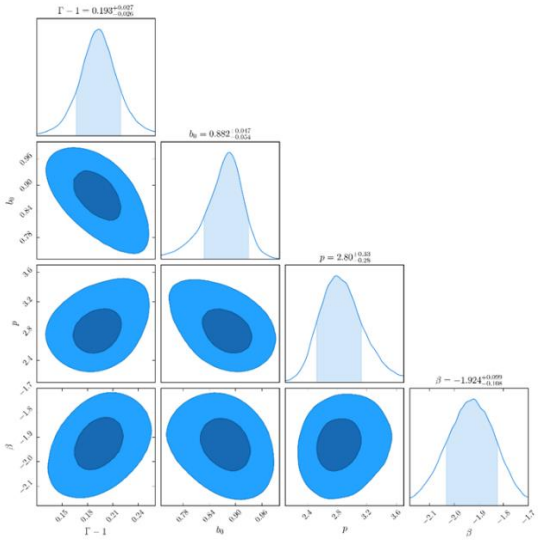

Fig.3. Marginalized posterior distributions of the parameters which specify the assumed b-N distribution. Blue and dark blue colors correspond to 0.683 (1 sigma) and 0.954 (2 sigma) confidence intervals, respectively.

**Analysis and results**

We used an automatic procedure for an analysis of the Ly-alpha forest. Instead of fitting every Ly-alpha forest line, we searched for these lines in the appropriate box in $N - b$ parameter space, near the expected $b_{min}(N)$. Assuming Gaussian statistical errors in the observed optical spectra, we used chi-square likelihood function to fit observed line profiles (consisting of ~30–40 spectral pixels) with modeled Voigt profile. Because the Ly-alpha forest is dense enough in the selected redshift range, some Ly-alpha forest lines blend with each other. To account for such blends we slightly modified likelihood function to remove blended pixels. To increase accuracy, we also added higher order Lyman series absorption lines associated with each Ly-alpha absorption line. The uncertainties on the obtained $N$ and $b$ values for each line were calculated via the Fisher matrix. The

obtained $(N, b)$ sample resulted from the automatic fitting and selection procedure is shown by error crosses in fig.2.

To proceed further, we assumed that the absorption systems are independently distributed over $N$ and $b_{turb}$ and both these distributions have power-law forms with indices $\beta$ and $p$, respectively. For the $N$ parameter this is a standard assumption (see, e.g., [9]). Using this assumption and eqs. (1–2) we performed the maximum likelihood estimate of the distribution parameters $(\beta, p, \Gamma)$ and the normalization constant $b_0 = b_{th}(N = 10^{12} cm^{-2})$. The fitting was done employing the Markov Chain Monte Carlo (MCMC) simulations with the affine sampler *emcee* [10]. The probability density function was normalized in the box in the $N - b$ parameter space, where we searched for the Ly-alpha forest absorption features. The marginal posterior distributions of the fit parameters are shown in fig.3 and the theoretical $N - b$ distribution corresponding to the best-fit parameters is compared with the data sample in fig.2.

The main result of our analysis is the estimate $\gamma - 1 = 0.58 \pm 0.08$ at the 68 per cent confidence. Note that this is an average value corresponding to adopted redshift range of $z$ = 2.02–2.87. In fig.4 we compare this result with available theoretical models and the results of similar analyses by other authors where various methods of the $b_{min}(N)$ estimation were used [2, 5–7].

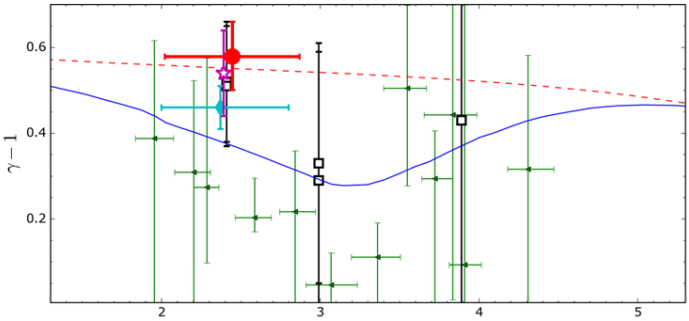


Fig.4. The evolution of $\gamma - 1$ with redshift, $z$. Solid and dashed lines show predictions of theoretical models with and without accounting for the HeII reionization, respectively [11]. Circle shows the result of the present work. Other measurements obtained by Voigt profile fitting of Ly-alpha forest are shown by triangles [4], squares [6], diamonds [2], and stars [5].

**Summary**

We developed the automatic procedure for fitting absorption lines over the Ly-alpha forest range in the spectra of QSOs using Voigt function. This procedure was applied to 10 spectra with high quality and resolution. We found that the power-law index of the IGM equation of state at $z$ = 2.02–2.87 is $(\gamma - 1) = 0.58 \pm 0.08$ (68% confidence). Our result agrees (see fig.4) with the measurements done for the same spectra [2] and with other estimates made using the Ly-alpha forest line analysis via the Voigt function profile fitting [6]. An important advantage of our method is in a possibility to analyze large data samples in an automatic fashion. Therefore it can be applied to the quasar spectra in Keck and VLT archives without serious complications. This will allow us in a future to put robust constraints on the redshift dependence of the parameter $\gamma(z)$ and hence on the evolution of the IGM in the early Universe.

**References**

1. Hui, L., Gnedin, N. Y., 1997, MNRAS, 292, 27
2. Rudie, G. C., Steidel, C. C., Pettini, M., 2012, ApJ, 757, L30
3. Schaye, J., Theuns, T., Leonard, A., Efstathiou, G., 1999, MNRAS, 310, 57
4. Schaye, J., Theuns, T., Rauch, M., Efstathiou, G., et al., 2000, MNRAS, 318, 817
5. Bolton, J. S., Becker, G. D., Haehnelt, M. G., Viel M., 2014, MNRAS
6. McDonald, P., Miralda-Escude, J., Rauch, M., Sargent, et al., 2001, ApJ, 562, 52
7. Bryan, G. L., Machacek, M. E., 2000, ApJ, 534, 57
8. Ricotti, M., Gnedin, N. Y., Shull, J. M., 2000, ApJ, 534, 41
9. Janknecht, E., Reimers, D., Lopez, S., Tytler, D., 2006, Astron. Astrophys. 458, 427
10. Foreman-Mackey, D., Hogg, D. W., Lang, D., Goodman, J., 2013, PASP, 125, 925
11. Upton Sanderbeck, P. R., D'Aloisio, A., McQuinn, M. J., 2016, MNRAS, 460, 1885

# HYBRID MODELING OF QUASIPARALLEL COLLISIONLESS SHOCKS IN TWO-SPECIES PLASMAS: TRAJECTORIES OF SUPRATHERMAL PARTICLES

Kropotina J.[1, 2], Bykov A.[1, 2], Krassilchtchikov A.[2], Levenfish K.[2]
[1]Peter the Great St. Petersburg Polytechnic University, St. Petersburg, Russia
[2]Ioffe Institute, Saint-Petersburg, Russia
[1] E-mail:juliett.k@gmail.com

**Abstract:** An individual-particle kinetic analysis of ion injection into the process of diffusive shock acceleration (DSA) is performed within a hybrid simulation of interstellar plasma for the case of two-species medium. It appears that only those ions, which are reflected from the shock front during their first interaction with it, are further injected into the efficient DSA.

**Keywords**: collisionless shocks in space plasmas, cosmic rays, hybrid simulation of plasmas.

## Introduction

Collisionless processes often dominate the dynamics of astrophysical plasmas due to the relatively low densities of the interstellar medium, allowing Coulomb mean free paths of the ions to be much larger than the system size. Physical processes in such systems are governed by collective nonlinear interactions between charged particles and fluctuating electromagnetic fields. In particular, various plasma instabilities, magnetic field amplification, and non-Maxwellian distributions of particles are likely to develop, making the problem too complicated to be solved analytically. Therefore, advanced numerical techniques are required to model the mentioned systems and processes. One of the commonly used methods is the hybrid approach, where ions are treated as individual particles, while electrons are represented by massless fluid [1]. This approach allows one to maintain a reasonably good balance between precise modeling of nonlinear processes on ion scales and saving numerical resources due to neglection of individual electrons.

One of the long-standing and important problems of modern astrophysics is the origin of cosmic rays — accelerated particles of energies up to $10^{21}$ eV, registered both directly with space-borne spectrometers and indirectly via ground-based observations of extensive air showers. Galactic cosmic rays of energies up to $10^{15}$ eV are believed to originate from supernova remnants, where they are accelerated by collisionless shocks driven by super-Alfvenic particle flows. Quasi-parallel collisionless shocks, where the angle between the shock normal and the direction of the ambient magnetic field is substantially less than $\pi/4$, are considered efficient particle accelerators. In the vicinities of such shocks energetic particles undergo diffusive shock acceleration (DSA), which allows them to gain energy due to multiple shock crossings [2]. However, to get involved, the ions need to be sufficiently pre-accelerated to overcome the cross-shock potential. Particular details of such pre-acceleration are still not clear (the so-called "injection problem"). A recent work [3] associated the pre-accelerated particles with reflected ion beams, observed *in situ* in the Solar wind. The authors of [3] also presented hybrid modeling of particle reflection at a shock and showed how the system proceeds beyond the initial injection steps. In the present work we add to the results of [3], emphasizing that all the particles, which eventually gain energy substantial to be injected into the DSA, are initially reflected at the shock front. We also expand our investigation to the case of two-species (hydrogen and helium) plasmas and find that particles of both sorts get accelerated in a similar way.

**Hybrid modeling of shock dynamics and ion injection**

A plasma box containing a moving collisionless shock was modeled with the three-dimensional second-order accurate hybrid code with exact magnetic field divergence conservation, described in [4, 5]. All the physical parameters of the system were normalized to the upstream proton inertial length ($l_i$), ion gyrofrequency ($\Omega_i$), Alfven velocity ($V_A$) and plasma density. The shock was initiated via a standard piston method, when the initial flow of super-Alfvenic ions moving in the negative $x$ direction is reflected from a conducting wall at $x = 0$. The modeling considered an initially uniform magnetic field directed in the $x$-$z$ plane and inclined by $10^o$ to the flow direction. Shock parameters typical for a supernova remnant were chosen: the

Afvenic Mach number of the initial flow $M_A$=10 (in the downstream reference frame), the upstream ratio of thermal to magnetic pressure $\beta$ = 0.001. The medium consisted of 75% protons (by mass) and 25% He (+1) ions (by mass). The simulation was performed in a rectangular box of length 10000 x $l_i$ on the time scale t = 850 $\Omega_i^{-1}$.

Soon after the shock was initialized, the energy spectra of the ions showed characteristic power-law tails, indicating particle injection into the DSA. By the end of the simulation timescale the protons reached energies up to about 700 $E_{sh}^{p}$, and the He ions — up to 150 $E_{sh}^{He}$ where $E_{sh}$ is their far upstream kinetic energy (note that the maximal velocities of the protons appeared twice those of the He ions). For each sort we selected some dozens of most energetic particles and traced their coordinates and velocities, as well as electromagnetic fields, acting on them, back until the simulation start. We considered only those particles, which interacted with the shock front after its complete formation at about 250 $\Omega_i^{-1}$ in order to exclude possible unphysical influence of the boundary conditions. The resulting particle trajectories in physical space were confronted with time-dependent maps of magnetic field amplitudes and effective angles, thus highlighting the behavior of the injected particles. Those trajectories and maps were further confronted with x-$V_x$, x-$V_y$, x-$V_z$, and x-E phase spaces with pin-pointed positions of injected particles for successive evolution times.

Thereby, it became evident that all the particles, which eventually gain substantial energy, were reflected back during their first interaction with the shock front. This observation is consistent with the results of [3] and contradicts the so-called “thermal leakage injection” hypothesis, where thermal, but energetic (“the Maxwellian tail”) particles from the shock downstream penetrate upstream and are injected into the acceleration mechanism. The latter process seems to be in fact suppressed by strong magnetic field fluctuations in the vicinity of the shock front, which could be overcome only by the already supra-thermal ions.

Typical trajectories of injected particles of both sorts are illustrated on the top panel of Fig. 1 along with the evolution of the shock front itself. The middle panel shows the local magnetic field angle to the shock normal at the selected position, while the bottom panel illustrates the evolution of the ion energies.

It should be noted that injected particles of both sorts behave similarly: during the first interaction with the shock front they interact with the quasi-perpendicular component of the magnetic field and thus do not penetrate downstream, instead continuing to move along the shock front (this process is sometimes called the shock drift acceleration [SDA] and is characteristic for quasi-perpendicular field configuration [see the middle panel of Fig. 1]). During this first stage some preliminary energy gain occurs. Eventually, such a drifting particle reaches a quasi-parallel field zone and moves back upstream, thus completing the primary reflection stage to further enter the DSA. One may also note that for the He ions this first stage is longer, due to their larger gyroradii. For the same reason during the SDA stage the He ions penetrate slightly deeper into the shocked medium. However, the whole mechanism is similar for H and He ions, in contrast with [6], who proposed that heavier ions reflect not from the shock front, but from post-shock magnetic irregularities. That can be true for the ions, which have already gained sufficient energy, but, as it can be seen from the *proton2* trajectory in Fig. 1, it is not a unique property of all the heavy ions, but occurs only at a certain phase of the DSA.

As an ion is injected into the DSA process, its acceleration consists of multiple shock crossings and reflections both upstream and downstream. Comparing the top and the bottom panels of Fig. 1, one may conclude that most efficient energy gain is usually obtained during the shock reflection events.

**Conclusions**

An individual-particle modeling of ion injection into the process of diffusive acceleration (DSA) at an interstellar shock has been performed within a hybrid simulation for the case of two-species plasma. It was found that injected ions of both sorts enter the DSA process in similar ways, but for heavier ions each step is longer and acceleration is slower (by a factor of 2 in case of He[+1]) due to larger spatial and temporal scales. An important observation was made, that for 100% of sufficiently energized particles their acceleration started with a reflection from the shock front. However, this process consists of two consequent phases: a shock drift stage in an area of quasi-perpendicular magnetic field, and an upstream escape after the particle reaches a quasi-parallel field area. Subsequently, the accelerated

particles gain energy via multiple reflections off upstream precursor waves and downstream magnetic irregularities.

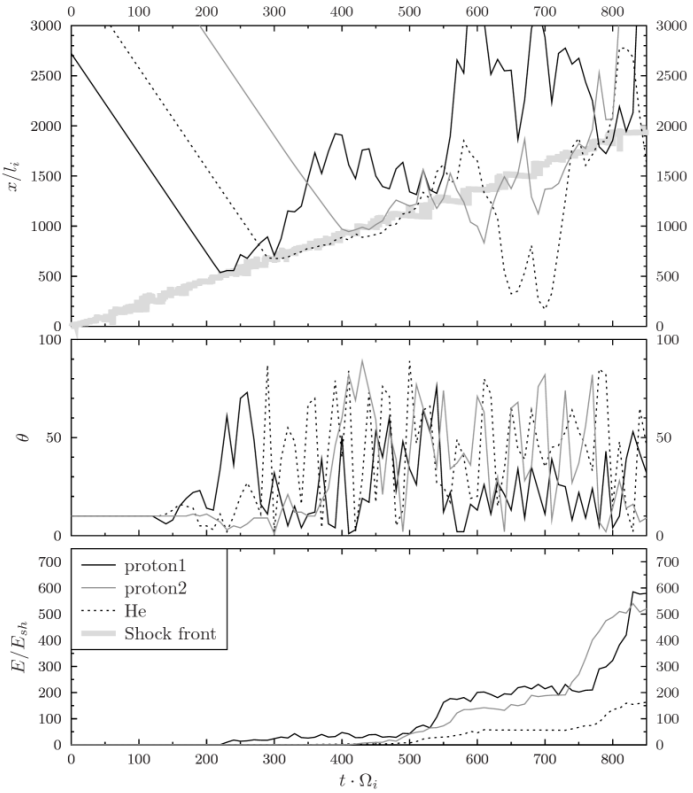


Fig. 1. Temporal evolution of injected particle trajectories (top panel), local magnetic field angles (middle panel) and particle energies (bottom panel). Two protons, denoted as *proton1* and *proton2*, and one He ion were chosen here to illustrate typical behavior of injected ions.

## References

1. Matthews, A.P. Current Advance Method and Cyclic Leapfrog for 2D Multispecies Hybrid Plasma Simulations // J. Comp. Phys. 1994. n. 112, pp. 102–116.

2. Caprioli, D.; Spitkovsky, A. Simulations of Ion Acceleration at Non-relativistic Shocks. I. Acceleration Efficiency // ApJ 2014. vol. 783, i. 2, pp. 783:91.
3. Sundberg, T.; Haynes, C.T.; Burgess, D.; Mazelle, C.X. Ion Acceleration at the Quasi-parallel Bow Shock: Decoding the Signature of Injection // ApJ 2015. vol. 820, i. 1, id. 21, 15 pp.
4. Kropotina, Yu.A.; Bykov, A.M.; Gustov, M.Yu.; Krassilchtchikov, A.M.; Levenfish, K.P. Relaxation of heavy ions in collisionless shock waves in cosmic plasma // Technical Physics 2015. vol. 60, i. 2, pp. 231-239.
5. Kropotina, Yu.A.; Bykov, A.M.; Krasil'shchikov, A.M.; Levenfish, K.P. Hybrid simulation of collisionless shock waves in space plasma // Technical Physics 2016. vol. 61, i. 4, pp. 517-524.
6. Caprioli, D; Yi, D.T.; Spitkovsky, A. Chemical Enhancements in Shock-accelerated Particles: Ab-initio Simulations // eprint arXiv:1704.08252.

## MODELING OF X-RAY STRIPES IN TYCHO'S SUPERNOVA REMNANT

Kalyashova M.E.[1,2], Bykov A.M.[1,2], Osipov S.M.[1,2]
[1]Peter the Great St. Petersburg Polytechnic University, St. Petersburg, Russia
[2]Ioffe Institute for Physics and Technology, St. Petersburg, Russia
E-mail: filter-happiness@yandex.ru

**Abstract**: Chandra observations of Tycho's supernova remnant (SNR 1572) allowed us to get high-resolution X-ray images of SNR. It was discovered that there are several series of coherent X-ray structures (bright, almost parallel stripes) in some regions of SNR. It is likely that the observed radiation of Tycho's SNR is synchrotron radiation of electrons with energies about $10^{14}$ eV. We develop a model, which represents synchrotron X-ray images of Tycho's SNR in order to reveal the physical mechanism of the observed structures formation. The model allows one to connect the bright stripes with a specific mechanism of the energetic particle transport in SNR. In particular, it is shown that the mirror instability, which evolves in plasma near SNR shock as a result of anisotropic

distribution function of electrons, can be the reason of the observed stripes.

**Keywords**: supernova remnants, mirror instability, synchrotron radiation, superdiffusion

## Introduction

Supernova remnants are very interesting and important objects for high energy astrophysics. Inside the remnant non-trivial configurations of magnetic field, density and pressure can occur. Observations and modeling of SNRs are necessary to shed light on physical properties and chemical composition of SNR.

Firstly the results of Chandra observations with series of X-ray stripes were published by Eriksen et al. in 2011[1]. In that paper there was also a first attempt to give explanation to the existence of such an ordered structure. In the same year, Bykov et.al. [2] performed modeling of synchrotron radiation of electrons in a magnetic field, amplified by Bell instability, which was supposed to be the main reason of the stripes. However, understanding the true origin of Tycho's stripes remains a challenge for high energy astrophysics.

The aim of this work is not only to make a model to fit the observations, but also to reveal physical processes which are standing behind the observed structures. It is likely that the stripes occur as a result of synchrotron radiation of electrons in modulated magnetic field. The scientific novelty of our research is in taking into account mirror instability. We assume that mirror instability can be the reason of modulation and amplification of the magnetic field in the remnant. Mirror instability arises when there is quadrupole anisotropy of a particle distribution function, which, in turn, exists, when particle transport is superdiffusive. Unlike Bell instability, mirror instability affects both magnetic field and distribution function of electrons, and, which is the most important, mirror instability is long-wavelength.

## Electron distribution function and mirror instability

We can model electron distribution function near the front of a collisionless shock wave using Monte Carlo (MC) simulations (the method is described by Bykov et.al. in [3]). As it was already said above, mirror instability occurs only with non-zero quadrupole

anisotropy of a distribution function. Because of that we use a superdiffusive (i.e. $\langle \Delta x^2 \rangle \sim \Delta t^{\delta};\ \delta > 1$) model of particle propagation in simulations. Although in [3] the shock wave front is plane, the results of this method can be used in our work, because at small distances from the front we can neglect its sphericity.

The electron distribution function with the second anisotropy has the form:

$$f_0(p,\mu) = \frac{n_{cr}N(p)}{4\pi}\left[1 + \frac{\chi}{2}(3\mu^2 - 1)\right] \quad (2.1)$$

Here, $\chi$ is the parameter of anisotropy, $\mu = \cos\theta$, where $\theta$ is an angle between velocity and background magnetic field $\mathbf{B}_0$. The dispersion relation for mirror instability can be derived from linearized fluid mechanics equations (for background plasma) and kinetic equation (for energetic electrons), where anisotropic electron distribution function (2.1) should be used. All the parameters of plasma are defined as $\xi = \xi_0 + \delta\xi, \delta\xi \propto e^{i\mathbf{kr} - i\omega t}$. The dispersion relation has the form [3]:

$$\omega_{mir}^2 = \left(v_a^2 + a_0^2 + 2\frac{\delta P}{\rho_0}\right)k^2 \quad (2.2)$$

Here, $v_a$ is the Alfven velocity, $a_0 = \sqrt{\frac{\gamma_g p_0}{\rho_0}}$, $\delta P = P_{\parallel} - P_{\perp} = \frac{3\chi}{5}P_0$, $P_0 = \frac{n_{cr}}{3}\int_0^{\infty} vp^3 N(p)dp$. Equation (2.2) shows that magnetic field modes (we are mostly interested in a mode, parallel to the background field $\delta B_z \propto e^{i\mathbf{kr} - i\omega t}$) are growing, when $\delta P \propto \chi < 0$. Thus, the physical explanation of mirror instability is anisotropic pressure of electrons. The complete derivation of the formula (2.2) can be found in [3].

We also should take into account the modulation of the distribution function by mirror instability. It transforms into $f = f_0 + \delta f$, where

$$\delta f \approx \frac{\delta B_z}{B_0}\frac{n_{cr}N(p)}{4\pi}\frac{3\chi}{2}\sin^2\theta \quad (2.3)$$

Hence, distribution function oscillates due to the oscillations of *z*-component of the magnetic field.

**Modeling of the magnetic field**

As it follows from the MC simulation [3], the best amplified mode (as a result of mirror instability) is the mode with $k_0 r_{g0} = 2 \cdot 10^{-7}$, where $r_{g0} = \frac{mcu_{sh}}{eB_0}$, $u_{sh} = 5 \cdot 10^8 cm/s$ is a shock velocity, $B_0 = 3\,\mu G$ is the background (interstellar) magnetic field. Its growth rate gives $\frac{\delta B_z}{B_0} \approx 3$. We put in the code the magnetic field in the remnant as:

$$B^2 = B_0^2 + B_{rand}^2 + B_{mode}^2 \quad (3.1)$$

The total magnetic field in the remnant is the sum of background field, mode, amplified by mirror instability and random magnetic field, which necessarily occurs near the shock wave. The random part of the magnetic field in our code is just a sum of plane waves with random phases, wavevectors and polarizations. The rate of a total magnetic field is defined by MC simulations.

**Synchrotron radiation modeling**

To get the intensity of synchrotron radiation of electrons we use a formula from [4]:

$$J(\nu, k) = \frac{\sqrt{3}e^3}{mc^2} \int \left\{ N(E, \mathbf{r}, \mathbf{k}) B \sin\theta \frac{\nu}{\nu_c} \int_{\frac{\nu}{\nu_c}}^{\infty} K_{\frac{5}{3}}(\eta) d\eta \right\} dE dr \quad (4.1)$$

where

$$\nu_c = \frac{2eB_\perp}{4\pi mc} \left( \frac{E}{mc^2} \right)^2 \quad (4.2)$$

We have no need to perform a modeling of the whole remnant, so we compute the intensity of synchrotron radiation only for a small part of a remnant, where the stripes were discovered. To imitate the observed picture we integrate the intensity along the line of sight.

**Results**

The result of modeling is shown in fig.1.

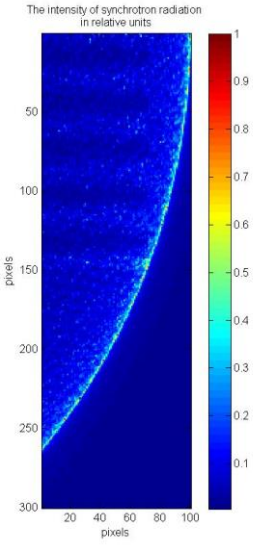


Fig. 1 The image of synchrotron radiation of Tycho's SNR with stripes. 1 pixel corresponds to 0.01 pc.

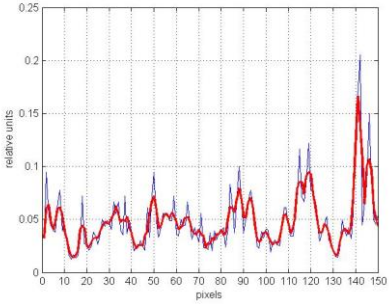


Fig. 2 The intensity of stripes in relative units.

One can see a series of parallel stripes appearing. The distance between stripes in our calculations is $\lambda = \frac{2\pi}{k_0} \approx 5.2 \cdot 10^{17} cm$, while the observed distance is $8'' \approx 4.56 \cdot 10^{17} cm$ [1]. So, we can say that the distances received by modeling correspond well with the observations.

The other parameter of stripes is their brightness. Fig. 2 shows that the ratio between intensities of stripe and non-stripe regions is from 2 to 8. From Chandra [5] image it is visible that for brightest stripes that ratio can reach 10, but the average value also corresponds with our model.

**Conclusions**

The model results presented in Fig.1 are in a reasonably good correspondence with the observations by Chandra. It gives a satisfactory explanation for appearing a highly-ordered structure in the

radiation of Tycho's supernova remnant. Moreover, if the stripes are indeed produced by the mirror instability then the superdiffusive particle transport should be considered as a plausible mechanism in the supernova remnants.

## References


1. Eriksen, K. et.al. Evidence for particle acceleration to the knee of the cosmic ray spectrum in Tycho's supernova remnant. ApJ Letters, 2011
2. Bykov, A.M. et.al. X-ray stripes in Tycho's supernova remnant: synchrotron footprints of a nonlinear cosmic-ray driven instability. ApJ Letters, 2011
3. Bykov, A.M., Ellison, D.C., Osipov, S.M. A nonlinear Monte Carlo model of super-diffusive shock acceleration with magnetic field amplification. Phys.Rev. E 95, 033207, 2017
4. Ginzburg, V. L.; Syrovatskii, S. I. Cosmic Magnetobremsstrahlung (synchrotron Radiation) Annual Review of Astronomy and Astrophysics, vol. 3, p.297, 1965
5. Evans, I. N., et al. 2010, Ap JS, 189, 37


# ANALYTICAL TIME-DEPENDENT INSTANTANEOUS FREQUENCY THEORY OF CHARGED PARTICLE MOTION IN ELECTROMAGNETIC FIELDS IN SPACE


Tsybin O.Yu.

Peter the Great St. Petersburg Polytechnic University, St. Petersburg, Russia

E-mail: otsybin@rphf.spbstu.ru



**Abstract:** A theoretical analysis has been carried out by means of novel differential equation for charged particles motion in electromagnetic fields in space plasma.



**Keywords:** Space, plasma, charged particle, electromagnetic field.


## Introduction

The Solar System and the Universe in whole are filled with space plasma. Plasmas occupy the magnetospheres of the Earth and

other planets, the solar corona and solar wind, tails of comets, the inter-stellar and inter-galactic media. Mainly, such plasmas contain both electron and ion components. A theoretical analysis of charged particles motion in electromagnetic fields remains high-demand in space plasma and ion physics, as well as in many other scientific fields like vacuum electronics, mass spectrometry, and so on. Computer simulation is a powerful tool for space plasma investigation, although analytical approach reveals more detailed understanding of actual physical processes in charged particles ensembles in free space. A possible approach is considered comprehensively for further development of analytical method produced via both the time-dependent non-linear phase (NP) and instantaneous frequency (IF) concepts describing the charged particle motion. Previously, Hilbert transform (HT) and Gabor's complex analytical signal (AS) approach were applied to Newtonian single particle motion equations in a framework of the frequency partition. [1]

Recently, using the HT and AS platform, differential equations (DE) were derived which describe time-dependent NP and IF of charged particles motion in a specific complex space without preliminary partitioning of frequency [2]. Firstly, the instantaneous frequency concept developed methods and technique of vacuum electron or ion devices, e.g., mass spectrometers. Now, several novel solutions appeared as appropriate tools for the space objects analysis.

**Basic theory**

For plasma in free space, one needs to contribute nonlinear and space charge fields, specific boundary conditions, relativistic effects, complex spectral compositions of ions, and so on. Here, we start with much simpler task. Its main and novel feature is time-dependent instantaneous non-linear phase and frequency. Since radial and azimuthal components of a moving particle time-dependent complex radius-vector in the plane transversal to uniform magnetic field $\tilde{r}(t) = r(t) \cdot \exp[-i(\varphi - \varphi_0)]$ are coupled by HT, then $\tilde{r}(t)$ is an AS by definition, and thus its properties allow determination IF in each point of the particle trajectory in a limited volume. Within our approach, the $\tilde{r}(t) = r_0 \exp[-i\Phi(t)]$ is associated with the constant

amplitude wave with an unwrapped NP $\Phi(t)$ that complies with the relation $\Phi(t) = (\varphi - \varphi_0) + i \cdot \ln \frac{r(t)}{r_0}$.

The spectral function $S(\tilde{\omega})$ of a complex potential field in free space $\tilde{U}(t) = \frac{1}{4\pi\varepsilon_0\varepsilon} \cdot \frac{q}{\tilde{r}(t)}$ generated by a moving charge *q* could be revealed by Fourier Transform (FT) of $\tilde{U}(t)$:

$$S(\tilde{\omega}) = \frac{r_0 q}{4\pi\varepsilon_0\varepsilon} \int_0^\infty dt \cdot e^{i\Phi - i\omega t}.$$

The largest $S(\tilde{\omega})$ value is achieved with constant phase $[\Phi(t) - \omega t]$. Therefore, the set of frequency values $(cod\omega)$ is defined by $(cod\omega) = \tilde{\omega}(t) = \frac{d\Phi(t)}{dt}$. In the case of a linear time-dependent phase, one obtains $\frac{d\Phi(t)}{dt} = \frac{d(\omega t)}{dt} = \omega = const$. For NP, the IF $\tilde{\omega}(t)$ is a *codomain* generalization of a traditional notion of static frequency of stationary periodic signals. Contrary to Fourier frequency, the IF value reflects local NP deviations. Therefore, signals in the detection circuitry could be locally represented by static frequency and a time-dependent dispersion around this frequency. In case of charged particles motion, complex IF $\tilde{\omega}(t) = \dot{\varphi}(t) + i\frac{\dot{r}(t)}{r(t)}$ contains both angular and radial frequencies. In other words, IF is determined by radius amplitude (length) dynamics, and both radial and azimuthal charged particle velocities:

$$\tilde{\omega}(t) = |\tilde{\omega}| \cdot \exp \cdot i(\arg\tilde{\omega} + 2\pi k), \quad k = 0, \pm 1, \pm 2, ..., |\tilde{\omega}| = \sqrt{\dot{\varphi}^2 + \left(\frac{\dot{r}}{r}\right)^2},$$

$$\arg\tilde{\omega} = \arctan\frac{\dot{r}}{r\dot{\varphi}}.$$

Using the formalism described above, one can transform Newtonian

motion equations into the first order DE that present IF spectra of the electrical field, generated by volume currents $q\dot{\tilde{r}}$ [2]:

$$i\dot{\tilde{\omega}} + \tilde{\omega}^2 - \tilde{\omega}\omega_c + \frac{q\tilde{E}(t)}{m\tilde{r}} = 0. \qquad (1)$$

In Eqn. (1) *m* denotes a particle mass value, $\omega_c$ is cyclotron frequency, $\tilde{E}(t)$ is electric field value on the trajectory. The Eqn. (1) can be represented in the following exponential form:

$$\tilde{\omega}(t) = \omega_0 \cdot \exp\left[ i\Phi - i\omega_c t + \int_0^t \frac{\eta\tilde{E}(t)}{\dot{\tilde{r}}}\,dt \right], \quad \omega_0 = -\dot{\varphi}_0 + i\frac{\dot{r}_0}{r_0},$$

$$\tilde{\omega}\cdot\tilde{r} = r_0\omega_0 \cdot \exp\left[ -i\omega_c t + i\int_0^t \frac{\eta\tilde{E}(t)}{\tilde{\omega}\cdot\tilde{r}}\,dt \right]. \qquad (2)$$

In another form, solution of Eqn. (1) for any arbitrary electric fields can be found via Laplace transform following the standard approach of its application to DE solution [2]:

$$\tilde{\omega} - \tilde{\omega}_0 e^{-i\omega_c t} - i\cdot\left[ \tilde{\omega}^2 + \frac{\eta\tilde{E}(t)\cdot u_0(t)}{\tilde{r}(t)} \right] * e^{-i\omega_c t} = 0,$$

$$\tilde{r}(t) = \tilde{r}(0) + \frac{\dot{\tilde{r}}(0)}{i\omega_c}\left(1 - e^{-i\omega_c t}\right) + \frac{\eta}{i\omega_c}[\tilde{E}(t)\cdot u_0(t)] * \left(1 - e^{-i\omega_c t}\right), \qquad (3)$$

$$\dot{\tilde{r}}(t) = \dot{\tilde{r}}(0)\cdot e^{-i\omega_c t} + \eta[\tilde{E}(t)\cdot u_0(t)] * e^{-i\omega_c t}.$$

In Eqn. (3) the asterisk means convolution integral procedure, $\tilde{r}(0), \dot{\tilde{r}}(0)$ are initial complex radius-vector and velocity respectively, and $u_0(t)$ is the boxcar function of electric field, in the form of Heaviside unit step function, e.g., $u_0(t) = 0, t < 0, u_0(t) = 1, t \geq 0$. In the case of a zero magnetic field, one can put $\omega_c = 0$ in Eqns. (1–3).

**Phase resonance and space charge field**

Equations and solutions (1–3) contain any electric field $\tilde{E}(t)$, so the opportunity of nonlinearities and space charge fields is given.

The trajectory parameters and the motion dynamics scenario depend on an electric field $\tilde{E}(t)$ by combined Eqns. (1–3). In free space we can consider plasma potential in the form of cylindrical harmonics, so we receive azimuthally periodical solutions of charged particles motion. Further, among the analytical solutions of Eqns. (1–3), we have obtained two particular ones for the following cases: a linear field $\tilde{E} = const \cdot \tilde{r}$, and effective acceleration/deceleration field $\tilde{E} \times \tilde{r} = 0$. Then, using the approach mentioned above (which has led to Eqn. (1)), we received the DE of the same structure for NP and IF of charged particle oscillations in (r, z) plane. Therefore, NP and IF of the charged particle motion in electromagnetic field have been described as two coupled 2D non-linear oscillators, $(r, \varphi)$ and $(r, z)$.

**Conclusion**

The time-dependent non-linear phase and instantaneous frequency concepts could be applied for investigation of charged particle motion in space plasma. In order to improve such applications one needs further expansion of the developed theory for multicomponent instantaneous frequency approach, dissipative losses, non-uniform magnetic field, relativistic case, and so on.

**References**


1. Vainshtein L. A., Vakman D. E. Frequency partition in oscillations and waves theory, Moscow, “Science” Publishing Company, 1983 (in Russian).
2. Tsybin O. Yu., Tsybin Y. O. Time-dependent frequency of ion motion in Fourier transform mass spectrometry // International Journal of Mass Spectrometry, Volume 376, 15 January 2015, Pages 75-84.

# Section Tools of Modern (Radio) Astronomy

## A SYNCHRONIZATION OF SESSIONS OF VLBI-OBSERVATIONS BY MEANS OF THE GLOBAL NAVIGATION SATELLITE SYSTEMS

Amelchenko A.O.[1], Karpichev A.S.[2]
[1]Peter the Great St. Petersburg Polytechnic University, St. Petersburg, Russia
[2]Institute of Applied Astronomy of the Russian Academy of Science, St. Petersburg, Russia
E-mail: 2313294@mail.ru

**Abstract:** The article explores the method of preliminary synchronization of VLBI observations with the help of GNSS receiver NVS-GNSS-STA/CH-5831. It also investigates the dependence of the clock difference on the operating mode of the receiver. The results obtained are compared for each of the operating modes. Based on the comparison, the optimum operating mode ensuring a difference in the stroke of the clock not more than 50 ns has been detected.

**Keywords:** VLBI-observations, GNSS receiver, standard time and frequency.

Improving the accuracy of pre-synchronization of VLBI observations and monitoring the timing of data logging using GNSS receivers operating only with L1 signals is possible. The operation modes of the NVS-GNSS-STA/CH-5831 receiver have been studied for its application in this regard. It has three modes of operation: free mode, averaging mode and "time on hard point" mode. The synchronization error does not exceed 15 ns (one sigma) [1–4].

Temporal stability of a time stamp of the receiver and its dependence on a receiver operation mode has been received and probed. The diagram of the experimental installation is shown in fig. 1.

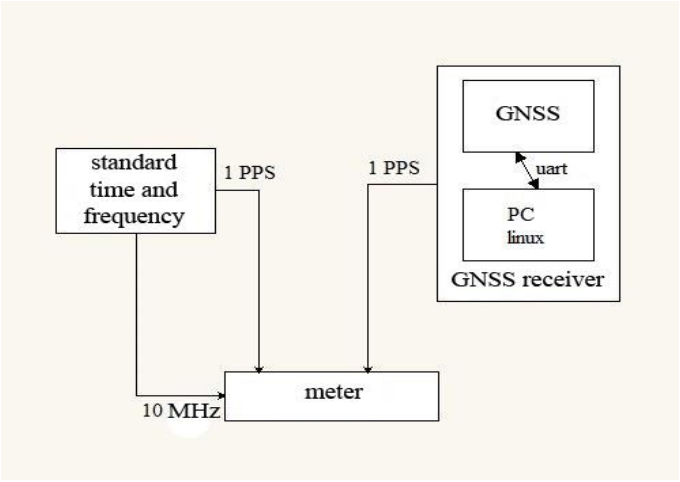


Fig. 1. A block diagram of experimental installation.

The time stamp of the GNSS receiver has a big error and a time delay concerning a time stamp of the standard of frequency and time (fig. 2).

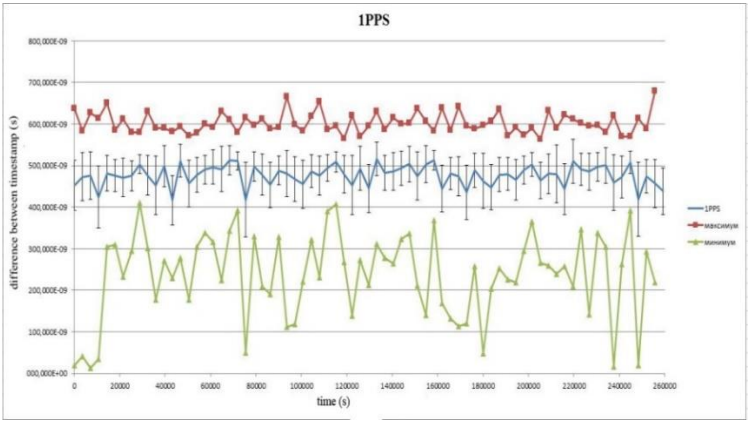


Fig. 2. An average clock difference in free mode.

The graph shows that the magnitude of the difference in the clock for free mode is on average 90 ns.

In the averaging mode of the interval, the errors of the σ label for the averaging time of 20 minutes (Fig. 3) and 1140 minutes (Fig. 4) were calculated in the interval.

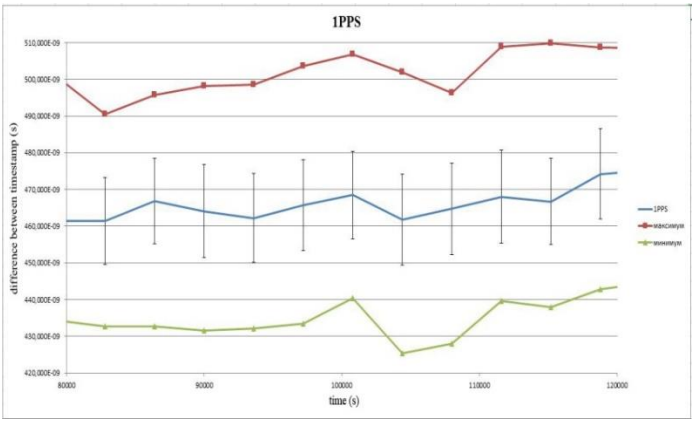


Fig. 3. Averaging the clock difference in the averaging mode in 20 minutes.

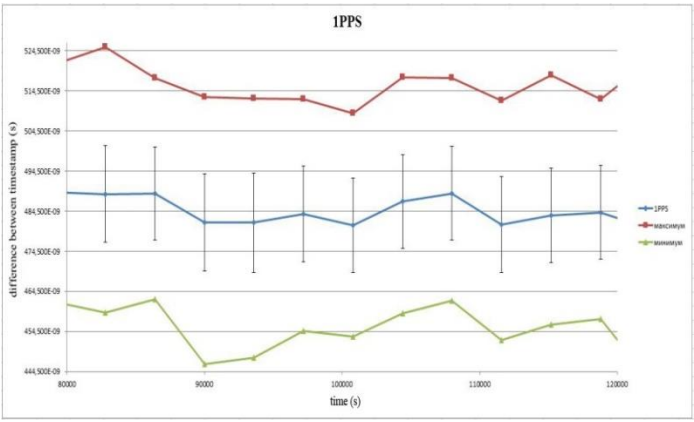


Fig. 4. Averaging the clock difference in the averaging mode in 1140 minutes.

The value of the clock difference for the averaging mode is on average 15 ns. By operation of the receiver in the mode of averaging

of coordinates in 20 minutes and in 1140 minutes the differences of the course of hours identical to each other experimentally were received.

Application of the method of post-processing of the receiver using data information about the correction to the front of the output mark signal relative to the solution of the navigation problem makes it possible to reduce the instability of the receiver time mark to 5–10 ns (Fig. 5).

In contradiction to the free mode, the averaging mode of the coordinates provides an increased accuracy of the timestamp.

The instability and latency of the time stamp of the GNSS receiver relative to the timestamp of the standard frequency and time in the averaging mode of coordinates do not depend on the averaging time of the coordinates. Averaging the coordinates in 20 minutes is enough to obtain accuracy within 50 ns.

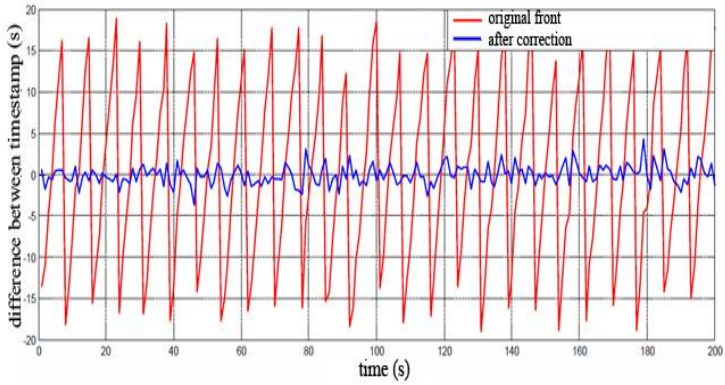


Fig. 5. Shift of 1PPS relative to UTC before and after software correction.

The use of post-processing makes it possible to reduce the instability of the time stamp of the receiver to 5–10 ns, which will improve the accuracy of synchronization of VLBI observations.

GNSS receiver can be used for preliminary synchronization of observational data and control of data acquisition timing.

**References**

1. GPS timing algorithm // SITCOM. – URL: http://www.sitcom.ru/www/content/view/63/10. – (accessed: 15.02.2016).
2. Products »Antennas » CH-5831// NVS. – URL: http://www.nvsgnss.com/products/ antennas/item/38-timing-smart-antenna-glonass-gps.html. – (accessed: 12.11.2015).
3. Products » Receivers » NVS-GNSS-STA// NVS. – URL: http://www.nvsgnss.com/products/ receivers/item/42-timing-smart-antenna-glonass-gps.html – (accessed 12.11.2015).
4. UTC to GPS Time Correction// QPS. – URL: https://confluence.qps.nl/display/KBru/ UTC+to+GPS+Time+Correction. – (accessed 15.02.2016).

## A RESEARCH OF DIFFERENT DEFORMATIONS INFLUENCE ON ROT-54/2.6 RADIO TELESCOPE ANTENNA

Khachatryan A.[1], Sargsyan A.[2]
[1]National Polytechnic University of Armenia, Teryan str., Armenia,
[2]Russian-Armenian University, National Polytechnic University of Armenia, , Yerevan, Armenia,
[1]Email: khachatryanartavazd@gmail.com
[2]Email: antenna@seua.am

**Abstract:** A telescope is never perfect because of mechanical, gravity, temperature and wind induced deformations of its structure, because of production imperfections and because of accidental small misalignments of the constrictive elements. The resulting degrading effect on the beam pattern is negligible if the corresponding deformation of the reflector and the misalignment of the constructive elements (main reflector, sub reflector, receiver) are small compared to the wavelength of observation, i.e. smaller than λ/16. The degradation becomes noticeable and disturbing if the corresponding deformation is larger than λ/10 [1].

In our work we examined the different deformations influence on field distribution in antenna's aperture for ROT-54/2.6 Radio Optical Telescope. Even taking into considerations that the gravity and wind impacts are minimized

in ROT-54/2.6 because of constructive feature, we obtained simple formulas demonstrating each type of deformation influence on phase distortion as well as combined impact of deformations on overall antenna efficiency.

## Introduction

Antennas used for radio telescopes usually have large dimensions and generally are composed by set of surface panels with supporting structure (also known as a backup structure) [2]. So far, the Arecibo Observatory Radio Telescope located on the island Puerto Rico has the largest spherical multi-reflector antenna in the world. The main collecting dish is 305 m in diameter, is constructed inside the depression, and the backup structure of it is the network of steel cables strung across the underlying karst sinkhole [3]. The only one Radio Optical Telescope in the world ROT-54/2.6 located in Armenia on the mountain Aragats has the second largest double-reflector spherical antenna. ROT-54/2.6 has been designed and constructed in Radiophisical Measurements Institute (Yerevan, Armenia) managed by famous Armenian scientist Paris Herouni in 1987 [4]. The main collecting dish is 54 m in diameter and is constructed inside the rock depression. It has a spherical shape and its surface consists of 3716 solid panels, specially melted and processed with high accuracy. The application areas of both these large double-reflector spherical antennas are radio astronomy and deep space communication.

In 2016 the Five-hundred-meter Aperture Spherical Telescope (FAST) in the Pingtang county in southwest China's Guizhou province was completed and became the largest in the world nowadays. Being 500 meters in diameter, the Radio Telescope is also nestled in a natural basin. Generally speaking, the working surface of the FAST antenna is not spherical but parabolic mirror constructed from special panels [3]. In such highly directional antenna systems of presented radio telescopes, the most optimal characteristics can be achieved only when the field distributions in the antenna aperture in terms of amplitudes and phases are close to uniform. These large dimensional antennas can have significant deformations of their backup structure and that has a direct effect to the filed distribution in the aperture of antenna which, in turn, affects the beam pattern and intensity. The associated wave-front deformation of the imperfections may be of

both systematic and random nature, as well as of both of them. Systematic wave-front deformations usually produce a deformation of the main beam and the profile close to the main beam and a decrease in main beam intensity; random wave-front deformations usually produce an intensity decrease of the main beam and a much extended and more or less intense Gaussian type error beam. In the general situations the deformations consists of spatially small-scale random deformations, which usually do not change the structure of the beam pattern and the focus and pointing, and large-scale deformations, which may do so [5].

The main restriction when constructing antenna system is the phase distortion tolerance in the antenna aperture, which should be less than $\pi/2$ [6]. The ROT-54/2.6 antenna design conditionally can be divided into following parts (Fig. 1): large fixed spherical reflector 1, the small reflector 2 which moves with the help of construction 3 around the centre of the sphere.

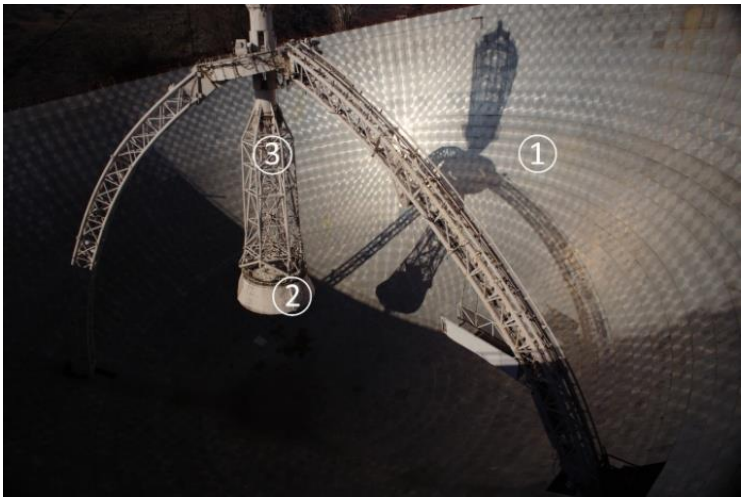


Fig. 3: Overall view of ROT-54/2,6 antenna construction.

The reflecting surface of the large reflector is the hemisphere of 54 m in diameter. Surface panels are casted from aluminium alloy and have spherical profile. The panels have a small gap between each other to ensure that thermal deformation of one panel will not affect

the neighbour panels. The average size and weight of panels are accordingly 1100x1100 mm and 55 kg respectively. Overall quantity of panels is 3716. On the opposite side of panels, stiffening ribs exist to ensure stiffness of panels. The small reflector has a complex profile. In the focus of small reflector the feed and the supporting structure for receiver is mounted. The reflecting surface of small reflector is composed from titanium panels. The small reflector has the following dimensions: the deepness is 2643 mm and the aperture diameter is 5688 mm. In this paper the dependence of ROT-54/2.6 antenna parameters in the aperture of large reflector on accuracy of constructive elements is examined.

**A theoretical research of the errors joint influence on the phase distortion**

In highly directional antenna systems, the optimal characteristics can be achieved if the field distribution on the antenna aperture in terms of amplitude and phase are close to uniform. However, in real case, field distribution differs from uniform one because of several reasons.

One of the main reasons causing the non-uniform distribution of field in aperture is the surface error of reflectors and other constructive elements of the antenna system. When the antenna dimension significantly exceeds the wavelength, in antenna theory, the methods of geometrical optics become applicable. In this case the reflecting mirrors should provide the uniform distribution of the filed in the antenna aperture, i.e. the distances which each beam passes from feed to aperture being reflected by two mirrors should be equal. Regardless of reflectors profile and quantity the following equation can be written:

$$\sum x_i - \sum c_i = 0 \quad , \tag{1}$$

where: $c_i$ is the path of central beam in the mirror system, $x_i$ is the same for current beam. The parameters $c_i$, $x_i$ are functions of the antenna constructive parameters, thus Eq.1 can be considered as an expression for uniform phase distribution in the aperture. For real antenna, the geometrical dimensions would differ from calculated

values. Correspondingly, parameters $c_i$ , $x_i$ would differ also from the calculated ones. The difference of the beams can be expressed as follows:

$$dS = dS_\theta - dS_o , \tag{2}$$

where

$$\left.\begin{aligned} dS_\theta &= \sum dx_i \\ dS_o &= \sum c_i \end{aligned}\right\} \tag{3}$$

The electrical length of

$$dS = \frac{d\varphi}{d\pi}\lambda , \tag{4}$$

where $\lambda$ is a wave length and $d\varphi$ is a phase distortion. The limits for phase tolerance on the antenna aperture in antenna theory is $\pm\frac{\pi}{4}$, thus the limiting deviations would be $\pm\frac{\lambda}{4}$.

In Fig. 2 the main spherical reflector 1 and the corrective small reflector 2 are shown, the point of the system focus is F, the current point is M of phase front line in the aperture, and created beam has the length of a, b and r. All parameters are shown taking into consideration the misalignments. Also, there are the following notations:

$x_0Oy_0$ is the fixed coordinate system. The coordinate system centre matches with the centre of large hemisphere;

$vOu$ is the movable coordinate system;

$xO_2y$ is the fixed coordinate system regarding small corrective reflector; x,y,u,v are the coordinates of current point of the small corrective reflector, in the corresponding system coordinates;

$x_0, y_0$ are the small corrective reflector centre "$O_1$" moving coordinates in the system coordinates $x_0Oy_0$;

e is a point in the axis of small corrective reflector; f is the distance of focus from point "$O_1$";

$x_e$ is the distance of point "e" from the top of the smallcorrective reflector;

$U_e$ is the distance of point "e" from axis "OV";

$U_f$ is the distance of focus from axis "OV";

$\gamma$ is the angle of rotation of small corrective reflector over point "e".

Taking into consideration Eq.3, the following equation can be written:

$$dS_\theta = dn + db + da \tag{5}$$

In addition, we have:

$$\left.\begin{aligned} n &= \frac{Cos\theta}{Cos(2\theta - \theta_1)} R \\ a &= \sqrt{(V_f - V)^2 + (U_f - U)^2} \\ b &= \sqrt{(n_1 - V)^2 + (r_1 - U)^2} \\ U_0 &= y_0 Cos\psi - x_0 Sin\psi \\ V_0 &= y_0 Sin\psi + x_0 Cos\psi \\ V_e &= V_0 + \sqrt{e^2 - (U_e - U_o)^2} \end{aligned}\right\}$$

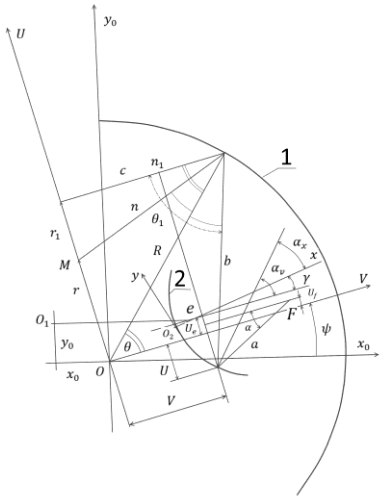


Fig. 4: Design scheme of a double reflector spherical antenna.

In Eq.6 the parameter $\alpha_x$ is the angle between the small corrective reflector current point normal $dS_\theta$ and the axis $O_2x$.

$$
\left.
\begin{aligned}
V_f &= V_0 + \sqrt{f^2 - (U_f - U_0)^2} \\
V_{02} &= V_e - x_e Cos\gamma \\
U_{02} &= U_e - x_e Sin\gamma \\
V &= V_{02} + xCos\gamma - ySin\gamma, \\
U &= U_{02} + yCos\gamma + xSin\gamma \\
\alpha_V &= \alpha_x + \gamma \\
\theta_1 &= 2\alpha_x + 2\gamma - \alpha \\
\alpha &= arc\tan\frac{U_f - U}{V_f - V} \\
\theta &= \theta_1 + arc\sin\left(\frac{U}{R}\cos\theta_1 - \frac{V}{R}\sin\theta_1\right) \\
n_1 &= R\cos\theta \\
r_1 &= R\sin\theta
\end{aligned}
\right\} \qquad (6)
$$

Parameters x and y can be calculated from the following equations [6]:

$$\left.\begin{aligned} x &= A - l - p\cos 2\theta \\ y &= B - p\sin 2\theta_1 \\ A &= 1 - 2(1-\cos\theta)cos^2\theta \\ B &= sin\theta - (1-cos\theta)sin2\theta \\ p &= \frac{1}{2}\frac{c^2 - (A-f)^2 - B^2}{c-(A-f)cos2\theta - Bsin2\theta} \\ c &= 1 - 2l + f \end{aligned}\right\} \quad (7)$$

where l is the distance between the vertex of the small corrective reflector and the center of the large hemisphere. Taking into consideration Eqs. 2–3, Eqs. 5–6 , the total differential of $dS$ can be expressed as follows:

$$\begin{aligned} dS &= 2cos\theta dR - 2dR_\zeta + 2sin^2\theta cos\psi dx_0 + \\ &+2sin^2\theta sin\psi dy_0 + 2sin^2\theta de - (sin2\theta - sin\alpha)dU_e + \\ &+(cos2\theta + cos\alpha - 2)dx_e - (cos2\theta + cos\alpha)dx + 2dx_\zeta - \\ &-(sin2\theta - sin\alpha)dy - sin\alpha dU_f - (1-cos\alpha)dm + \\ &+(esin2\theta - sin\theta + msin\alpha)d\eta \end{aligned} \quad (8)$$

where

$$\left.\begin{aligned} m &= f - e \\ d\eta &= Rd\gamma \\ \alpha &= arcsin\left[\frac{y}{\sqrt{(f-x-l)^2 + y^2}}\right] \end{aligned}\right\} \quad (9)$$

$dR_\zeta$ is the error of large hemisphere at some point of its surface, when the point is located on the axis of small corrective reflector.

$dX_y$ is the error of small corrective reflector surface on the axis $O_2x$.

In the Eq. 8 phase deviations are calculated from the intersection of central beam with the antenna's aperture plane, i.e. $\theta = x = y = r = 0$.

The Eq. 8 can be used to study systematic errors. For the current point of $\theta$ equation gives the linear dependency of phase deviation on errors of the antenna construction, however, the phase deviation on the antenna aperture is non-linear. The influence of each constructive error can be calculated separately assuming that other types of constructive errors do not exist.

The phase deviation dependency $dS$ from the antenna aperture plane coordinates for each $dx_n$ errors is shown in the Fig. 3.

The curves for $\Delta x$ and $\Delta x_1(\Delta y, \Delta y_1)$ show the constructive error influence of $x(y)$ coordinate on phase distortion. The curve $\Delta x(\Delta y)$ takes into consideration the situation when the point of small reflector has constant error equal to 1 over $x(y)$. Curve $\Delta x_1(\Delta y_1)$ shows the situation when errors change according to the law:

$$\Delta x = \frac{x}{x_1}\Delta x_1$$

$$\Delta y = \Delta x_1 tg2\theta \frac{x}{x_1}$$

Random errors can be expressed using the RMS summation. If $\sigma$ is the RMS error of the beam traveling distance from the antenna aperture plane to the focus and $\sigma_i$ is the RMS error of corresponding constructive elements, then:

$$\sigma^2 = 4(cos\theta - 1)\sigma_R^2 + 4\sin^4\theta\cos^2\psi\sigma_{x_0}^2 + 4\sin^4\theta sin^2\psi\sigma_{y_0}^2 +$$
$$+4\sin^4\theta\sigma_e^2 + (\sin 2\theta - \sin\alpha)^2\sigma_{U_e}^2 + (\cos 2\theta + \cos\alpha - 2)\sigma_{x_e}^2 + \quad (10)$$
$$+(1-\cos\alpha)^2\sigma_m^2 + sin^2\alpha\sigma_{U_f}^2 + (\cos 2\theta + \cos\alpha)^2\sigma_x^2 +$$
$$+4\sigma_{x\zeta}^2 + (\sin 2\theta - \sin\alpha)^2\sigma_y^2 + (e\sin 2\theta - \sin\theta + m\sin\alpha)^2\sigma_\eta^2$$

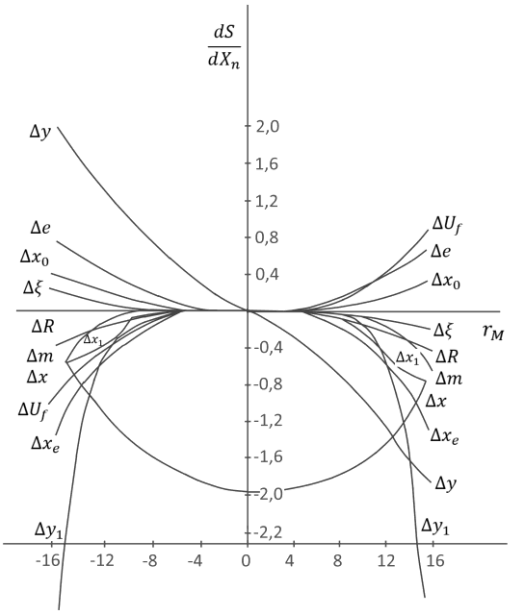


Fig. 5: The curves of phase deviation on the antenna aperture plane.

**ROT-54/2.6 radio telescope temperature deformations caused by evenly heating**

When real antenna is evenly heated, every separate element of construction is resizing strictly according to a specific law. Due to material differences, the conditions of equality of relational elongations are not ensured. This may cause the phase distortion in the antenna aperture plane.

The study of evenly heating is done for the following values of the antenna parameters (Fig. 4):

$R = 27000mm$, $l = 0,49R$, $f = 0,63R$

The foundation for the antenna is a reinforced concrete hemisphere with an internal radius of $R_1 = 28800mm$ and a wall thickness of $B_1 = 1500mm$. The main spherical reflector consists of separate shields with $b_1 = 60mm$ thickness. The shields are fixed on individual steel supports with a height of $H = 1740mm$. The movement system of small reflector with supported structure is also made of steel. The distance between main reflector axis of symmetry to the small reflector supporting structure foundation is $H_1 = 20000mm$. The small reflector is joined with mobile metalwork at a distance of $e = 14500mm$ from the center of the main reflector.

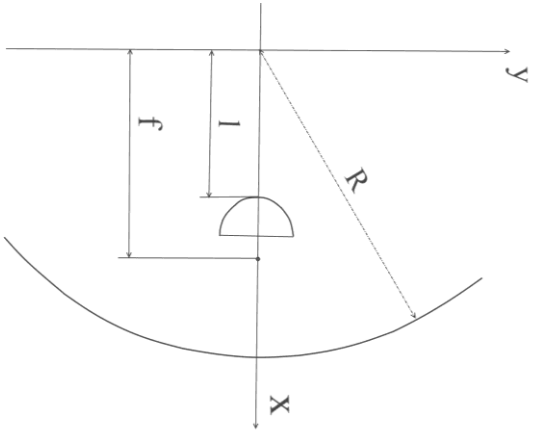


Fig. 6: The schematic view of parameters R, l and f.

For the moderate temperature range the errors of construction can be determined as follows:

$$\Delta x_i = x_i \beta_j t \tag{11}$$

where $i$ is the current number of the construction element, $j$ is the material, $x$ is the corresponding dimensions, $\beta$ is the coefficient of

linear expansion, $t$ is the temperature of uniform heating calculated from a certain average temperature.

The study of ROT-54/2.6 antenna shows, that, due to heating, reinforced concrete hemisphere inner radius changes according to the law [6]:

$$\Delta R_1 = 0,742 R_1 \beta_{r.c.} t \tag{12}$$

Due to asymmetry of small reflector supporting structure, uniform heating will cause the following error:

$$\left.\begin{aligned} \Delta y_0 &= 0 \\ \Delta x_0 &= 0,258 \frac{R_1^2}{H_1} \beta_{r.c.} t \end{aligned}\right\} \tag{13}$$

Obviously, the main reflector radius expansion will correspond to the linear law:

$$\Delta R = \Delta R_1 - \Delta H - \Delta b_1 \tag{14}$$

So, $\Delta R_y = \Delta R = Cosnt$, for every part of surface.

Considering that $\Delta x_y = \Delta U_e = \Delta U_f$

The phase distortion curve on the antenna aperture plane regarding to the function $r = sin\theta$, in the range $-0,5926 \ll r \ll 0,5926$, for the different values of $\psi$ in the range of $-60^0 \ll \psi \ll 60^0$,

where $t$ and $\lambda$ are taken as 1, is shown in Fig. 5. Curves for $\Delta S$ show uniform heating and $\sigma$ curves show random errors.

Fig. 5 shows that $\Delta S$ has the maximum value when $r$ has the maximum value and $\psi$ equals to 0.

So, the temperature range tolerance for the antenna construction elements can be written with quantitative coefficients as follows:

$$\Delta\varphi = \frac{2\pi}{\lambda}\begin{pmatrix} -0.389\Delta R + 0.702\Delta x_0 + \\ +0.702\Delta e - 1.331\Delta x_e - \\ -0.669\Delta x_1 + 1.883\Delta y_1 - 0.629\Delta m \end{pmatrix} \tag{15}$$

For the certain antenna dimensions and materials the temperature range tolerance should be $\pm 1.26\lambda_{deg.}$ ($\lambda$ in $mm$) to ensure that phase distortion is less than $\pm\frac{\pi}{4}$.

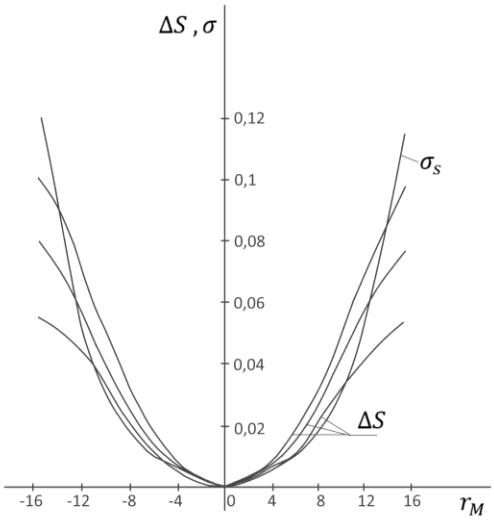


Fig. 7: The curves of phase deviation in the aperture plane.

## Conclusions

In this paper we showed that in the theory of tolerances of large multi-reflector antennas, it is possible to obtain simple working formulas convenient for studying the joint influence of the antenna inaccuracies on phase distortion on the aperture plane with the help of differentials. This is the scientific value of the work.

Final working formulas were obtained for estimating both random and systematic errors of a double reflector spherical antenna with a large mirror diameter of 54,000 mm.

The ways of reducing the phase distortion on the antenna aperture plane are indicated caused by the evenly heating of the ROT-54/2.6 telescope main reflector.

## References

1. Ruze,J. (1966). Antenna tolerance theory - A review.Proc. IEEE, vol. 54, no. 4, pp. 633–640.
2. Baars, J. W. M., Lucas, R.,Mangum,J. G.& Lopez-Perez,J. A. (2007). Near-Field radio holography of large reflector antennas.IEEE Antennas Propag. Mag., vol. 49, no. 5, pp. 24–31.
3. Rico,P., Ii, R. L. W.& Ph,D. (2015). Five-Hundred Meter Aperture Spherical Radio Telescope ( FAST ) Cable-Suspended Robot Model and Comparison with the Arecibo Observatory. Mechanical Engineering Ohio University.
4. Геруни, П. (1990). ИзмеренияхарактеристикРОТ-54/2,6.ВКАИ-5, pp. 22–26.
5. Greve,A. & Bremer, M. (2010). Thermal Design and Thermal Behavior of Radio Telescopes and their Enclosures. vol. 1.
6. Геруни, П. (1980). Разработка вопросов создания государственного эталона поля излучения ГЭПИ-32/54. ВНИИРИ, pp. 23-36.

## A DEVELOPMENT OF SIGNAL PROCESSING ALGORITHM FOR WATER VAPOUR RADIOMETER OPERATING IN INTENSIVE PRECIPITATION

Drozhzhov K.A.[1], Ilin G.N.[2], Ivanov S.I.[1]
[1]Peter the Great St. Petersburg Polytechnic University, St. Petersburg, Russia
[2]Institute of Applied Astronomy of the Russian Academy of Science, St. Petersburg, Russia
[1] E-mail: kirill.drozhzhov@yandex.ru

**Abstract**: The paper presents the results of development of an adaptive signal processing algorithm for the output signal of a water vapor radiometer (WVR) operating in quasi real-time. Land based WVR is used for continuous monitoring of the troposphere parameters, including periods of intensive precipitation. The algorithm is implemented in LabVIEW and uses Singular Spectrum Analysis (SSA) "Caterpillar" method and fuzzy logic techniques.

**Keywords**: remote sensing; adaptive data processing; water vapor radiometer; singular spectrum analysis; fuzzy logic.

## Introduction

Radiometric remote sensing method can measure several important atmospheric parameters such as integral water vapor density, condensed water density in clouds, height-temperature profile of the atmosphere. This data can be used to calculate the "wet" tropospheric delay (WTD) of a radio signal that is important in solution of several scientific and applied problems. The WTD influences the positioning accuracy of the GLONASS national navigation satellite system, it is essential for Very Long Baseline Interferometry (VLBI) data processing and accuracy and reliability of weather forecasts.

Currently WVRs are among the most accurate tools for measuring WTD, providing continuous data in quasi real-time with high time and spatial resolution [1–3]. However, despite its advantages, radiometric method produces anomalous results during periods of intensive precipitation, when the attenuation of a radio signal is significantly increased due to the presence of water droplets or wet snow in the beam. In practice intensive precipitation causes partial or complete loss of accuracy. Depending on the local climate the amount of data lost can reach 25–30 %.

## Water vapor radiometer

The observatories of the Russian VLBI complex "Quasar-KVO" are equipped with troposphere monitoring radiometers [3]. The instruments in the observatories include a water vapor radiometer (WVR), temperature profile meter MTR-5 and weather station MK-15 that allow to monitor the Q and W parameters in real time [1–3]. The block diagram of a radiometric complex of a radio astronomical observatory is shown in Fig.1. WVR and MTR-5 use microwave modulation receivers which register the total power of a radio signal.

WVR has two channels with the central frequencies of $f_1$= 20,7 GHz (channel A) and $f_2$= 31,4 GHz (channel B) that measure the atmospheric brightness temperatures $T_{f1}$ and $T_{f2}$ respectively [1, 2]. MTR-5 is a single channel scanning radiometer with the central frequency $f_3$= 56,7 GHz [1].

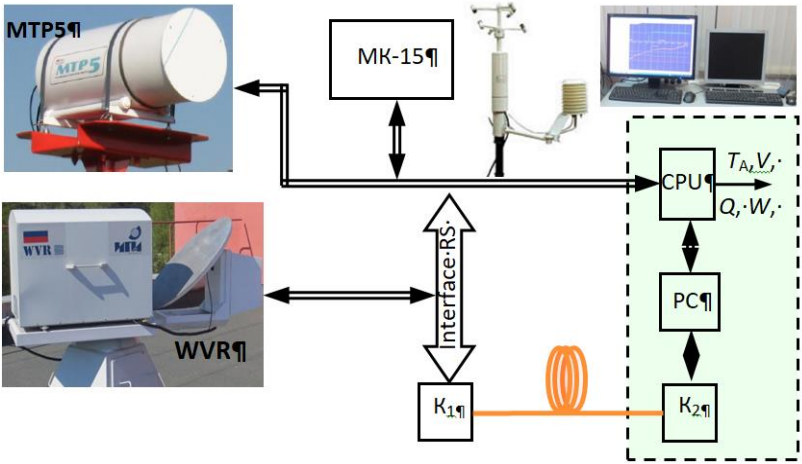


Fig. 1. Functional scheme of the ground-based automated radiometric complex.

Corresponding inverse problems are solved in quasi-real time using information about $T_{f1}$, $T_{f2}$, $T_{f3}$ and current weather conditions [1], giving the values of the $Q$ and $W$ parameters and the tropospheric delay $\tau$.

**Signal processing algorithm for WVR**

Digital signal processor receives a time series of samples of the integral content of water vapor $Q_i$ and information from a precipitation sensor with the period of 60 seconds. A fuzzy logic module determines if the $Q_i$ value is anomalous using Mamdani algorithm [4, 5]. If the current value of Q is not anomalous then the Singular Spectrum analysis (SSA) “Caterpillar” algorithm [6–8] is used to find the dominant trend component of the time series of Q values and suppress the noise component. Otherwise the algorithm works in vector prediction mode using SSA "Caterpillar" method [6, 7]. Our research shows that this approach to the problem produces the most accurate results.

**Examples of WVR signal processing**

Fig.2 shows a comparison of the integral content of water vapor Q obtained using a WVR in a radio astronomical observatory

"Zelentchukskaya" in August 2016 to the GNSS measurements during the same period. As it is shown in Fig.2, during the 48 hour measurement time, intensive precipitation was present for 14 hours and during these periods the signal processing algorithm operated in prediction mode.

The difference between the values of Q measured by two independent methods (WVR and GNSS) in this case is not more than ±0.4 g/cm$^2$ for the whole duration of the experiment. The mean squared error of the difference between the two methods is 0.15 g/cm$^2$. The MSE is not equal to measurement error but its low value demonstrates that the Q values measured by a WVR and GLONASS GNSS are very close.

**Conclusion**

The use of the SSA "Caterpillar" method and fuzzy logic techniques helps to develop an effective algorithm for signal processing in ground based WVR used for troposphere parameters monitoring in quasi-real time. The algorithm helps to reduce the loss of observation time during periods of intensive precipitation without significant loss in measurement accuracy.

The Q parameter measurements made by a ground based WVR and GLONASS GNSS produce similar results. The MSE of the difference between the two methods during 48 hours is 0.15 g/ cm$^2$ (Fig.2).

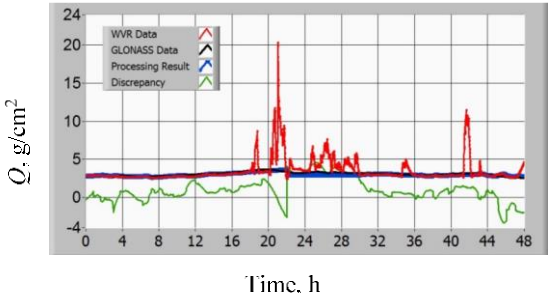


Fig. 2. Time series of WVR data (red), GNSS data (black), processing results (blue) and difference between processing result and GNSS data multiplied by 10 times (green).

## References


1. Il'in G.N., Troitsky A.V. Determination of tropospheric radio signal delay by radiometric method // Radiophysics and Quantum Electronics 2017. V. 60. № 4. P. 326-335.
2. Arsaev I.E., Bykov V.Yu., Il'in G.N., Yurchuk E.F. Water Vapor Radiometer: Measuring Instrument of Atmospheric Brightness Temperature // Measurement Techniques. 2017. V. 60. № 5. C. 1-8. DOI: 10.1007/s11018-017-1224-1.
3. IAA RAS (2017) Available at: http://iaaras.ru/en/ (accessed 09 September 2017).
4. Pedro Ponce-Cruz, Fernando D. Ramírez-Figueroa. Intelligent Control Systems with LabVIEWTM . Springer-Verlag London Limited 2010. 216 p.
5. Jerry M. Mendel, Hani Hagras, Woei-Wan Tan, William W. Melek, Hao Ying. Introduction to type-2 fuzzy logic control : theory and applications. Published by John Wiley & Sons, Inc., Hoboken, New Jersey. Copyright 2014 by IEEE. 356 p.
6. Golyandina N., Nekrutkin V., ZhigljavskyA. Analysis of Time Series Structure. Chapman&Hall/CRC: Roca Raton London New York Washington, DC. 2003. 310 p.
7. Golyandina N., Zhigljavsky A. Singular Spectrum Analysis for Time Series. Springer: Heidelberg New York Dordrecht London. 2013. 119 p.
8. Drozhzhoм K.A., Ivanov S.I. Software implementation of the singular spectrum analysis method in the LabVIEW environment for the task of filtering a random signal // Proceedings of the Conference: Nedelja Nauki Peter the Great St. Petersburg Polytechnic University, Institute of Physics, Nanotechnology and Telecommunications. St. Petersburg, 2016. P. 169-171.

# Section
# Remote Sensing System and Spacecraft Technologies

## A NOVEL PHOTODIODE IN ON-BOARD MICRO RECEIVER IN 400-800 NM RANGE

Dyubo D., Tsybin O.Yu.
Peter the Great St. Petersburg Polytechnical University, St. Petersburg, Russia
E-mail: doobinator@rambler.ru

**Abstract**: On-board electromagnetic radiation sensors require more effective photodetectors. Here, we analyze novel dynamic operation hybrid Gate-PIN photodetector, embedded in an on-board 400-800 nm range microelectronics receiver. Both theoretical and experimental characteristics revealed for that photodetector have allowed designing dynamic scenarios of its operation in optical band, as well as possible applications inside on-board systems. We mention clear temperature dependence, low supply voltage, microscale dimensions, signal integration feature, and other characteristics of the micro receiver with such detector.

**Keywords**: PIN photodiode, spacecraft, remote sensing.

### Introduction

Electromagnetic signals detection, including remote sensing, is one of the most important ways of obtaining information on a spacecraft board. The received signals lying in different ranges of the wide frequency band have a one-dimensional structure or create a two-dimensional image. For instance, in the “Ikonos-2” satellite [1, 2] the optical node includes CCD elements (12 μm x 12 μm) based on Si for panchromatic scanning and Si photodiodes (48 μm x 48 μm) for multispectral scanning. In the “WorldView-2” satellite [3, 4], the optical node includes a CCD elements (8 μm pixel size) based on Si

for panchromatic scanning and CCD elements (32 μm pixel size) for multispectral scanning. Optical visible range and infrared sensors detect the solar radiation reflected or scattered from the Earth and the reflected laser radiation. The detecting occurs in a single spectral channel (IKONOS PAN, SPOT HRV-PAN) or in multi-channel systems (LANDSAT MSS, LANDSAT, SPOT HRV-XS, IKONOS MS, MODIS, MERIS). The hyperspectral "Hyperion" system obtains the images using one hundred or more adjacent spectral bands. This system has potential applications in such fields as coastal area management (for instance, phytoplankton, pollution, changes in bathymetry monitoring) and agriculture (for instance, the monitoring of the health status, moisture and maturity of the crop).

High requirements for the spectral sensitivity, stability, noise level, dimensions and other characteristics are imposed on the space borne radiation detectors, which requires their further improvement. The vacuum photoelectric multipliers possess the highest sensitivity, but they are presented by macro-technological tools only. The photomultipliers do not provide the capability of a parallel two-dimensional image, do not possess mall dark currents and low noise level. They are characterized by insufficient vibration resistance, require high-voltage power sources, and their photocathodes are subjected to degradation. Photoelectron multipliers based on microchannel plates are characterized by unstable operation under ionizing radiation. The conventional semiconductor photodetectors and CCD arrays require high-sensitivity broadband amplifiers and signal integrators, such circuits possess a high noise level. Microelectronics semiconductor photodetectors with a broadband preamplifiers could make losses of low amplitude peaks, increase of electronic noise, appearance of interference, and artifacts. The drawbacks of existing photon detecting devices applied on spacecraft board can be continued.

**Materials and Methods**

Recently, novel hybrid PIN diode with an embedded gate appeared [5]. That device operates in a dynamic regime with the space charge storage and further neutralization, and possesses a high quantum efficiency in visible light range. Presumably, that device has good prospects for use in the weak signals detection in the visible

range, however it has never been evaluated from the point of view of its applying on board a spacecraft. In this paper, the prospects assessment of use an on-board visible range photodetector based on such a hybrid PIN photodiode, operating in a dynamic regime, in the remote sensing systems is provided. The analysis includes the experimental determination of the device characteristics, as well as a theoretical study of the basic physical phenomena providing these characteristics.

The DPD contains two heavily doped p-Si and n-Si regions separated by a slightly doped (or undoped) region, and an embedded metal oxide semiconductor (CMOS) gate located around the p region. A pulsed forward voltage when switching the DPD from the reverse bias causes a large forward current after a significant time delay $T_{trig}$ in the microsecond-millisecond range. The forward current magnitude is controlled only by the value of applied forward voltage, and is independent of the incident light intensity. For instance, the output current of the DPD is 0.8 mA, which is more than four orders greater than the photocurrent magnitude, which is equal to 18 nA in the static regime [5]. In contrast, the time delay $T_{trig}$ is a function of the absorbed light power.

According to the proposed model, the direct current is switched on when a certain amount of electrons $N_{crit}$ is accumulated under the gate in the barrier area [5]. The time delay is defined as follows [5]:

$$T_{trig} = N_{crit}/(G + G_{dark}), \quad (1)$$

$G$ is a coefficient proportional to the absorbed light power at a fixed wavelength, $G_{dark}$ is the self-generation or dark current coefficient. According to this estimation, the dependence of the inverse triggering time $1/T_{trig}$ on the incident light power is linear function. The critical parameter, being of fundamental importance, is the self-triggering temperature dependence caused by the dark current only, in the absence of light. The dark current is formed by the thermal generation of electron-hole pairs in the substrate ($I_{thermal}$) and by the cathode to anode leakage.

The measurement of the photocurrent delay time, instead of its magnitude, provides a new efficient method of light detecting.

In our research, we study novel photodiode temperature dependences and operation processing experimentally and by means of a computer modeling in COMSOL.

**Results**

A physical model of the over space charge barrier current has been developed, which is confirmed by computer simulation. The time delay for the photocurrent switching during the action of the forward voltage is due to the neutralization of the accumulated space charge.

Main characteristics of the device have been obtained, possessing the elimination of a broadband high-sensitivity preamplifier, integrator, and analog-to-digital converter:

- weak photon fluxes integration measurement,
- linear dynamic range of integration,
- certain well-controlled temperature characteristics,
- microscale dimensions,
- possibility of 2D/ 3D imaging,
- low supply voltage (1 volt approx.), and low power consumption,
- predictable reaction on humidity,
- high vibration and shock resistance.

**Conclusions**

The novel results obtained indicate significant opportunities for the new photodetector application in the on-board hardware of spacecraft, including remote sensing systems.

**References**

1. Zevenbergen A. Ikonos and GeoEye-1 // Ground Segment Coordination Body workshop, Frascati, Italy. June 19-20, 2007.
2. Delaney T. Satellite Imagery in Land Development Applications // EOM. Oct. 1999. p. 47-48.
3. Poli D., Angiuli E., Remondino F. Radiometric and Geometric Analysis of WorldView-2 Stereo Scenes // International Archives of the Photogrammetry, Remote Sensing and Spatial Information Sciencesand Remote Sensing. 2010. vol. XXXVIII p. 1-6.
4. Marchisio G., Pacifici F., Padwick C. On the relative predictive value of the new spectral bands in the WorldView-2 sensor // Proceedings of

IGARSS, IEEE International Geoscience and Remote Sensing Symposium. Honolulu, HI, USA, July 25-30, 2010.
5. Okhonin, S., Gureev, M., Sallin, a.o. A dynamic operation of a PIN photodiode // Applied Physics Letters. 2015. vol. 106(3), 031115. doi: 10.1063/1.4906488

# RELATIVE ORBIT AND ATTITUDE COUPLED CONTROL BASED ON SLIDING-MODE VARIABLE STRUCTURE CONTROL

HUO Jun-hai, MENG Tao, JIN Zhong-he
School of Aeronautics and Astronautics, Zhejiang University, Hangzhou, China
huojunhai@zju.edu.cn

**Abstract:** The problem of relative orbit and attitude coupled control of spacecraft formation flying is studied. In this paper, the coupled attitude and orbit nonlinear dynamic model of six degrees of freedom (6-DOF) is proposed. Considering a variety of space perturbations and model uncertainties, power reaching law sliding-mode variable structure control method is used to develop an orbit and attitude coupling cooperative controller, also the finite time convergence is performed using Lyapunov stability method. Numerical simulations are carried out to verify the validity of the proposed controller. The results show that this controller can achieve synchronization control of the relative orbit and attitude, and it provides good control accuracy and stability.

**Keywords:** Formation flying; orbit and attitude control; sliding mode variable structure control

## Introduction

Recently, formation flying using micro satellites appeared to be a new and promising trend. In aerospace industry, this new technology makes way for new and better applications, such as navigation, remote sensing, electronic reconnaissance, stereo imaging, and etc.

Modeling and control for relative orbit and attitude maneuvers are critical technologies in most spacecraft formation flying missions,

and they have received increased attention during the last several years [1–5]. Compared with traditional formation flying control, which usually controls relative orbit and relative attitude separately, this method can take the coupled factors of the relative orbit and relative attitude into consideration. However, these studies do not consider the model uncertainties and external space perturbations and distributions, which cannot be ignored in 6-DOF formation flying control especially for future new formation flying missions where one needs to achieve high accuracy on earth observation and deep space exploration.

In this paper, we address the coupled control for the 6-DOF motion of a follower spacecraft relative to a leader spacecraft using the coupled translation and rotation dynamics. Considering several space perturbations and model uncertainties, power reaching law sliding-mode variable structure control method is employed to achieve coordinated control for formation flying.

**Dynamic model**

In the following analysis, we denote the leader and follower spacecraft by *l* and *f* subscript respectively. The relative orbit dynamic model can be expressed as [6]

$$\dot{v} + C_t(\dot{f})v + D_t(\dot{f}, \ddot{f}, r_f)p + n_t(r_l, r_f) = F_a + F_d \qquad (1)$$

where $C_t(\dot{f}) = 2\dot{f}\begin{bmatrix} 0 & -1 & 0 \\ 1 & 0 & 0 \\ 0 & 0 & 0 \end{bmatrix}$,

$D_t(\dot{f}, \ddot{f}, r_f) = \begin{bmatrix} \frac{\mu}{r_f^3} - \dot{f}^2 & -\ddot{f} & 0 \\ \ddot{f} & \frac{\mu}{r_f^3} - \dot{f}^2 & 0 \\ 0 & 0 & \frac{\mu}{r_f^3} \end{bmatrix}$, $n_t(r_l, r_f) = \mu \begin{bmatrix} \frac{r_l}{r_f^3} - \frac{1}{r_l^2} \\ 0 \\ 0 \end{bmatrix}$,

$\mu$ is constant of earth gravitation, $F_a$ is relative orbit control force, $F_d$ is perturbation force due to external effects, such as earth J2 perturbation etc.

The relative attitude quaternion can be expressed as

$$q = q_f \otimes q_l = \begin{bmatrix} \eta_f \eta_l + \varepsilon_f^T \varepsilon_l \\ \eta_l \varepsilon_f - \eta_f \varepsilon_l - \mathrm{S}(\varepsilon_f)\varepsilon_l \end{bmatrix} \qquad (2)$$

and relative attitude kinematics equation can be expressed as

$$q = \begin{bmatrix} \dot{\eta} \\ \dot{\varepsilon} \end{bmatrix} = \frac{1}{2}\begin{bmatrix} -\varepsilon^T \\ \eta \mathbf{I} + \mathrm{S}(\varepsilon) \end{bmatrix} \omega \tag{3}$$

where $\omega = \omega_{lb,fb}^{fb} = \omega_{i,fb}^{fb} + A_{fl}\omega_{i,lb}^{lb}$ is relative angular velocity between the leader and follower body frame, $A_{fl}$ is the rotation matrix describing rotations from leader spacecraft body frame to follower spacecraft body frame.

Moreover, the dynamics of relative attitude motion is

$$J_f \dot{\omega} + C_r(\omega)\omega + n_r(\omega) = \Gamma_a + \Gamma_d \tag{4}$$

Where $C_r(\omega) = J_f \mathrm{S}\left(A_{fl}\omega_{i,lb}^{lb}\right) - \mathrm{S}\left(J_f(\omega + \omega_{i,lb}^{lb})\right)$ is a skew-symmetric Coriolis-like matrix,$n_r(\omega) = \mathrm{S}\left(A_{fl}\omega_{i,lb}^{lb}\right)J_f A_{fl}\omega_{i,lb}^{lb} - J_f A_{fl} J_l^{-1}\mathrm{S}\left(\omega_{i,lb}^{lb}\right)J_l \omega_{i,lb}^{lb}$ is nonlinear term, and $\Gamma_a$, $\Gamma_d$ are relative attitude control torque and perturbation torque such as gravitational torque, solar perturbation torque, atmosphere drag perturbation, respectively.

Finally, we define the state vectors $x_1 = [p \quad q]^T$ , $x_2 = [v \quad \omega]^T$, so the 6-DOF coupled dynamics of formation flying is

$$\dot{x}_1 = \Lambda(x_1)x_2$$

$$M_f \dot{x}_2 = U + W - C\left(\dot{f}, \omega\right)x_2 - D\left(\dot{f}, \ddot{f}, r_f\right)x_1 - n\left(\omega, r_l, r_f\right) \tag{5}$$

where $M_f = \mathrm{diag}([\mathrm{I}, J_f])$, $C\left(\dot{f}, \omega\right) = \mathrm{diag}([C_t\left(\dot{f}\right), C_r(\omega)])$, $n\left(\omega, r_l, r_f\right) = \mathrm{diag}([n_t\left(r_l, r_f\right), n_r(\omega)])$, $U = [F_a, F_d]^T$, $W = [\Gamma_a, \Gamma_d]^T$, $\Lambda(x_1) = \begin{bmatrix} \mathbf{I} & \mathbf{0} \\ \mathbf{0} & \frac{1}{2}\begin{bmatrix} -\varepsilon^T \\ \eta I + \mathrm{S}(\varepsilon) \end{bmatrix} \end{bmatrix}$, $D\left(\dot{f}, \ddot{f}, r_f\right) = \begin{bmatrix} D\left(\dot{f}, \ddot{f}, r_f\right) & \mathbf{0} \\ \mathbf{0} & \mathbf{0} \end{bmatrix}$

**Controller design**

The control problem is to design a controller that makes the state $x_1$ converge to a time-varying smooth trajectory $x_d$.The desired trajectory can be specified by $x_{d1} = [p_d \quad q_d]^T$, $x_{d2} = [v_d \quad \omega_d]^T$. We define the relative translation error as $\tilde{p} = p - p_d$, the relative rotation error $\tilde{q} = \tilde{\eta} - \tilde{\varepsilon}$ is given by the quaternion product $\tilde{q} = q_d \otimes q$, thus the attitude error dynamics can be written as

$$\dot{q} = T(\tilde{q})\tilde{\omega} = \frac{1}{2}\begin{bmatrix} -\tilde{\varepsilon}^T \\ \tilde{\eta}\mathbf{I} + \mathrm{S}(\tilde{\varepsilon}) \end{bmatrix} \tilde{\omega} \tag{6}$$

Accordingly, the closed-loop system has two equilibrium points in the $(\tilde{q}, \tilde{\omega})$ space which are referred to as the same attitude orientation, namely $\tilde{q}_{\mp} = [\mp 1, \mathbf{0}]^T$. Aiming at minimizing the path length for the desired rotation, for the equilibrium points, we define the relative position and attitude errors as $e_{1\mp} = [\tilde{p}^T, 1 \mp \tilde{\eta}, \tilde{\varepsilon}^T]^T$, $e_2 = x_2 - x_{d2} = [\tilde{v}, \tilde{\omega}]^T = [\mathrm{v} - v_d, \omega - \omega_d]^T$

then

$$\dot{e}_1 = \Lambda_e(e_1)e_2, \Lambda_e(e_1) = \frac{1}{2}\begin{bmatrix} \mathbf{I} & \mathbf{0} \\ \mathbf{0} & \mathrm{sgn}(\tilde{\eta})\tilde{\varepsilon}^T \\ & \tilde{\eta}\mathbf{I} + \mathrm{S}(\tilde{\varepsilon}) \end{bmatrix}\tilde{\omega} \tag{7}$$

Assuming that the leader spacecraft is in control, which means $\Gamma_{al}^{lb} = -\Gamma_{dl}^{lb}$ and $f_{al} = -f_{dl}$, and according to the sliding-mode control theory, we choose the sliding-mode surface function as

$$s = e_2 + c{\Lambda_e}^T(e_1)e_1 \tag{8}$$

The control method is designed as

$$U = -C\left(\dot{f}, \omega\right)x_2 + D\left(\dot{f}, \ddot{f}, r_f\right)x_1 + n\left(\omega, r_l, r_f\right) + M_f\dot{x}_2 - K_2e_2 - \lambda|s|^{\beta}\mathrm{sgn}(s) - K_1{\Lambda_e}^Te_1 \tag{9}$$

where c, $K_1$, $\lambda$ is constant positive matrix, and

$$K_2 = M_f c\begin{bmatrix} \mathbf{I} & \mathbf{0} \\ \mathbf{0} & \pm\frac{1}{4}(\tilde{\eta}\mathbf{I} + \mathrm{S}(\tilde{\varepsilon})) \end{bmatrix}$$

**Proof**

We choose the following Lyapunov function

$$V = \frac{1}{2}s^TM_fs + \frac{1}{2}{e_1}^TK_1e_1 \tag{10}$$

The differentiation of this function along the trajectories of the system results in

$$\dot{V} = s^TM_f\dot{s} + {e_1}^TK_1\dot{e}_1 = s^TM_f\left(\dot{e}_2 + c\left({\Lambda_e}^T(\dot{e}_1)e_1\right)\right) + {e_1}^TK_1{\Lambda_e}^T(e_1)e_1 =$$

$$= -s^T\lambda|s|^{\beta}\mathrm{sgn}(s) - {e_1}^T\Lambda_e(e_1)c^TK_1{\Lambda_e}^T(e_1)e_1 \tag{11}$$

$\lambda > 0$, $c > 0$, $K_1 > 0$, thus $\dot{V} \leq 0$. We can know from (9) that there is only one equilibrium point which can make us sure that $\dot{V} = 0$ among all the point sets $E = \{(s, e)|\dot{V} = 0\}$, and this point is (0, 0), namely *ep*. According to Lasalle's invariant set theory, the system is uniformly asymptotically stable for the equilibrium point *ep*.

**Simulations**

In this section, numerical simulations are conducted to evaluate the performance of the proposed controller, and $p_{df} = [5\sin(\omega_0 t), 5\cos(\omega_0 t), 0]$km, which means the follower is assumed to be commanded to track around the leader in a circular orbit of radii 5 km, and $\omega_0 = 0{,}011\mathrm{rad/s}$ means orbital angular velocity. The moment of inertia is $J_f = J_l = \mathrm{diag}([1.1, 1.1, 1.6])\mathrm{kg}m^2$, the initial attitude quaternion is $q_0 = [0.03, 0.19, 0.27, 0.9]$, the initial relative position is $p_0 = [-0.7, 1.8, 0.04]$km, the initial angular velocity is $\omega_{0f} = [0.02, 0.04, 0.05]\mathrm{rad/s}$. Furthermore, the controller parameters are $K_1 = \mathrm{diag}([0.01,\ 0.01,\ 0.01,\ 0.01,\ 0.01,\ 0.01])$, $\beta = 0.3$, $c = \mathrm{diag}([0.4,\ 0.4,\ 0.4,\ 1,\ 1,\ 1])$, $\lambda = \mathrm{diag}([0.02,\ 0.02,\ 0.02,\ 0.02,\ 0.02,\ 0.02])$. Then, simulations have been carried out under the given initial conditions and the designed control system, as shown in figures 1–4.

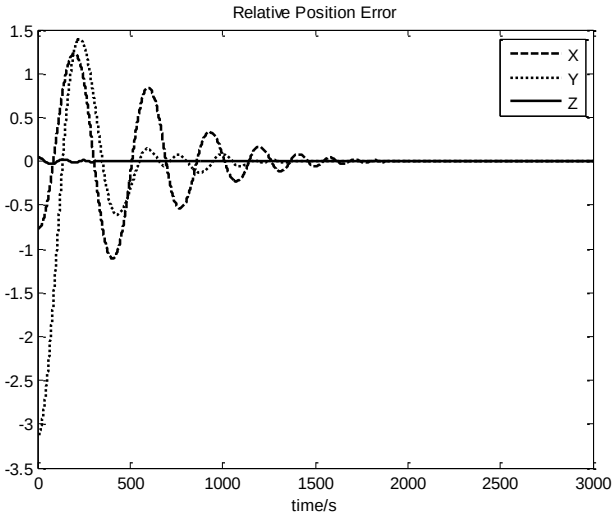


Fig.1. Relative position error.

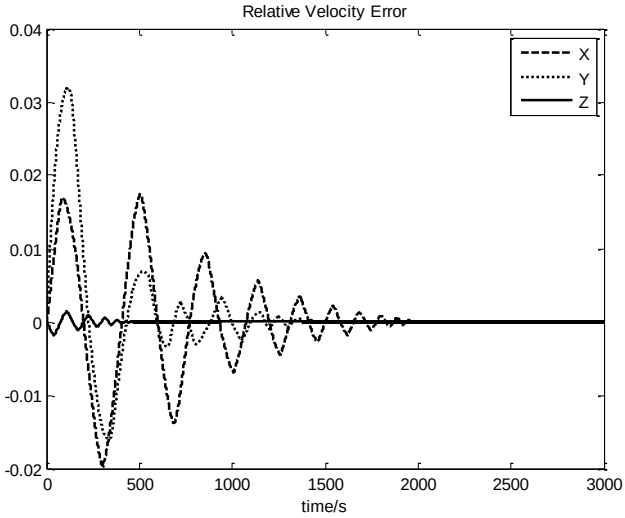


Fig.2. Relative velocity error.

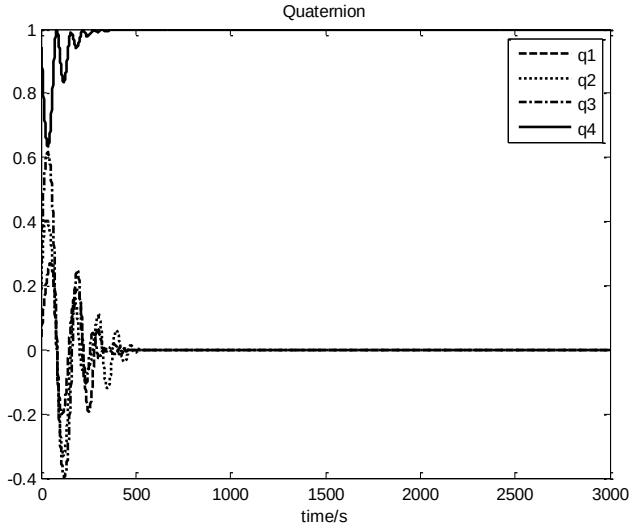


Fig.3. Relative attitude quaternion.

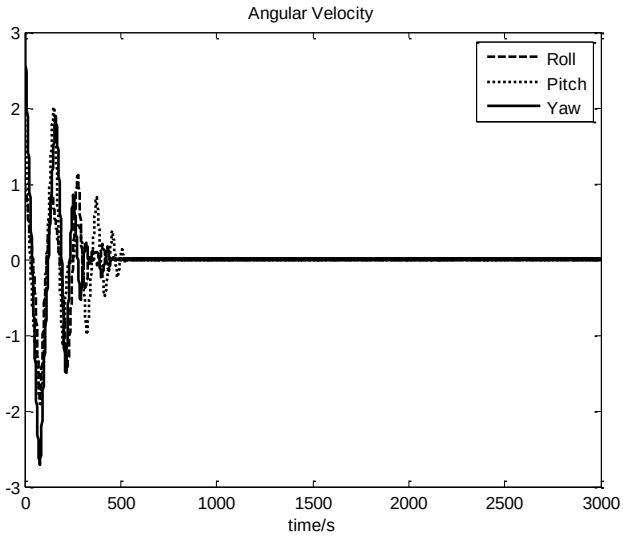


Fig.4. Relative angular velocity.

Table 1. Simulation control errors (3σ)

| | **Relative position Error (m)** | **Relative velocity Error (m/s)** | **Relative angular velocity error (rad/s)** |
|---|---|---|---|
| X | 0.013 | 0.003 | 0.012 |
| Y | 0.022 | 0.002 | 0.025 |
| Z | 0.041 | 0.005 | 0.017 |

The figures 1–4 show that the proposed controller is effective in maneuvering the follower spacecraft into the desired position and attitude and it can achieve the synchronized control of relative orbit and attitude. Table 1 illustrates that the control error of relative orbit and attitude is very small, which means the control system has good accuracy under model uncertainties and external disturbances.

## Conclusions

A coupled 6-DOF cooperative control law is proposed on a basis of power reaching law sliding-mode variable structure control theory, in which external perturbations and model uncertainties are considered. As sliding-mode is recursively Lyapunov stable, the

closed-loop system stability is achieved. Simulation results demonstrate that control system is able to converge with fine performance.

## References


1. Wu Y H, Cao X B, Xing Y J, Zheng P F, Zhang S J. A Survey of Coupled Control for Spacecraft Formation Flying[C], 3 rd Int. Symposium on Flying, Missions and Technologies, 2008, Netherlands.
2. Gaulocher S. Modeling the coupled translational and rotational relative dynamics for formation flying control[C]. AIAA Guidance, Navigation, and Control Conference and Exhibit. San Francisco, California, 2005. AIAA 2005-6091.
3. Wu Yunhua, Cao Xibin, Relative Orbit and Attitude Integrated Coupled Control for Formation Satellite [J]. Journal of Nanjing University of Aeronautics & Astronautics, 2010, 42(1), 13-20.
4. Wang Jianying, Liang Haizhao, Sun Zhaowei, et al. Relativemotion coupled control based on dual quaternion [J]. Aerospace Science and Technology, 2013, 25(1): 102-113.
5. Zhang Haitao, Mei Jie, Coupled distributed adaptive coordinated control for relative orbit and attitude of multiple spacecrafts[J]. Control Theory & Applications, 2013, 30(9), 1086-1098.
6. Kristiansen, R., Grøtli, E. I., Nicklasson, P. J., & Gravdahl, J. T. (2007). A model of relative translation and rotation in leader–follower spacecraft formations. Modeling, Identification and Control, 28(1), 3–14.


# A RELATIVE INFLUENCE OF LOW-FREQUENCY AND MICROWAVE RADIO-OPTICAL RESONANCES IN ALKALI ATOMS VAPOR


Sagitov E.A., Lezhennikova K.A., Semenov V.V., Fatkhutdinova L.I.
Peter the Great St. Petersburg Polytechnic University, St. Petersburg, Russia
E-mail: e-sagitov@mail.ru



**Abstract**: The paper is devoted to the study of the relative influence of low-frequency and microwave signals of the system of two quantum magnetometers based on simultaneous induction of the spin generator signal on the resonance transition and the $M_Z$-signal of the edge

magnetically dependent microwave resonance. The “dressed” atom effect caused frequency shifts of low-frequency and microwave resonances is shown. The frequency shifts ratio of the spin generator to the microwave resonance was between 10 and 100, depending on the experimental conditions. The necessity of the using a circularly polarized low-frequency radio field is shown to reduce the radio-optical resonance frequency shifts caused by the mutual influence of the measuring channels of the magnetometers system.

**Keywords**: quantum magnetometer, optical pumping, frequency stability, alkali atoms, hyperfine structure, frequency shifts.

## Introduction

Quantum magnetometers are used for a wide range of physical experiments, measurements of the Earth's magnetic field and its spatial and temporal changes in geophysical and marine applications and the exploration of minerals.

Such systems as the absolute instruments are widely used for magnetic measurements under unfavorable conditions (at high altitudes corresponding to the orbits of ballistic missiles and artificial Earth’s satellites). So the problem of measuring the magnetic fields of the solar system planets and interplanetary space has become actual.

Another application of quantum magnetometers is based on their sensitivity to rotation. In this way, it is possible to build quantum gyroscopes on their basis, which are devices that allow to detect the rotation of the body and to determine its angular velocity. This possibility is based on the gyroscopic properties of electrons, atomic nuclei and photons.

The results of a study of the relative influence of the quantum magnetometers system measuring channels are presented below. One of the magnetometers was based on a low-frequency spin generator principle, while the second one was built as passive microwave spectrometer with a resonance frequency lock loop [1].

## Relative influence of low-frequency and microwave signals

In the work [2] a research of influence of low-frequency noise on stability of the self-generating magnetometer resonant frequency at

simultaneous registration of a radio optical resonance signal on magnetodependent microwave transition was provided. Similar schemes are applied in the chip-scale atomic clocks using the microwave magnetodependent transition between end magnetic subtotals of a hyperfine structure of a ground state with different values of the complete moment F of an atom [3].

Unlike [3] where the absorption camera with the extreme high pressure of buffer gas was used, experiments [2] were executed on cells with an anti-relaxational covering, in which so-called luminous shift of resonance frequency played an essential role [4]. Its value depends on the polarization of pumping light and the frequency range of the magnetic resonances observed in hyperfine structure of alkali atoms [2]. At the same time resonant character of the applied radio-frequency fields determines inevitable relative influence of the registered signals.

The paper focuses on exploring the possibility of minimizing the frequency shifts of the measuring module, which are not related to the magnetic field variations and the pumping light. The origin of such shifts is due to the phenomenon of *coherence circulation* between sublevels in the hyperfine structure of the atomic system under the conditions of simultaneous action of microwave and low-frequency fields, causing magnetic dipole transitions between magnetic sublevels of the ground state, i.e. the position of atoms in states with different total moment values. Wherein, in accordance with the concept of a "dressed" atom, a significant contribution can be made to the observed frequency shift by *the change of the g-factor* that determines the scale of the magnetic splitting, as well as the presence of multiphoton transitions, which connect all the magnetic hyperfine structure sublevels to each other.

The scheme of alkali atoms magnetic dipole transitions in the ground state within the concept of a "dressed" atom is shown in Fig.1.

The amplitudes of the microwave transitions probabilities in the energy structure of the "dressed" atom determine the specific contribution of various magnetodipole transitions to the radio-optical resonance signal. The probabilities of microwave transitions P for different types of resonance (central or edge) are derived taking into account the statistical weight of the transition, which is determined by the population difference between the levels.

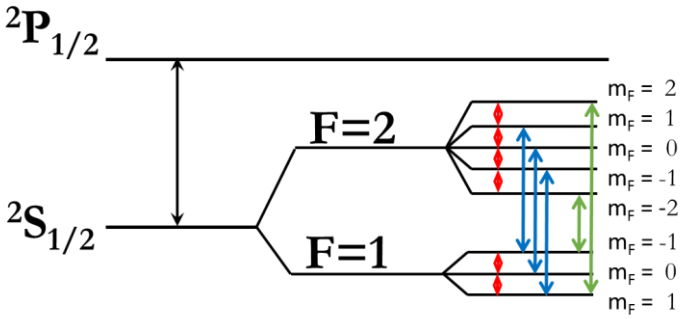


Fig. 1. Magnetic dipole transition of alkali atom ground state. Black arrows − D1 optical pumping line, red arrows − transitions of the spin oscillator, green arrows − microwave edge resonance transitions, blue arrows − microwave transitions in accordance with the concept of the "dressed" atom.

The probability amplitude of such transitions is expressed in terms of the matrix element of the magnetic dipole moment operator M as

$$\langle F^*, m^*|M|F, m\rangle = \sum_{m_1, m_1^*} D^{F^*}_{m_1^*, m^*} D^{F}_{m_1, m} J_0\left[(m + m_1^*)\frac{\omega_1}{\omega}\right]\langle F^*, m_1^*|M|F, m_1\rangle \delta_{m_1, m_1^*+q}\,, \qquad (1)$$

where $D^{F^*}_{m_1^*, m^*}$ and $D^{F}_{m_1, m}$ are Wigner functions, $J_0\left[(m + m_1^*)\frac{\omega_1}{\omega}\right]$ are Bessel functions, $\langle F^*, m_1^*|M|F, m_1\rangle$ is matrix element of a magnetic dipole transition, $\delta_{m_1, m_1^*+q}$ is Kronecker symbol, where the index q takes the value 0 or $\pm$ 1, depending on the direction of the microwave field vector with respect to the direction of the constant magnetic field, $\omega_1 = \gamma H_1$ and ω are, respectively, the amplitude and frequency of the low-frequency radio field.

Table 1 shows the amplitudes of the transition probability in the central and edge series of the absorption spectrum calculated by Eq. (1) for the magnetic microwave resonances of the "dressed" atom $Rb^{87}$.

The probabilities of P transitions were calculated for microwave resonances of the "dressed" atom in the central and edge series of the absorption spectrum of rubidium-87 for the case of a camera with paraffin covering of the walls.

Table 1. Amplitudes of the transition $\langle F^*, m_1^* | M | F, m_1 \rangle$of the atom $Rb^{87}$

| Transition$\langle \boldsymbol{F^*}, \boldsymbol{m_1^*} \vert \boldsymbol{M} \vert \boldsymbol{F}, \boldsymbol{m_1} \rangle$ | Amplitudes of the transition |
|---|---|
| $m^* = 0, m = -m^*$ | $\frac{1}{8}[J_0(\frac{\omega_1}{\omega}) + 3J_0(3\frac{\omega_1}{\omega})]$ |
| $m^* = 1, m = -m^*$ | $\frac{\sqrt{3}}{8}[J_0(\frac{\omega_1}{\omega}) - J_0(3\frac{\omega_1}{\omega})]$ |
| $m^* = \pm 2, m = \pm 1$ | $\frac{\sqrt{3}}{8}[J_2(2\frac{\omega_1}{\omega})]$ |

The experimental value of the Bessel function argument given in Table 1 do not exceed 0.1. In this case taking into account the statistical weight of the population differences, the probabilities ratio of magnetodipole transitions with "0-0" frequency and edge resonance is about $10^2$ for cameras covered with paraffin in the range of $\Gamma^*$ from 1 to 5, which corresponds to the experimental data.

The relative influence of low-frequency and microwave channels on the intensities of the detected signals is shown in Fig. 2, where experimental recordings of the signal of the self-generating magnetometer and the microwave absorption spectrum of $Rb^{87}$ atoms are presented when scanning the frequency of the microwave field.

The nature of the change in the intensity of the signal of the self-generating magnetometer can be explained by the competition of the laser hyperfine pumping process and the process of redistribution of atomic populations caused by the action of the microwave field. It can be seen from Fig. 2 that inducing the edge microwave resonance R1 disrupts the self-oscillations of the self-generating magnetometer (because of atom depolarization), in the case of the edge microwave resonance R2, the intensity of self-oscillations increases, due to the increase in the number of optically oriented atoms interacting with the pumping field.

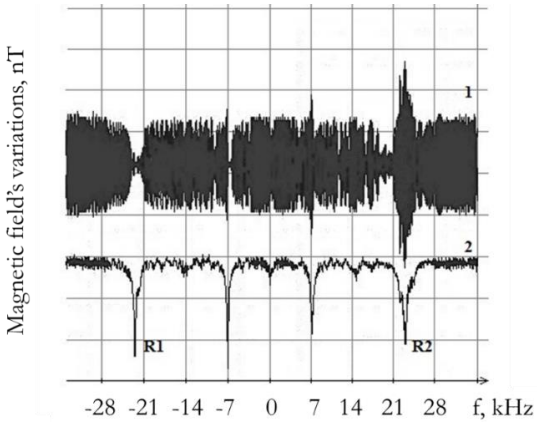


Fig. 2. Recordings of the microwave absorption spectrum and the signal of a self-generating magnetometer on optically oriented pairs of $Rb^{87}$ in a magnetic field of 1 μT: 1 – self-oscillating magnetometer signal, 2 – the signal of the absorption radio-optical resonance under conditions of scanning the frequency of the microwave field. The absorption signals of R1 and R2 correspond to edge resonances at transitions between the HFS sublevels, F = 1, $m_F$ =1 ↔ F = 2, $m_F$ = 2 and F = 1, $m_F$ = -1 ↔ F = 2, $m_F$ = -2 respectively.

The role of the coherence circulation in the HFS was tested in two modes of operation: 1) measuring the frequency shifts of the self-generating magnetometer with a fixed frequency detuning of the microwave field; 2) measurement of the shifts in the frequency of microwave resonance for fixed changes in the frequency of the spin generator. The experiment showed a dramatic difference between the relative influence of low-frequency and microwave signals when operating in different modes: with the same artificial deviations, the ratio of the frequency shift of the spin generator to that of the microwave one is $10–10^2$, depending on the experimental parameters.

**Conclusion**

It can be stated that in the considered version of the system of two quantum magnetometers, it is preferable to use a circularly polarized low-frequency radio field, which makes it possible to minimize the shifts in the radio-optical resonance frequency caused by the relative influence of the measuring channels.

## References


1. A. A. Baranov, S. V. Ermak, E. A. Sagitov, R. V. Smolin, V. V. Semenov. Double resonance frequency light shift compensation in optically oriented laser-pumped alkali atoms // Journal of Experimental and Theoretical Physics. – 2015. – V.121, № 3. – P. 393-403.
2. A. A. Baranov, S. V. Ermak, E. A. Sagitov, R. V. Smolin, V. V. Semenov. Signal correlation in the tandem of a spin oscillator and microwave frequency discriminator with laser-pumped alkali atoms // Technical Physics Letters. - 2016, V.42, №4, - P.38-45.
3. Y.-Y Jau, A.B. Post, N.N. Kuzma, A.M. Braun, M.V. Romalis and W. Happer Intense, Narrow Atomic-Clock Resonances // Phys. Rev. Letters - 2004.- v.92.- №11, P.110801-1 – 110801-4.
4. W. Happer, B.S. Mathur, Effective operator formalism in optical pumping // Phys. Rev.- 1967.- v163.- №1, P.12-25.

# Section Satellite Communications, Navigation Systems and Technologies

## A NEW FAST ALGORITHM FOR MICRO-SATELLITE ATTITUDE DETERMINATION BASED ON PANORAMIC ANNULAR LENS

Chen Lu, Wang Hao, Wang Bendong
Micro-Satellite Research Center, Zhejiang University, Hangzhou, China
E-mail:lynlur@163.com

**Abstract**: A new fast attitude determination algorithm based on panoramic annular lens has been developed. The panoramic annular lens is used as the static infrared sensor, which forms a large field of view to get the infrared image of the Earth. The algorithm of PAL projects the image points onto the virtual earth formatting a space circular loop. The points on this loop are used to construct the spatial vectors. Through the cross product of these spatial vectors, the micro-satellite direction vector can be estimated. This algorithm abandons the iterative process, which reduces the calculation time to meet the demand of rapid maneuver of micro-satellite.

**Keywords**: micro-satellite, attitude determination algorithm, static infrared earth sensor.

### Introduction

Nowadays, the typical micro-satellite attitude determination algorithm of infrared earth sensors consists of Hough transformation and Least Squares fitting [1], and its iteration process is inevitable. Although the accuracy is increased, it takes a large amount of computation time and poses a serious problem for the rapid movement

of micro-satellite [2–4]. In this research, a new attitude determination method of a panoramic annular lens (PAL) sensor has been developed which compensates the distortion and reduces the operation time. The PAL is used to construct the static infrared sensor, which forms a large field of view to get the infrared image of the earth. Then this algorithm projects the image points onto the virtual Earth, and the points are divided into different groups to construct the spatial vectors. Through the multiplication cross, a set of satellite direction vectors is obtained. The micro-satellite direction vectors are distributed normally, thus micro-satellite attitude angle can be estimated by the average number of direction vectors according to maximum probability. The experimental results show the improvement of new algorithm performance.

**Spatial vector algorithm**

The static infrared earth sensor testing system is shown in Fig.1. The PAL is used as the static infrared sensor [5, 6], which forms a large field of view to get the infrared image of the earth. Upper computer sends the rotation angle to the rotary table, and then the PAL obtains infrared earth images at different angles. Through the processing of DSP the infrared earth image data are transferred back to the upper computer.

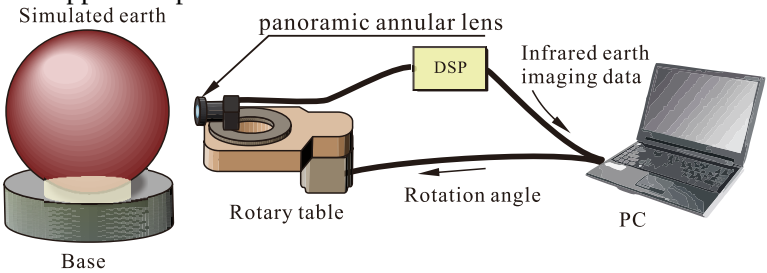


Fig.1. Static infrared earth sensor testing system.

The imaging principle of PAL sensor is

$$y = f \cdot \theta \tag{1}$$

The imaging of PAL sensor is positively correlated with angle $\theta$. Therefore, no matter what direction the sensor moves, the earth imaging faces are the same, as shown in Fig.2.

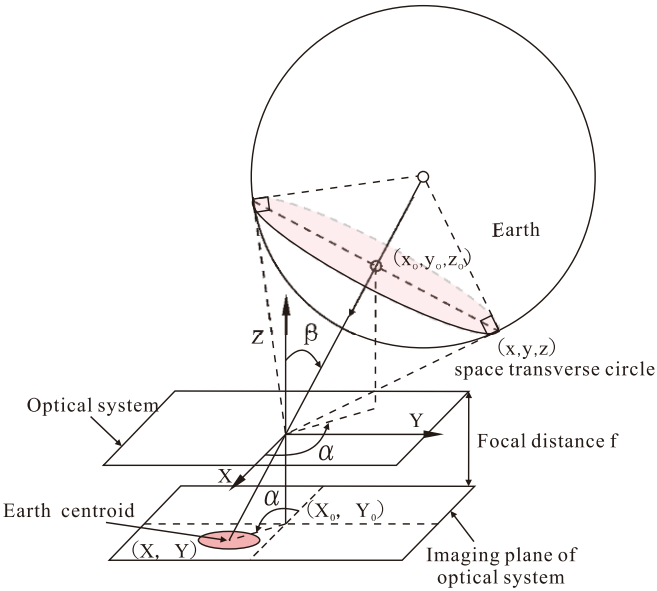


Fig.2. Diagrammatic sketch of PAL imaging.

The imaging point on the imaging plane of the optical system is (X, Y), and the goal of the system algorithm is to obtain β values by means of (X, Y).

According to the lens imaging formula (1) there is

$$\sqrt{X^2+Y^2} = f \cdot \theta \tag{2}$$

Then the relationship between the coordinate of imaging position and the three-dimensional direction of infrared imaging can be obtained.

$$x = R\sin(\theta)\frac{\mathrm{X}}{\sqrt{X^2+Y^2}} \tag{3}$$

$$y = R\sin(\theta)\frac{Y}{\sqrt{X^2+Y^2}} \tag{4}$$

$$z = R\cos(\theta) \tag{5}$$

The mapping points of the optical imaging points (X, Y) to the sphere can be represented as points (x, y, z), and the mapping result is a cross section circle.

The space transverse circle is obtained from the distortion of the imaging point, as shown in Fig.3.

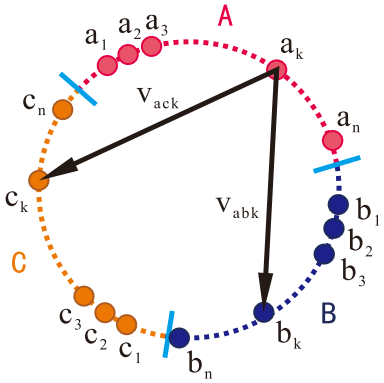


Fig.3. Space transverse circle.

The spatial transverse loop is mapped by the earth's infrared imaging points, and it can be divided into three parts A, B and C. Each part contains n image points, thus three parts can be represented as three sets A= $\{a_1,a_2,a_3\ldots a_n\}$, B= $\{b_1,b_2,b_3\ldots b_n\}$ and C= $\{c_1,c_2,c_3\ldots c_n\}$.

Three points $a_k$, $b_k$ and $c_k$ are selected from three sets, then we connect them together to get two vectors $\mathbf{v_{abk}}$ and $\mathbf{v_{ack}}$ called a spatial vector pair. There can be at least n spatial vector pairs, and they are in the same plane, and that is exactly the spatial transverse plane.

Vectors $v_{abk}$ and $v_{ack}$ are distributed in the same plane, and they are not on the same line. According to vector theory, we can get

$$D=\left\{\mathbf{d}\,|\,\mathbf{d_k}=\mathbf{v_{abk}}\times\mathbf{v_{ack}},\mathrm{k}=1,2\ldots\mathrm{n}\right\} \tag{6}$$

$\mathbf{d_k}$ is perpendicular to the plane of vectors $\mathbf{v_{abk}}$ and $\mathbf{v_{ack}}$, and that is the desired direction vector. In the same way, at least n directional vectors $\mathbf{d} \in D$ can be obtained, which are parallel to each other and perpendicular to the spatial transverse loop.

Then the angle β can be calculated

$$\mathrm{Bt}=\left\{\beta\mid\beta=\arccos\left(\frac{z_d}{|\mathbf{d}|}\right),\mathbf{d}=(x_d,y_d,z_d)\in D\right\} \tag{7}$$

But in fact, the result of distortion is that all the image points are not distributed in the same plane totally, which causes a little

difference in angle β. And it is near normal distribution. In order to solve the problem, the angle β value of the maximum probability near the median is taken, and taking an average of them allows to estimate a more accurate angle β.

In order to obtain higher precision positioning, the traditional algorithm repeats the Hough transform and least squares fitting to remove the noise points. The k-th calculated distance between cross sectional and imaging center of sphere can be recorded as $r_{k.}$ Until the difference between $r_k$ and $r_{k-1}$ is less than the rated value, the iteration process stops and the corresponding β value is output. However, due to the Hough transformation, the least square method, and the iterative process, the calculation becomes pretty complicated, and usually consumes a large amount of time.

**Experimental results and analysis**

The t Actual measurement scene is shown in Fig.4. The turntable is rotated from -10 degrees to 10 degrees, and PAL takes infrared images of the earth at different angles.

Fig.4. Actual measurement scene.

The resulting data is processed by different algorithms. And the angle β between the image axis and the geocentric vector is obtained, as shown in Fig.5.

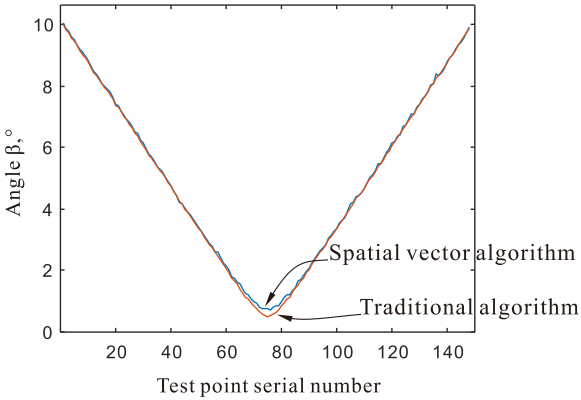


Fig.5. Angle β test results.

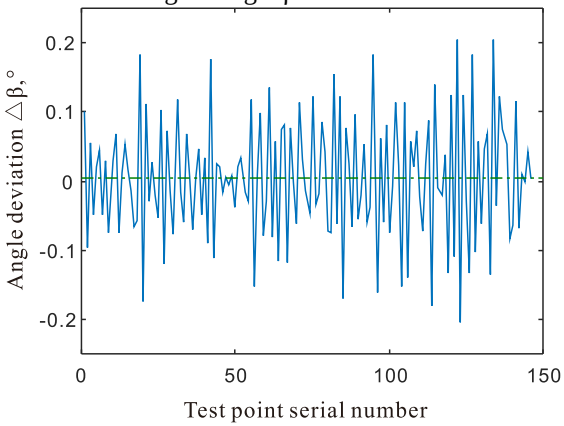


Fig.6. Angle deviation ∆β test results.

The experimental results show that the satellite attitude angles β derived from two algorithms are generally the same, and there is a small deviation near zero. Detailed performance comparisons are shown in the table 1

As shown in the Table 1, the accuracy of new algorithm is almost the same as traditional one, but the new algorithm can improve the efficiency up to nearly 94%.

Table 1. Results of convergence step length

| **Algorithm** | **Average deviation, °** | **Standard variance** | **Computation time, second** |
|---|---|---|---|
| Traditonal | 0.035 | 0.046 | 0.354 |
| Spacial vector | 0.024 | 0.082 | 0.018 |

## Conclusions

This paper presents a new fast algorithm for micro-satellite attitude determination based on PAL. It was shown that the new fast algorithm, namely Spatial vector algorithm, discards the iterative process of the traditional algorithm, but calculates the attitude angle with the vector cross product. The experimental results show that the pose accuracy of this algorithm is about 0.03 degree, and it can improve the efficiency up to nearly 94%. This helps to achieve more accurate and rapid control of micro-satellites.

## References

1. Shen G, Wang H, Guo Z, et al. Design of infrared static focal plane earth sensor for micro-satellite[J]. Chinese Journal of Sensors & Actuators, 2012, 25(5):571-576.
2. Xin L I, Cui W N, Zhou S B. Wide Angle Attitude Measuring Model and Error Analysis of Static-infrared Earth Sensor[J]. Infrared Technology, 2015, 37(1):73-77.
3. Zhang X L, Li F, Zhao J H. New Test System of Infrared Earth Sensor[J]. Applied Mechanics & Materials, 2015, 789-790:536-539.
4. Harry Gross, Carol Bruegge, and Mark Helmlinger. "Unattended Vicarious Calibration of a Low Earth Orbit Visible-Near Infrared Sensor", AIAA SPACE 2007 Conference & Exposition, AIAA SPACE Forum, doi.org/10.2514/6.2007-6088
5. Liu B, Meng L, Hua C. Sensitivity analysis of thermal design of infrared earth sensor for GEO satellites[J]. Spacecraft Environment Engineering, 2013. 30(3):240-244.
6. Wang H, Xing F, You Z, et al. Study of high-precision earth sensor with triple-FOV [J]. Instrumentation, 2014, 1(2):23-29.

# SELECTED CHALLENGES IN SPACE ION PHYSICS RESEARCH AND TECHNOLOGY

Tsybin O.Yu.
Peter the Great St Petersburg Polytechnic University, St. Petersburg, Russia
E-mail: otsybin@rphf.spbstu.ru

**Abstract**: Ion physics in outer space and on-board is under short consideration. We focus on ionization, desorption, ion sputtering, mass-to-charge analysis, particle acceleration and trapped motion in electromagnetic field, electrical propulsion, and so on. A brief analysis of ion mass spectrometry physical background, technologies, and applications in space is provided. Several specific challenging cases present actual tasks of ion technology and mass-spectrometry in space.

**Keywords**: Space, Jet Thrust, Ionization, Desorption, Sputtering, Mass Spectrometry.

## Introduction

Space activities and applications are vital to our society's growth and development. Space research aims to foster a cost-effective, competitive, and innovative space industry, and advanced research community as well. In this context, space policy is an instrument responding to social, economic and strategic types of need. Space ion physics is basic scientific research carried out using novel technologies and scientific equipment in outer space. That includes the use of space technology for a broad spectrum of research and technology fields, including Earth science, materials science, life science, electric propulsion, technical developments, and ion physics. The scientific objectives of expeditions to Planets of Solar system and small objects in space are to study their surface, subsurface and atmosphere, as well as the interaction with the interplanetary medium. Comets and asteroids carry interstellar materials pivotal to understanding prebiotic molecules that could have initiated life on Earth. About one third of the molecules detected in the interstellar medium or circumstellar shells are complex ones, containing six or

more atoms. Using electric energy is especially important because it can be produced on-board by means of the solar radiation conversion. In that content, electrical Hall and ion-based thrusters both have been successfully used for primary propulsion in both deep-space scientific missions and satellite station control. On-board mass-spectrometry (MS) in outer space is most powerful analytical tool for materials science in general, and for investigation of any kind of remote substance like solid state, gases and solutions, in form of atoms and molecules particularly.

**Ion Physics and Jet Engines**

According to the fundamental laws of nature, the jet propulsion apparatus can be realized by ejecting an expendable material agent in the form of combination of electromagnetic field irradiation and massive matter ejection. The required technologies are initiation of reactions by means of electrical energy, effective operation in vacuum conditions with appropriate expendable substances, and production of accelerated particle beams leaving the jet into free space, and originated from the mentioned substances (agents). The ion beam exiting the thruster is often called the thruster plume, and the characteristics of this plume are important in how the exhaust particles interact with the spacecraft. The plume from a thruster typically has a complex structure. This material can deposit on spacecraft surfaces, which can change surface properties such as emissivity, transparency, etc. Electric thrusters propel the spacecraft using the same basic principle as chemical rockets — accelerating mass and ejecting it from the vehicle. The ejected mass from electric thrusters, however, is primarily in the form of energetic charged particles. Electric thrusters provide exhaust velocities higher than those available from gas jets or chemical rockets. For explanation of modern thrusters operation, it is required to describe the fundamental physics of these devices. This is a task requiring basic knowledge of plasma physics, ion accelerators, cathodes, electrical discharges, high voltage, gas dynamics, and many other technologies. The total efficiency is the jet power produced by the thrust beam divided by the electrical power in the system. Electric thrusters are generally described in terms of the acceleration method used to produce the thrust. These methods can be separated into three categories: electro thermal, electrostatic and electromagnetic. Ion

thrusters employ a variety of plasma generation techniques to ionize a large fraction of the propellant. Ion thrusters feature the highest efficiency. Electrostatic thruster of Hall type utilizes a cross-field discharge described by the Hall effect to generate plasma. Such thruster efficiency and specific impulse are somewhat less than that achievable in the ion thrusters, but the thrust at a given power is higher and the device is much simpler and requires fewer power supplies to operate. The most well-known Russian SPT-100 Hall thruster operates nominally at electrical power of 1.35 kW. This thruster includes a redundant hollow cathode to increase the reliability and features a lifetime in excess of 9000 hours. There are many other types of electric propulsion thrusters: electro thermal resistojets and arcjets, electrospray/field emission, pulsed plasma, magneto plasma dynamic, and many others [1].

Indeed, the electromagnetic field radiation reactive force produces mechanical pressure on an *open* resonator, or antenna, as predicted by A. Einstein in 1906, demonstrated experimentally by P.N. Lebedev, and confirmed theoretically elsewhere based on Maxwell's equations in a framework of classical electrodynamics on the conductor boundary [2–5]. However, it is impossible to create a sufficient momentum thrust by means of electromagnetic field with an *open* empty inner volume of a microwave cavity. The maximum pressure force produced by electromagnetic field equals approximately to $|F_{EMF}| \approx 2W/V_g$, where W is a radiation power expanded freely into space, $V_g$ is the group velocity of the wave (which has a value close to the speed of light). The coefficient of 2 appears when the wave incidents from outer space and is re-irradiated back. Excessive input power, approximately 150 MW, is required for notable acceleration values produced by 1N of force. Recently, the idea has appeared for an “EM Drive” which generates a small amount of thrust simply by bouncing microwaves in closed interior volume of a cone-shaped copper chamber. These approach and view are based on an erroneous assumption that, in the steady state excitation regime, a closed cavity, continuously irradiated by microwave power flow, can convert it into unbalanced force and kinetic energy of the motion of closed mechanical system. Of course, such closed system generates

zero radiation of radio frequency power into space; therefore, the jet thrust must vanish [6]. There are no reasons to support the attractive EM Drive concept. There is no serious theoretical explanation for how such an engine might work, and not all possible sources of experimental error were under critical consideration in the article [7]. To put it briefly, such artifacts could be caused by a) radio frequency non-uniform heating of the chamber and b) infrared radiation pressure acting from outer volume on hot walls.

The challenging tasks in the field of ion physics and electrical propulsion could be presented by a novel design of high quality long-life thrusters, their optimum design, protected from any secondary negative effects; selection and preparation of expendable substances; 2D/3D computer modeling of a plume; the practical implementation of desorption and sputtering of the outboard solid-state substances [6]. Other possible applications might involve materials preparation, chemical reactions and building procedures by means of ion technologies on planets' surfaces.

**Space Mass-Spectrometry**

In the human practice on Earth's surface, vacuum mass-spectrometry (MS) is extremely effective, high sensitive and almost universal analytical tool, having wide spread in science, technology, medicine, and many others applications. MS is based on a great deal of fundamental knowledge in any kind of sample collection, ionization, desorption, ion sputtering, principles of charge particles motion in electromagnetic fields in vacuum chambers, determination of ion trajectory, design, and parameters of data acquisition systems, and information technologies. Further, practical MS requires specific experience of applications and "know-how" as well. In outer space missions, MS keeps its outstanding analytical features, so we can expand our knowledge and understanding of universe positively [8]. The space programs include MS for both environmental monitoring and as a tool in on-board medical experiments. Several examples could confirm this idea. The lower atmosphere MS were flown on the USA Pioneer Venus and on the USSR Venera 11 and 12 landers. One upper atmosphere MS was on the Pioneer Venus and one on the Pioneer Venus Orbiter. The last three Apollo flights to the moon carried magnetic MS to detect the presence of an atmosphere and to

determine its composition. MS experiments carried by spacecraft Giotto (Europe), Vega 1 and Vega 2 (USSR), determined the abundances and the chemical, elemental and isotopic composition of the gases and low-energy ions in the coma of Halley's Comet. The Cassini mission to Saturn launched in October 1997 was equipped by MS designed to identify and measure chemicals in Titan's atmosphere. By means of Viking 1, Viking 2 and The Phoenix spacecraft landed on Mars, a number of MS programs were realized there. The Ion Mass Analyzer of Mars Express Orbiter mission was an improved version of the ion mass spectrographs TICS/Freja, IMIS/Mars-96 and IMI/Nozomi and a copy of Rosetta's ICA instrument [8]. An ion MS measured relative abundances of collected ion samples from the ionosphere. Gas Analyzer MS was built for use on Shuttle's biomedical laboratory missions that flew between 1989 and 1995. However, space MS applications require some different approaches to hardware design, sample collection, its processing and analysis, data storage, and utilization. Specific conditions include weight and power limitations, high acceleration and acoustic vibrations during launch, extreme temperature variations and ionizing radiation, remote telecommunications. It is essential that all ionization and detection processes are clear, stable and long-life. Micro-scale size MS are optimal required for space applications with small orbital satellites and deep missions as well, e.g. for the chemical composition and biomarker exploration of planets, asteroids and comets. Hybrid and tandem MS look like emerging promising device for future study of complex molecules in space.

## Conclusion

Ion physics, technology, and mass spectrometry reveal great opportunities in the field of modern and future space investigations. Selected challenges here require a novel design of both ion-based propulsion and ion mass-spectrometry hardware, implementation of advanced ionization, desorption, and ion sputtering schemes, wider using of any natural resources, available in space expeditions.

## References

1. Dan M. Goebel and Ira Katz. Fundamentals of Electric Propulsion: Ion and Hall Thrusters //JPL Space Science and Technology Series, Jet

Propulsion Laboratory, California Institute of Technology. March 2008. 486p.
2. Einstein A. The principle of conservation of the center of gravity movement and the inertia of energy. Ann. Phys. 20, 627-633, 1906
3. Lebedew, P. Über die ponderomotorische Wirkung der Wellen auf ruhende Resonatoren. III. Akustische Hohlresonatoren. - Leipzig, 1897 - 20 S. - (Annalen der Physik und Chemie. Neue Folge. Bd. 62).
4. Von Peter Lebedew. Über die ponderomotorische Wirkung der Wellen auf ruhende Resonatoren. II. Hydrodynamische Oscillationsresonatoren // Annalen der Physik und Chemie. Neue Folge. Bd. 59. 1896. - Leipzig: Johann Ambrosius Barth (Arthur Meiner), 1896. - 18 S
5. Griffiths, David J. (2007), Introduction to Electrodynamics, 3rd Edition; Pearson Education – Problem 9.10.
6. Tsybin, O.Y., Makarov, S.B., Ostapenko, O.N. Jet engine with electromagnetic field excitation of expendable solid-state material // 2016. Acta Astronautica, 129, pp. 211-213. doi:10.1016/j.actaastro.2016.08.022
7. Harold White, Paul March, James Lawrence, a.o. Measurement of Impulsive Thrust from a Closed Radio-Frequency Cavity in Vacuum // Journal of Propulsion and Power, Vol. 33, No. 4, July–August 2017, p.830-841. doi: 10.2514/1.B36120
8. Hoffman, John. H., Griffin, Timothy P., Limero, Thomas., Arkin, C. Richard. Space Applications of Mass Spectrometry. NASA Technical Reports. Chapter 31. February 01, 2010. 130 p. Document ID 20100039433.

## CESIUM ATOMIC CLOCK FOR GLONASS SATELLITE NAVIGATIONAL SYSTEM

Petrov A.A., Davydov V.V., Popov A.S., Lukashev N.A.
Peter the Great St. Petersburg Polytechnic University, St.-Petersburg, Russia
Alexandrpetrov.spb@yandex.ru

**Abstract**: One of the essential elements of satellite navigation system is an atomic clock. The proper operation of any navigation system depends on the performance of atomic clock. Several directions of modernization of the cesium atomic clocks are considered. New design of the frequency

synthesis circuitry is presented. The theoretical calculations and experimental researches showed the decrease of step frequency tuning by several orders and improvement of spectral characteristics of the frequency synthesizer output signal. New magnetic field control unit eliminates one of the most important perturbing factors affecting on long-term frequency stability. Experimental research of the cesium atomic clock metrological characteristics showed the improvement of Allan variance by 10%.

**Keywords:** cesium atomic clock, quantum frequency standard, frequency synthesizer, direct digital synthesis, magnetic field control unit, Allan variance.

## Introduction

Global navigation satellite constellations such as European Galileo, Russian GLONASS, and the USA Global Positioning Systems (GPS) use atomic frequency standards for precision time-keeping and stable frequency generation [1].

One of the central problems of satellite systems is the problem of mutual synchronization of the satellite time scale up to nanoseconds and less. The error of the navigation signals emitted by the different satellites at 10 ns causes an additional error in determining the location of the consumer to 10–15 meters.

The solution of the high-precision synchronization problem of the on-board time scales requires the implementation of highly stable on-board cesium and rubidium frequency standards on satellites, as well as the creation of ground-based devices for comparing time scales.

The concept of development of the space navigation systems and development of the metrological services makes it necessary to modernize the currently used quantum frequency standards or to develop new ones.

Development and commissioning of new atomic clock is very long and costly process, and in most cases there is not enough funds and time. Therefore, in most cases, modernization is needed for specific tasks related to the operating conditions of the frequency standards.

The process of quantum frequency standards modernization includes various directions: changing the weight and dimensions,

reducing energy consumption, improvement of metrological characteristics. For frequency standards, modernization may not be necessary for the whole construction but only for individual units or blocks. In present work several directions of metrological characteristics improvement are considered.

**Several directions of improvement of cesium atomic clock metrological characteristics**

Frequency synthesizer is one of the main blocks of quantum frequency standard. Frequency synthesizer generates the microwave signal at ~9.2 GHz (used to interrogate the $^{133}$Cs atoms hyperfine resonance transition) from the 5 MHz quartz oscillator frequency [1–3].

The main characteristic of the frequency synthesizer is an ability to impact on the characteristic of frequency stability of the quantum frequency standard output signal. Frequency instability introduced by the synthesizer is determined by the lateral discrete spectrum components of the signal that occurs in dividing, multiplying, mixing frequency signals, the accuracy of generated frequency, and the impact of natural and technical noise [5–7].

In order to provide the best possible frequency stability, it is crucial that the microwave signal which interrogates the $^{133}$Cs atoms is as "clean" as possible; that is, free of unwanted sidebands and spurious signals which can cause Bloch-Siegert frequency shifts [1–2].

To meet the requirements for spectral purity of output signal 10 bit DAC was used. It is possible to obtain the suppression of lateral amplitude components in the spectrum of the output signal not worse than -70 dB.

Experimental study showed that the accuracy of present method of generating the frequency synthesizer output signal needs to be increased. The large resolution of step frequency is necessary. New scheme of the frequency synthesizer has been designed by using a method of direct digital synthesis (DDS) [4]. This method allows us to generate the synthesizer output signal within the accuracy about $10^{-5}$ Hz.

In Fig. 1 new design of the frequency synthesizer is presented.

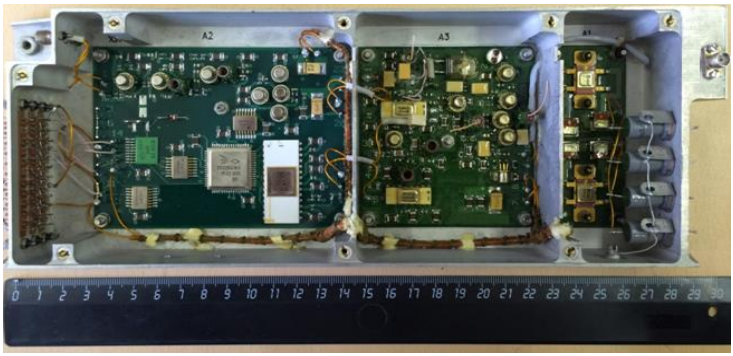

Fig.1. New design of the frequency synthesizer.

In addition, a new design of the frequency synthesizer also allows eliminating one of the most important perturbing factors affecting on long-term frequency stability.

The stable isotope $^{133}$Cs has two hyperfine states F = 4 and F = 3 which are split in the magnetic field into 16 components. In accordance with the selection rules, seven transitions between the components of hyperfine sublevels are possible. The central resonance $|F=3, m_F=0\rangle \leftrightarrow |F=4, m_F=0\rangle$ due to the Zeeman effect exposes a quadratic frequency shift. For a typical value of magnetic field or so-called C-field near 8 uT the frequency shift is 2.7 Hz corresponding to a relative frequency shift of $3 \cdot 10^{-10}$.

The accuracy of the output signal quantum frequency standard is dependent on the shift of the central resonance. It should be noted that not only the central resonance is exposed the frequency shift, but also all six transitions $(3, m_F) \leftrightarrow (4, m_F)$ with $\Delta m_F = 0$. To express these changes as a function of B and atomic constants we used the Bright Rabi equation [1–3].

In order to control any changes of magnetic field a new magnetic field control unit was developed. In modern quantum frequency standards the magnetic field is maintained by the active stabilization system. For this purpose the neighboring transition $|F=3, m_F=1\rangle \leftrightarrow |F=4, m_F=1\rangle$ is used. The method of C-field adjustment is similar to the method of frequency adjustment to the main maximum [1–2].

In this case, the effects, associated with magnetic field changes, such as long-term drift of the current source, temperature dependence, effect of external magnetic field, etc., are excluded.

Experimental research of quantum frequency standards with two new functional blocks includes measuring of the output signal frequency and calculation of Allan variance, which allows to evaluate the frequency instability.

Time dependencies of Allan variance for previously used cesium atomic clock (1) and cesium atomic clock with new frequency synthesizer and new magnetic field control unit (2) are presented in fig.2.

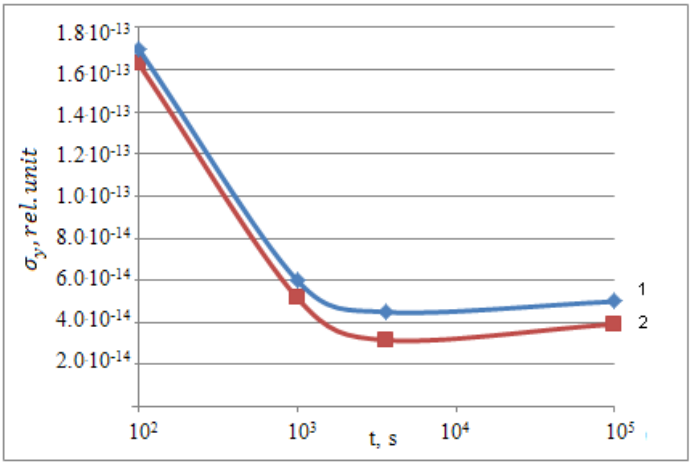


Fig.2. A plot of Allan variance vs time for cesium atomic clock (1) and cesium atomic clock with new frequency synthesizer and new magnetic field control unit (2).

From these results it is clear that the use of new design of the frequency synthesizer and system for stabilizing magnetic field makes it possible to obtain better frequency stability of quantum frequency standard. A pure spectrum of the frequency synthesizer output signal and best resolution of frequency step improved short-term frequency stability. System for stabilizing magnetic field eliminated one of the most important perturbing factors affecting on main metrological characteristic of cesium atomic clock.

## Conclusion

Experimental research of the cesium atomic clock with new design of frequency synthesizer and system for stabilizing magnetic field showed the improvement in main metrological characteristic, being the long-term frequency stability, by about 10%.

## References


1. Riechle, F.: Frequency Standards. Basics and Applications. Wiley-VCH, 526 p. (2004)
2. K. Oduan and B. Gino, Chronometry and Basics of GPS, (Technosphere, Moscow, 2002).
3. V. I. Dudkin and L. N. Pachomov, Quantum Electronics. Devices and Their Applications, (Technosphere, Moscow, 2002).
4. L. I. Ridiko, J. Components and Technology 7, 83 (2005).
5. Petrov A.A., Vologdin V.A., Davydov V.V., Zalyotov D.V. Dependence of microwave – excitation signal parameters on frequency stability caesium atomic clock. Journal of Physics: Conference Series volume 643 (2015) 012087 – proceeding the 2st International School and Conference «Saint – Petersburg OPEN 2015» on Optoelectronics, Photonics, Engineering and Nanostructures.
6. Petrov A. A., Davydov V. V. Improvement frequency stability of caesium atomic clock for satellite communication system. // Lecture Notes in Computer Science (including subseries Lecture Notes in Artificial Intelligence and Lecture Notes in Bioinformatics) Volume 9247, 2015, Pages 739-744 - 15th International Conference on Next-Generation Wired/Wireless Advanced Networks and Systems, NEW2AN 2015 and 8th Conference on Internet of Things and Smart Spaces, ruSMART 2015; St. Petersburg; Russian Federation; 26 August 2015 through 28 August 2015; Code 142759.
7. Petrov A. A., Davydov V. V. New microwave excitation signal generating circuit for quantum frequency standard on the atoms of caesium Cs133. International Journal of Modern Physics: Conference Series Vol. 41 (2016) 1660142.

# A SHORT-SCALE QUANTUM FREQUENCY STANDARD BASED ON TWO QUANTUM MAGNETOMETERS FOR ON-BOARD APPLICATIONS

Sagitov E.A., Ermak S.V., Semenov V.V.
Peter the Great St. Petersburg Polytechnic University, Saint Petersburg, Russia
E-mail: e-sagitov@mail.ru

**Abstract**: The paper is devoted to the possibility of construction of the quantum frequency standard based on two quantum magnetometers system. One of the magnetometers is based on self-oscillation spin generator, another is $M_z$-type magnetometer based on end microwave resonance. The laser pumping of $^{87}$Rb atoms placed into anti-relaxation coated cell is provided. The experimental results on the magnetometers frequency difference fluctuations measurements and Allan deviation are presented. The role of the radio-optical resonance frequency light shift different components is noted for the choosing the quantum magnetometers optimal operation mode. The effect of the light shift compensation is demonstrated.

**Keywords**: quantum frequency standard, quantum magnetometer, optical pumping, frequency stability, alkali atoms, hyperfine structure, frequency shifts.

## Introduction

Quantum frequency standards implement the synchronization of telecommunication and precise time systems. They provide correct operations of stationary and mobile systems, ensuring their reliability and accuracy. The basis for such frequency standards is the optical pumping method, which have been developed since the beginning of 1950s. The optical pumping leads to the redistribution of populations in the atom energy structure ground state, that creates the conditions to observe the magneto-dipole transitions in the hyperfine structure, providing a possibility for precise measurement of the resonance frequency, that determines the stability of standard [1]. The main measurement error source is the light frequency shift associated with the influence of non-resonant light components.

Theoretical and experimental studies have shown the ability to reduce the influence of the light frequency shift component compensation in the case of end magneto-dependent hyperfine structure transitions, which is not possible in the case of magneto-independent 0-0 transition [2]. In the case of the atomic clock on end resonance, Zeeman transitions in spin generator can be selected to compensate the magnetic fluctuations in an external magnetic field. Hereby, the compensation of the magneto-dependent end resonance magnetic dependence and the additional frequency destabilizing factors of the atomic clock are provided.

Obviously, this compensation is achieved by simultaneous registration of end resonance signal using the synchronous detection technique and self-oscillating quantum magnetometer signal. The mathematical processing of the received signals is provided.

**The system of two quantum magnetometers**

The basis of experimental research is the magnetic induction meter scheme based on the system of two quantum magnetometers with optical pumping, one of which is spin generator (low frequency magnetometer), and another is passive $M_z$-magnetometer based on microwave radio-optical resonance, resonance frequency of which corresponds to magneto-dependent transitions between hyperfine structure sublevels with extreme values of a magnetic quantum number. The simplified functional scheme of such device is presented in Fig.1.

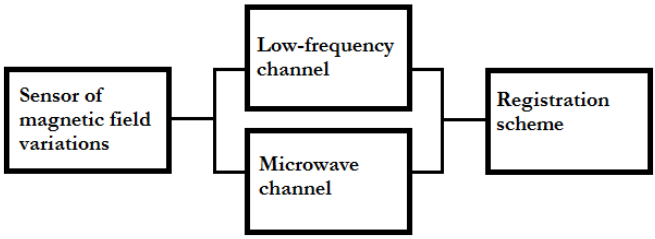


Fig.1. Functional scheme of two-channel quantum magnetometer system with optical pumping.

The functional schemes of low frequency spin generator and microwave Z-type magnetometers are presented in Fig.2 and Fig.3. The original result of this research is the using of one cell with anti-relaxation coating, containing alkali atoms for two magnetometers, which provides additional possibilities in the light shift reduction.

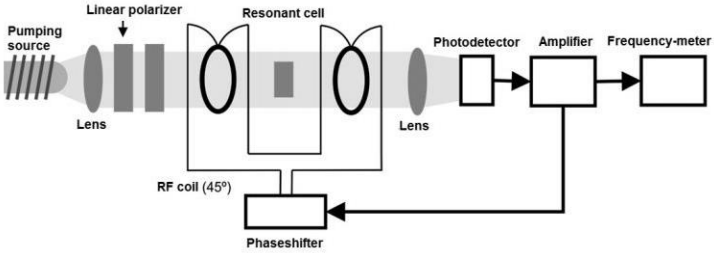


Fig.2. Spin generator, low frequency channel.

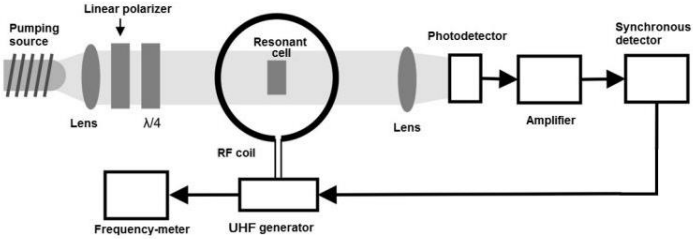


Fig.3. $M_Z$ – magnetometer, microwave channel.

The experimental verification of the light shift compensation effect was carried out within the $^{87}Rb$ atoms with laser optical pumping of ground state F=2 by light component $S_{1/2} - P_{3/2}$ of $D_2$ line in system of quantum magnetometers. The functional scheme of it contains well known elements used in gas-cell atomic clock. The scheme is operated on the microwave radio-optical resonance signals and on the weighted average resonance frequency of the Zeeman structure. It provides simultaneous measurement of magnetic field fluctuations by registration of the microwave measuring channel error signal and by measurement of the low-frequency measuring channel, which react to changes of an external magnetic field and laser pumping parameters.

Then, the signals from two channels are detected by the registration scheme where they are relatively subtracted (see Fig.4). This method provides a compensation of the magnetic fluctuations and joint light shift components compensation [2, 3]. Further, Allan variance for the differential signal of two quantum magnetometers is calculated.

Allan variance for two directions of the pumping light circular polarization ($\sigma+$ and $\sigma-$) is presented in Fig.5. The light power is about 100 μW, that corresponds to the quality factor mode of low-frequency and microwave radio optical resonance signals. The represented experiments have also been carried out under other similar conditions. Thus, there is a principal possibility of scalar and vector light shift mutual compensation by choosing a suitable sign of the pumping light circular polarization, that allows realizing the reduced resonance frequency light shift of the atomic clock based on the two quantum magnetometers system.

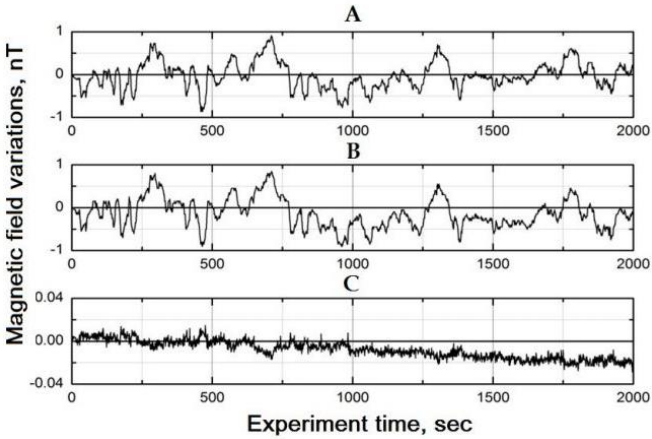


Fig.4. The magnetic variations compensation system of two quantum magnetometers. A – low-frequency channel, B – microwave channel, C — difference of the magnetic variations registered by low-frequency and microwave channels.

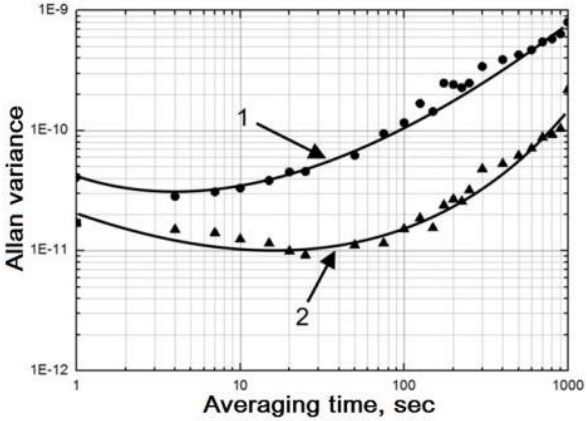


Fig.5. Allan variance for system of two quantum magnetometers. Graphs 1 and 2 correspond to the σ– and σ+ types pumping light polarization respectively.

The greatest interest in applications represents the area of averaging time $10^2$-$10^3$s. It was the cause to providing experiments for the quantum magnetometers operating mode optimization in time of averaging exceeding a time barrier of hundreds of seconds [4]. The correct choice of the laser pumping light polarization allows of the light shift various component mutual compensation of the atomic clock resonant frequency and therefore, increases its long-term stability.

## Conclusion

It was experimentally shown that the effect of the light shift components compensation allows the reducing of the atomic clock based on the system of two quantum magnetometers frequency Allan variance in comparison with the atomic clock on 0-0 transition.

### References

1. 1. F. Riehle. Frequency Standards: Basics and Applications // Weinheim: WILEY-VCH Verlag GmbH & Co. KGaA. – 2004.
2. 2. A. A. Baranov, S. V. Ermak, E. A. Sagitov, R. V. Smolin, V. V. Semenov. Double resonance frequency light shift compensation in

optically oriented laser-pumped alkali atoms // Journal of Experimental and Theoretical Physics. – 2015. – V.121, № 3. – P. 393-403.
3. 3. 4. A. A. Baranov, S. V. Ermak, E. A. Sagitov, R. V. Smolin, V. V. Semenov. Signal correlation in the tandem of a spin oscillator and microwave frequency discriminator with laser-pumped alkali atoms // Technical Physics Letters. - 2016, V.42, №4, - P.38-45.
4. 4. E. B. Aleksandrov, A. K. Vershovskii // Phys. Uspekhi. – 2009. – V.52. – P.573.

## A REVIEW ON THE DEVELOPMENT OF MICRO-NANO SATELLITE CONSTELLATION AND FORMATION FLYING TECHNOLOGIES

Sun Shu-jian, Meng Tao, Jin Zhong-he
School of Aeronautics & Astronautics, Zhejiang University,
Hangzhou, China
E-mail: mengtao@zju.edu.cn

**Abstract**: Constellation and formation flying have been becoming the most promising development trends for further micro-nano satellite applications. A review of the development of micro-nano satellite constellation and formation flying technologies is proposed in this paper. The classification, characteristics, and applications of micro-nano satellite constellation and formation flying are illustrated, and the differences between them are argued in details. This paper also provides a brief overview of the advanced technologies and the future development trends of these two kinds of distributed micro-nano satellite system. This work has guiding significance for the research of micro-nano satellite and related fields.

**Keywords**: micro-nano satellite; constellation; formation flying; networking; distributed satellite system.

### Introduction

Micro-nano satellites have taken an increasingly important part in kinds of space missions during recent years. Particularly, distributed micro-nano satellite system has been becoming the most

promising development trend for further micro-nano satellite application. The concept of distributed micro-nano satellite system [1] is as follows: by the cooperation of multiple satellites (two or more) distributed in one or more orbits as required, the system can accomplish complex space mission (such as observation, communication, scout, navigation) and realize greater application value. Compared with a single satellite, distributed satellite system may lead the micro-nano satellite to exploit its advantages of miniaturization, high integration and low cost, and offset its disadvantages of simple function, limited resources and short life.

Constellation and formation flying are the most common used distributed micro-nano satellite systems. Because of their great value of application, the micro-nano satellite constellation and formation flying technologies have developed rapidly and been intensively studied. Under the efforts of research institutes all over the world, a number of micro-nano satellite constellations have been deployed and a finite amount of micro-nano satellite formation flying experiments have been conducted. It is the goal of this paper, therefore, to explore the development status, key technologies and future trends of micro-nano satellite constellation and formation flying.

**Micro-nano satellite constellation**

A micro-nano satellite constellation [2] is a multi-satellite set for completing a specific mission by collaborative working. In general, the satellites of a constellation are distributed in different orbits so that ground coverage area and revisit frequency for a target area will be effectively improved by the cooperation of a quantity of transit satellites. The distributed satellites do not need to maintain a fixed orbit configuration so that the orbit control of each satellite is independent. Accordingly, closed-loop control and information exchange between the satellites are not required.

The following several features are usually used to evaluate the performance of a micro-nano satellite constellation [3]. 1) Coverage performance. For a constellation, the coverage area and the coverage multiplicity are the most important characteristics which decide the coverage quality of a target area. 2) Time resolution. The target area can be covered continuously or intermittently to meet the mission requirements. 3) Economy. The cost of a single satellite, the total

number of satellites, the difficulty of deployment and the over-redundancy of system determine the economy of a constellation. 4) Robustness. The functional redundancy, the back-up satellites and the ability of the defective satellites getting off the orbit are the factors to improve the service life of a constellation.

Micro-nano satellites always operate in low orbits, that will provide higher resolution to remote sensing and decrease the communication delay between the satellite and the earth. Therefore, the micro-nano satellite constellation is very suitable for communication and remote sensing. Since 1990s, countries around the world have carried out research and exploration on micro-nano satellite constellation. Most of the deployed constellations provide service for communication and remote sensing, and a few others are navigation satellite constellations or space science experiment satellite constellations. With the development of technology, micro-nano satellite constellations have been extensively used in practical applications. There are some representative examples: the Orbcomm communication satellite constellation is one of the three largest LEO Mobile constellation satellite systems in the United States. From the first launch in 1991, there have been over 70 satellites in orbit to offer service for global short data communications. The Aprize satellite constellation is another communication satellite constellation which was deployed from the year of 2002. It is estimated that there will be 24–64 satellites to provide narrowband data transmission service for mobile and fixed monitoring terminals all over the world when the constellation deployment is complete. The Flock earth observing constellation built and operated by Planet Labs consists of numerous triple CubeSats. It is the largest constellation of earth imaging satellites in the world and it offers the daily global remote sensing data at a resolution of 3–5m. Up to now, over 50 micro-nano satellite constellations in the world have been or are being deployed, becoming a major component of commercial aerospace gradually.

**Micro-nano satellite formation flying**

A micro-nano satellite formation flying [2] is a series of collaborative satellites which keep a fixed orbit configuration. Members in the satellite formation flying not only have to maintain the formation configuration, but revolve around the earth respectively.

The micro-nano satellite formation flying is equivalent a large virtual satellite, improving the system scale and the measurement baseline incredibly. Closed-loop relative control between member satellites is necessary, and all the satellites need to be coordinated to perform signal processing, communication or functional payload operation together.

The micro-nano satellite formation flying can be distinguished to the following three categories depending on the formation control requirements [4], and both the technical level and the implementation difficulty of them increase gradually. 1) Cooperative formation. The relative measurements and control will be conducted only in a certain mission period instead of long time. 2) Knowledge formation. The formation will obtain the distributed configuration by relative measurements, but the relative control is not required for a lax orbit configuration. 3) Accurate formation. This kind of formation flying requires a strict orbit configuration by means of precise autonomous control and measurements. The relative control and measurement systems result in system coupling, the accurate satellite formation is then formed.

Micro-nano satellite formation flying offers cheaper, more flexible, better performance, and more robust architectures than a single, traditional large satellite. On one hand, larger system scale and measurement baseline will greatly improve the precision of observation. On the other hand, the cooperation, the closed-loop control and the extensive information exchange bring considerable autonomy to the satellite formation flying system, reducing reliance on ground stations. It is obviously that the micro-nano satellite formation flying has enormous potential, however, its practical applications are still limited because of the great difficulty in implementation. AFRL (Air Force Research Laboratory) had ever carried out a grand plan named Techsat-21 since 1998. Several low-cost small satellites flying in formation constitute the Techsat-21 with the performance much better than a traditional large satellite, which will archieve formation flying, on-orbit autonomy, precise time measurement and time service, distributed evacuation aperture radar signal processing, etc. Unfortunately, the plan was forced to be cancelled in 2003 as a result of technical difficulties and budget overruns. 3Csat (3 Corner Sat) formation was developed by three

universities in the United States for the demonstration of nano-satellite formation flying and meteorological stereo imaging technology. It is regrettable that in 2004, one of the three satellites failed to catch the launch deadline, and the other two satellites failed to reach the scheduled orbit due to rocket technical problems. ION-F (Ionospheric Observation-Nanosatellite-Formation) was another nano-satellite formation developed by American universities. The primary scientific objective was to measure the fundamental parameters of ionosphereic density irregularities that effect radio wave propagation including communications, navigation, and the GPS (Global Positioning System). The satellites flied as a string of beads, being the first tests of a small satellite formation for making scientific observations of the near Earth space environment. The System F6 (Future, Fast, Flexible, Fractionated, Formation-Flying) project, also called Fractionated Spacecraft, is a satellite architecture where the functional capabilities of a conventional monolithic spacecraft are distributed across multiple modules which interact through wireless links. It is regarded as the technological revolution in the design and development of spacecraft, which was also vigorously promoted by DARPA (Defense Advanced Research Projects Agency). In 2013, DARPA confirmed that they cancelled the Formation-flying Satellite Demo, which meant that they closed the project. As can be seen from the above examples, although the scale and the depth of the technology study increased gradually during past 20 years, the unsolved problems lead the micro-nano satellite formation flying to stay in the stage of theoretical research and flight demonstration.

## Key technologies and future development trends

### A. High function density micro-nano satellite technology

Function density is the function offered by a unit weight of micro-nano satellite. The higher function density, the more functions and the better performance will be provided by a distributed satellite system. The high function density consists of two levels. 1) The function integration of satellite platform, subsystems, and payloads are high, and they will perform well under the premise of less resources (such as mass, volume, and power) consuming. 2) Percentage of payloads in whole satellite mass is high. The payload ratio is proposed to reach over 60%~70% instead of 30%~40% now. High function

density micro-nano satellite technology is based on standardization and modularization of spacecraft design and production technologies, having an important influence on distributed micro-nano satellite system.

**B. Satellite networking autonomous operation technology**

It is an inevitable trend that the management mode of distributed micro-nano satellite system will turn from the traditional ground station tracking, telemetry and control to the intelligent on-orbit autonomous operation. Fruitful results on single spacecraft on-orbit autonomous operation technology have been achieved during past decades, for instance autonomous spacecraft, autonomous rendezvous and docking, and autonomous attitude and orbit control, laying the foundation for satellite networking autonomous operation technology. The autonomous operation consists of six aspects [5]: 1) coordination and cooperation among satellites; 2) system resource allocation and management; 3) monitoring and handling of abnormal conditions; 4) on-orbit operation mission planning; 5) control command execution; 6) analysis and processing of mission data. The new methods and technologies of satellite networking autonomous operation are in need of being studied and implemented.

**C. Inter-satellite relative measurement and control technology**

Inter-satellite relative measurements and control technology are the core technologies for distributed satellite system, especially for the formation flying system [6]. On the one hand, the inter-satellite relative measurements include mainly range measurement, azimuth measurement, and relative position measurement. The research into inter-satellite relative measurement technology has been quite thorough, and the methods are generally divided as follows: 1) vision based relative measurement technique; 2) differential relative navigation based on GPS; 3) inter-satellite ranging system. Through certain filtering algorithms, the inter-satellite relative measurement accuracy can be as high as cm level or even μm level. On the other hand, the main tasks of inter-satellite relative control is to capture formation, reconstruct formation and maintain formation. Coupling of three dimensional orbital position and three axis attitude is usually difficult to decouple so that it is a multivariable complex system control problem. Proportional Differential (PD) control method,

discrete pulse speed control method, robust control method, and some other methods have been proposed, but the related technologies still need to be further improved.

### D. High efficiency orbit control and transfer technology

Applications of micro-nano satellite constellation and formation flying require orbit control and transfer technologies for all aspects of their operations. The application of high efficiency orbit control and transfer technology, also high efficiency micro-propulsion technology, will provide orbital-maneuvering and station-keeping capabilities at possible low cost. Orbit control and transfer technology has been playing an important role throughout the whole space mission of distributed satellite system. In the stage of entering into-orbit, to save the cost of transportation and reduce deployment difficulty, satellites should have the capability of transferring from the drift orbit to the operation orbit by themselves. In the stage of maneuvering control, satellites in the system should implement orbit maneuver according to the mission requirements. In the stage of on-orbit operation and orbit configuration maintenance, station-keeping and relative control capabilities are required. For most micro-nano satellite formation flying missions, orbit control capability is the most important factor limiting their space missions. The most common used micro-propulsion techniques are cold gas propulsion, liquefied gas propulsion, electric propulsion, chemical propulsion, MEMS propulsion, etc. However, none of the existing micro-propulsion techniques is entirely appropriate for the high efficiency orbit control and transfer requirements. A kind of micro-propulsion that can offer high specific impulse, high thrust, high speed increment becomes an imperative requirement.

## Conclusions

This paper formulates the concept discrimination between micro-nano satellite constellation and formation flying, and their technical features and characteristics are summarized. Representative examples are listed to illustrate the development status, and key technologies are analyzed to explore the future development trends. This work offers an in-depth analysis of the advanced technology of distributed micro-nano satellite system, having reference significance to researchers in related fields.

**References**

1. Lin, L. Technological development and application prospects of distributed small satellite system. Spacecraft Engineering. 2010, 19(1): 60-66. doi: 10.3969/j.issn.1673-8748.2010.01.011.
2. Lin, L. Discussion on conception of cluster, constellation and formation flying. Spacecraft Engineering.
3. Andrews J. Constellation of distributed NanoSats for real time earth observation. IAA 2011 B8-1002. 8th IAA Symposium on Small Satellites for Earth Observation. Berlin: IAA, 2011:4-8.
4. Zhu, Z. C., Yang, G. Q., Jin-Pei, Y. U., and Zhang, R. The development of micro-satellite network and formation technologies. Aerospace Shanghai. 2004, 21(6): 46-49. doi: 10.3969/j.issn.1006-1630.2004.06.011.
5. Leiner J A. Spacecraft formation flying-an overview of missions and technology challenges. AAS 07-031. San Diego: AAS, 2007.
6. Cornara S. Definition and design of satellite constellations and formation flying system. Madrid: DE-IMOS Space S. L. U, 2012.

# Section
# Signal Processing, Systems Simulation and Complex objects control for Space Applications

## AN INFLUENCE OF STRONG PULSED LASER FIELDS ON THE RESONANT PROCESSES OF QUANTUM ELECTRODYNAMICS

Dubov V.V., Roshchupkin S.P.
Department of Theoretical Physics Peter the Great St. Petersburg Polytechnic University, St. Petersburg, Russia
e-mail: serg9rsp@gmail.com, maildu@mail.ru

**Abstract:** The review on the quantum electrodynamics (QED) processes proceeding in strong pulsed light fields, realized in modern powerful pulsed lasers is presented. Resonant processes of quantum electrodynamics in strong laser fields are considered. Following QED processes in the pulsed laser field are considered: resonant scattering of ultrarelativistic electrons, resonance of exchange amplitude of a photon by an electron. The resonant peak altitude and width are defined by the external pulsed wave properties. It is demonstrated that the resonant cross sections may be several orders of magnitude greater than the corresponding cross sections in the absence of an external field.

### Introduction

Use of a powerful coherent light source in modern applied and fundamental research has stimulated study of the external strong field influence on quantum electrodynamics (QED) processes [1–2]. A characteristic feature of electrodynamics processes of second order in the fine-structure constant in laser fields is associated with the fact that such processes may occur under both coherent and resonant conditions [1–9]. The resonant character relates to the fact that lower-

order processes, such as spontaneous emission and one-photon creation and annihilation of electron-positron pairs, may be allowed in the field of a light wave. Therefore, within a certain range of energy and momentum, a particle in an intermediate state may fall within the mass shell. Then the considered higher-order process is effectively reduced to two sequential lower-order processes [1–9]. The appearance of resonances in a laser field is one of the fundamental problems of QED in strong fields.

As a result of laser technology development, different types of coherent light sources have become available, with intensities that have increased up to $10^{24}\,\mathrm{W/cm^2}$ in recent years. The new experimental conditions have required constant improvements in calculations and model development. The amplitude of the field intensity of powerful ultra-short pulsed lasers changes greatly in space and time. In the description of QED processes in the presence of a pulsed laser the external field is usually modeled as a plane non-monochromatic wave, when a characteristic pulse width $\tau$ obeys the condition [1–9]

$$\omega\tau >> 1. \tag{1}$$

There are two characteristic parameters in these processes of QED in the field of a pulsed electromagnetic wave. The first one is the classical relativistic-invariant parameter [1–9],

$$\eta_0 = \frac{eF_0\lambda\!\!\!^{-}}{mc^2}, \tag{2}$$

which in the pulse peak equals numerically to the ratio of work done by the field within the distance equal to a wavelength to the electron rest energy ($e$ and $m$ are the charge and the mass of an electron, $F_0$ and $\lambda\!\!\!^{-} = c/\omega$ are the strength and the wave-length of an electric field in the pulse peak respectively). The Bunkin-Fedorov quantum parameter is specified [1–9]:

$$\gamma_i = \eta_0 \frac{mv_i c}{\hbar\omega}. \tag{3}$$

($v_i$ is the electron speed). We treat these problems of QED within the range of moderate-strong-field intensities, when

$$\eta_0 << 1, \quad \gamma_i \gtrsim 1. \tag{4}$$

Consequently, the quantum Bunkin-Fedorov parameter is the main parameter which determines multiphoton processes. Hereafter, we use the relativistic system of units $\hbar = c = 1$.

**Resonant scattering of ultrarelativistic electrons in the strong field of a pulsed laser wave**

Here we describe the resonant scattering of ultrarelativistic electrons at small ingoing–outgoing angles in a strong pulsed laser field. It is well known that it is precisely the case of small-angle scattering that makes the largest contribution to the cross section for the ultrarelativistic energy of particles. (see Fig.1) [6].

We study the scattering of an electron with the four-momentum $p_{1i,1f} = \left(E_{1i,1f}, \mathbf{p}_{1i,1f}\right)$ by an electron with the four-momentum $p_{2i,2f} = \left(E_{2i,2f}, \mathbf{p}_{2i,2f}\right)$ in the case of ultrarelativistic energy and small angles in a field of a pulsed laser wave. In the center-of-mass frame we have

$$1 \ll E_i / m \ll m / \omega, \quad E_i \approx \left|\mathbf{p}_i\right|, \tag{5}$$

$$\theta_{i,f} = \angle\left(\mathbf{e}_z, \mathbf{p}_{i,f}\right) \ll 1. \ \delta_{i,f} = \theta_{i,f}\left(E_{i,f} / m\right) \tag{6}$$

Here $m$ is the electron mass; $\theta_{i,f}$ are the incoming and outgoing polar angles of electrons; $\delta_{i,f}$ are the characteristic parameters appearing in the scattering of ultrarelativistic articles.

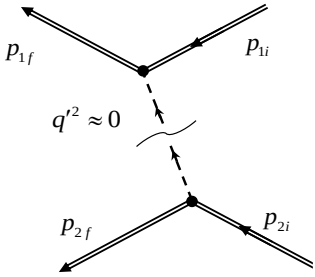


Fig. 1. The direct Feynman diagram of resonant scattering of an electron by an electron in the field of a pulsed laser wave.

The external pulsed field is taken into account accurately. We consider the field of a pulsed laser wave as a plane non-monochromatic wave, propagating along the $z$-axis with a polarization plane $xy$. The four-potential of such a field has the form

$$A(\varphi) = g\left(\frac{\varphi}{\omega\tau}\right)\frac{F_0}{\omega}\left(e_x \cos\varphi + \delta_{\text{ell}} e_y \sin\varphi\right), \tag{7}$$

$$\varphi = kx = \omega(t - z). \tag{8}$$

Here, $\varphi$ is the wave phase; $\tau$ is the characteristic duration of a laser pulse; $F_0$ is the strength amplitude of the electric field in the pulse peak; $\omega$ is the characteristic frequency of the laser wave; $k = (\omega, \mathbf{k})$ is the wave vector; $\delta_{\text{ell}}$ is the wave ellipticity parameter ($\delta_{\text{ell}} = 0$ corresponds to the linear polarization, $\delta_{\text{ell}} = \pm 1$ corresponds to the circular polarization); $e_x = (0, \mathbf{e}_x)$, $e_y = (0, \mathbf{e}_y)$ are the four- vectors of wave polarization. The function $g(\varphi/\omega\tau)$ in (7) is the envelope function of the four- potential of an external wave that allows to take into account the pulsed character of a laser field.

The process is studied in the frame of the quasimonochromatic approximation when a laser wave performs a lot of amplitude oscillation, i.e. the following condition is met:

$$\omega\tau \gg 1. \tag{9}$$

The condition (9) is satisfied for the majority of modern lasers [1–2]. The given paper is devoted to studying of the strong field case, when

$$\eta_0 >> 1, \quad \eta_0 m / E_i \gtrsim 1 \tag{10}$$

The suitable laser fields depend on the energy of ultrarelativistic electrons $\left(\gtrsim 10^{19}\, W/\text{cm}^2\right)$. The fields with such intensity are accessible for modern laser facilities functioning in the pulsed regime [1]. The condition of Oleinik resonance assumes the form [2–8]:

$$q'^2 \lesssim \frac{(kq')}{\omega\tau} \ll \omega^2. \tag{11}$$

The resonant scattering angle for the fields with great intensity and small incoming angles in the ultrarelativistic case can be expressed as:

$$\theta_{\text{res}} = \left(l + 2|r|\right)\frac{\omega m}{E_i^2}\delta_i . \tag{12}$$

The resonant cross section of laser-assisted Möller scattering into the element of the solid angle is obtained in the form:

$$\frac{d\sigma_{\text{res}}}{d\Omega_f} = \frac{r_e^2 m^2}{E_i^2 \theta_{\text{res}}^4}\left(\frac{\eta_0 m}{E_i}\right)^4 \frac{(\omega\tau)^2}{8}\left(1+\delta_{\text{ell}}^2\right)^2 \sqrt{\frac{\pi}{2}}\cdot P_{\text{res}} , \tag{13}$$

$$\begin{aligned} P_{\text{res}} &= \frac{1}{2\rho}\int_{-\rho}^{\rho} d\phi_1 \exp\left(-\phi_1^2\right)\left(1-\text{erf}\left(\sqrt{2}\phi_1\right)\right) \\ &\times \int_{-\rho}^{\phi_1} d\phi_1' \exp\left(-\phi_1'^2\right)\cos\left(2\beta\left(\phi_1-\phi_1'\right)\right). \end{aligned} \tag{14}$$

Here $\beta$ is the resonant parameter, which determines the nature of electron-electron scattering in the field of a pulsed light wave:

$$\beta = \frac{q'^2}{4(kq')}\omega\tau \approx \frac{\omega\tau}{2}\left(\frac{\theta}{\theta_{\text{res}}}-1\right). \tag{15}$$

We are interested in estimation of the ratio of the resonant cross section of ultrarelativistic electrons in the field of a strong pulsed laser wave to the corresponding cross section in an external field absence. This ratio has the form

$$\frac{d\sigma_{\text{res}}}{d\sigma_{Moller}} = \left(\frac{\eta_0 m}{E_i}\right)^4 (\omega\tau)^2\left(1+\delta_{\text{ell}}^2\right)^2 \frac{\pi^2}{72\rho} \tag{16}$$

For further study we consider the case of the frontal collision in scattering of ultrarelativistic electrons with equal energy. Consequently, the c. m. system coincides with the laboratory reference system. The laser wave at that, according to the problem statement, propagates under the small angle to the collision axis. We also consider the external wave circular polarization. Let us carry out analysis of the cross section of resonant scattering for several laser systems (see, the Table I). We note that laser systems PHELIX and Vulcan concern to the class of petawatt optical lasers generating within the sub-picoseconds range of duration [1]. Laser systems Vulcan and ELI because of their parameters will concern to multipetawatt lasers generating within the femtosecond range. The

basic characteristics of the laser systems are provided in the Table I. Figure 2 represents the ratio of the resonant scattering of electrons in the strong laser field to the cross section of electron scattering in an external field absence as a function of the initial energy in the units of the electron rest energy for concrete laser systems (see, Table I). One can conclude from (16) and Figure 2 that the dependence of the cross sections ratio on the electron initial energy is linear for logarithmic scales. Thus, for both electron MeV-energy and petawatt optical lasers the ratio of the resonant cross section of electron-electron scattering in the field of a strong pulsed laser and the cross section in an external field absence amounts to 5-6 orders of the magnitude. In the same case for multipetawatt lasers within the femtosecond range the ratio (16) may reach 8-9 orders of the magnitude. The resonant cross section becomes of the same order with the Moller cross section for the electron energy of the order 102 MeV for the 1PW range of laser field intensity, and for the electron energy up to 1 GeV in the case of the multupetawatt range.

Table 1. The basic characteristics of the modern laser systems.

| Laser system | Pulse duration, ($\omega\tau$) | Peak intensity, ($\eta_0$) |
|---|---|---|
| PHELIX | 500 fs (900) | $2\cdot10^{20}$ W/cm$^2$ (9) |
| Vulcan | 500 fs (900) | $10^{21}$ W/cm$^2$ (20) |
| Vulcan 10 | 30 fs (60) | $10^{23}$ W/cm$^2$ (170) |
| ELT | 15 fs (35) | $10^{24}$ W/cm$^2$ (500) |

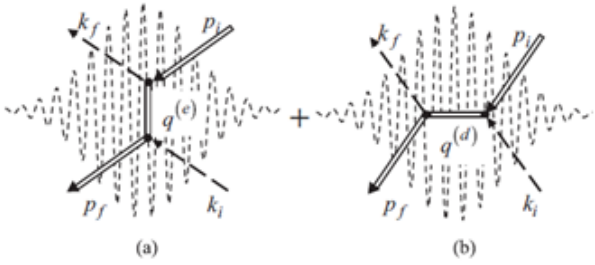


Fig. 2. The ratio of the resonant cross section of scattering of an electron by an electron in the strong pulsed laser field to the cross section of electron-electron scattering in an external field absence as a function of the initial energy for concrete laser systems (Table I).

The obtained results can be verified experimentally on the said facilities with using of highly monochromatic beams of electrons and detectors with high angular resolution.

**Resonance of exchange amplitude of a photon by an electron scattering in the pulsed laser**

Here we study of laser-modified Compton scattering (see [7], Fig.3). We consider the external field as a circularly polarized pulsed electromagnetic wave, propagating along the *z*-axis with a polarization plane *xy*. The four potential of such a field has the form (7) and (9).

We search for the resonance probability of the exchange diagram using the resonance approximation $\left(q^{(e)}\right)^2 \approx m^2$. The ratio of the differential resonance probability of the scattering of the photon by electron via exchange diagram and to the differential probability of the Compton effect in the absence of the external field in the same scattering kinematics is

$$R^{(\mp)} = \frac{\mathrm{dW}_{\mathrm{res}}^{(\mp)}}{d\mathrm{w}_{\mathrm{Compt}}} = \frac{16}{\left(u_1^{(\mp)}\right)^2} \frac{K^{(\mp)}}{f\left(\tilde{u}', \tilde{u}_1\right)} \cdot \eta^4 \varphi_0^2 \frac{\tau_{\mathrm{imp}}}{T} P_{\mathrm{res}}\left(\beta_i^{(\mp)}\right), \qquad (17)$$

$$P_{\mathrm{res}}\left(\beta_{\mp}\right) = \frac{1}{2\pi} \int_{-\infty}^{\infty} \left|I_1(\beta_{\mp}, l_*)\right|^2 d\left(\varphi_0 l_*\right), \qquad (18)$$

Analysis of laser-modified Compton scattering through the exchange diagram has demonstrated the following. The resonant probability of the Compton scattering in the field of the weak intensity wave may exceed the corresponding probability in the external field absence in several orders of the magnitude. Thus, for the electron energy $E_i = 5\mathrm{MeV}$, the photon frequency $\omega_i = 11.7\ \mathrm{eV}$, the intensity in the pulse peak $I = 7 \times 10^{16}\ \mathrm{Wcm}^{-2}$, and arbitrary angles of the entrance of both electron and photon, the ratio $R^{(-)}$ amounts to seven orders of the magnitude. The excess of the resonant probability of the Compton effect for the case of ultrarelativistic energy of the electron moving in the narrow cone with the direction of the external wave propagating, may amount to ten orders of the magnitude.

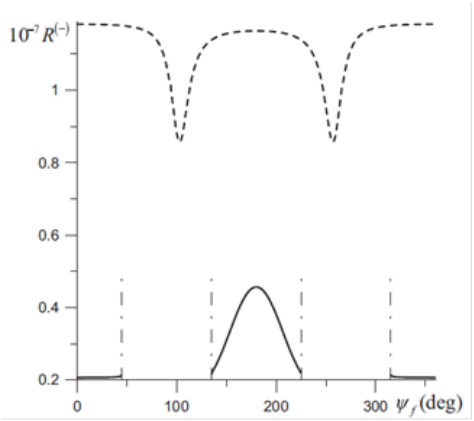


Fig. 3. Feynman diagram for the Compton effect in the field of the pulsed light wave for the direct (a) and exchange (b) parts. Incoming and outgoing double lines correspond to the Volkov function of an electron in initial and final states, and the dashed lines represents the wave function of a photon; inner lines designate the Green's function of an electron in the pulsed field.

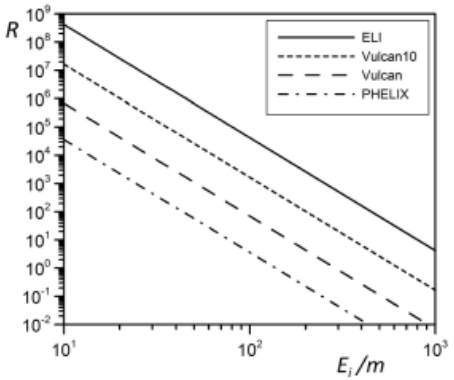


Fig. 4. The ratio (17) of the resonant probability of scattering of the photon by an electron in the field of the pulsed wave ( $I = 7\times10^{16}$ Wcm$^{-2}$, $\tau/T$ = 1, $\omega$ = 2.35 eV) in the resonant peak $\beta\pm$ = 0 to the probability of the Compton scattering, when the external field influence is absent, as a function of the photon output azimuthal angle $\psi_f$ . The dashed line corresponds to the photon entrance angle $\theta_i = 130^\circ$ and the solid line corresponds to the case $\theta_i = 164^\circ$, $E_i = 5\text{MeV}$, $\omega_i = 11.7$ eV.

## Conclusions

In review the resonant QED processes in strong pulsed laser field are considered. Significant influence of a pulsed field on the processes was shown.

The obtained results may be experimentally verified, for example, by the scientific facilities at the SLAC National Accelerator Laboratory and FAIR (Facility for Antiproton and Ion Research, Darmstadt, Germany).

## References


1. A. Di. Piazza, C. Muller, K. Z. Hatsagortsyan, and C. H.
2. Keitel, Rev. Mod. Phys. **84**, 1177 (2012).
3. S. P. Roshchupkin and A. A. Lebed. *Effects of quantum electrodynamics in the strong pulsed laser fields*, Kiev, Ukraine: Naukova Dumka, 2013.
4. S. P. Roshchupkin and A. I. Voroshilo. *Resonant and Coherent Effects of Quantum Electrodynamics in the Presence of Light Field.* Kiev, Naukova Dumka, 2008 [in Russian].
5. S.P. Roshchupkin, A.A. Lebed, E.A. Padusenko, and A.I. Voroshilo, ”Quantum electrodynamics resonances in a pulsed laser field”, Laser Phys., vol. 22, pp. 1113-1144, 2012.
6. S. P. Roshchupkin, A. A. Lebed, and E. A. Padusenko, ”Nonresonant quantum electrodynamics processes in a pulsed laser field”, Laser Phys., vol. 22, pp. 1513-1546, 2012.
7. A.A. Lebed’, E.A. Padusenko and S.P. Roshchupkin. Resonant scattering of ultrarelativistic electrons in the strong field of a pulsed laser wave. Laser Phys., vol. 26**,** 025302 (9pp), 2016.
8. V.N. Nedoreshta, S.P. Roshchupkin, and A.I. Voroshilo. Resonance of the exchange amplitude of a photon by an electron scattering in a pulsed laser field. Physical Review A **91**, 062110, 2015.
9. V. N. Nedoreshta, A. I. Voroshilo, S. P. Roshchupkin and V. V. Dubov. Two-photon emission of an electron in the weak pulsed laser field for the resonant case. Laser Physics **27** (2017) 026003.
10. A. A. Lebed’, E. A. Padusenko, S. P. Roshchupkin and V. V. Dubov. Parametric interference effect in nonresonant pair photoproduction on a nucleus in the field of two pulsed light waves. Physical Review A **95**, 043406 (2017).

# I/Q IMBALANCE CALIBRATION USING A GENETIC ALGORITHM APPROACH

HUANG Jia-jun, ZHANG Chao-jie, JIN Zhong-he, XU Jiu-Ling
Micro-Satellite Research Center, Zhejiang University,
Hangzhou/China
E-mail: zhangcj@zju.edu.cn

**Abstract**: Zero-IF architecture is one of the most integrated transmitter architecture, but I/Q imbalance can affect the transmitting performance and produce an unwanted mirror signal. To solve this problem, this paper proposes a calibration method of I/Q imbalance based on genetic algorithm (GA), which combines the additional loop-back path in the transmitter radio frequency (RF) end. In the digital baseband, the compensation parameters can be rapidly searched by using the global search capability of GA and the feedback information from loop-back path. The transmitting signal will be pre-compensated by using the obtained compensation parameters, so that I/Q imbalance can be calibrated.

**Keywords**: genetic algorithm; I/Q imbalance; I/Q imbalance calibration; transponder; transmitter.

## Introduction

Micro-satellites are a new concept of satellites based on micro-electromechanical technology. They work in satellite networks through decentralized constellations. They work together to complete a wide range of mapping, stereoscopic imaging, distributed space measurements and many other tasks. In the future of scientific research and commercial applications, micro-satellites will play an important role.

In the view of the problem of I/Q imbalance, the existing studies can be divided into training sequence based method and blind estimation method. There are some papers based on ML criteria for joint estimation and compensation of transceiver I/Q imbalance [1]. Some papers also refer to a scheme that allows joint estimation and compensation of I/Q imbalance at the channel, transmitter and receiver [2]. The scheme has better performance only when the system

has only I/Q imbalance, but once the system introduces interference such as frequency offset and the phase noise, the performance will drop rapidly. And the complexity of this scheme is relatively high. There are also some methods , which do not require the training sequences [3].

Aiming at the problem of the unbalanced transmitter I/Q branches, combined with the loop-back path of the transmitter RF end, this paper proposes a calibration method of I/Q imbalance based on GA. This method is suitable for I/Q imbalance calibration of the integrated transceiver chip with the loop-back path of the transmitter RF end.

## The relationship between Sideband Suppression and I/Q Imbalance

Assume that the I-channel signal is a cosine signal and the amplitude is *A*. Assume also that the Q-channel signal is a sine signal and the amplitude is *B*. The phase difference between I-channel signal and Q-channel signal is *p(w)*. By derivation of the formula, it can be concluded that the difference between main signal and the mirror signal under the condition of I/Q imbalance, that is, the sideband suppression (SBS) is:

$$SBS = 10 \cdot \lg[\frac{A^2 - 2AB\cos(p(w)) + B^2}{4A^2}] \tag{19}$$

In order to simplify the description, it is assumed that *p(w)* is independent of the frequency, that is, the phase imbalance at each frequency component is the same, assuming *p'*. Then, SBS is:

$$SBS = 10 \cdot \lg\{\frac{1}{4}[(\frac{B}{A})^2 - 2\frac{B}{A}\cos(p') + 1]\} \tag{20}$$

As it can be seen from the formula (2), SBS can be used to measure the degree of I/Q imbalance.

When I/Q imbalance is calibrated, the value of SBS will be infinite.

## Calibration Scheme

### A. The Architecture of Transmitter Calibration Scheme

The baseband signal frequency is set to $f_b$. The local oscillator (LO) frequency of the transmitter is set to $f_{TXLO}$. The LO frequency of

the receiver is set to $f_{RXLO}$. Note that, $f_{TXLO}$ should be slightly larger than $f_{RXLO}$ and $f_{TXLO}$ should be much larger than $f_b$.

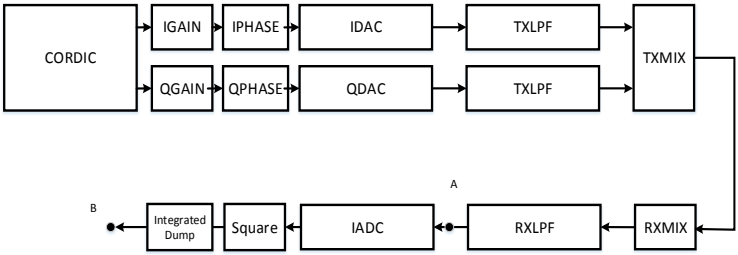


Fig.1. I/Q Imbalance Calibration Block Diagram.

As shown in Fig.1, the RF signal transmitted from the transmitter passes through the loop-back path and then is subjected to the low-pass filtering. At this point, the signal frequency at point A is $f_{TXLO}$ - $f_{RXLO}$ - $f_b$. Then, the signal at point A is sampled by the ADC module, and then through the square processing module and integrated dump processing module. Finally, the signal at point B can be used to indicate the degree of I/Q imbalance.

Therefore, the calibration of I/Q imbalance can be transformed into the following optimization problem:

$$\begin{aligned} \min \quad & f(I\_Gain, Q\_Gain, Phase) \\ & I\_Gain > 0 \\ s.t \quad & Q\_Gain > 0 \\ & \pi > Phase > -\pi \end{aligned} \tag{21}$$

where *I_Gain* and *Q_Gain* are the gain compensation parameter of I-channel and Q-channel, *Phase* is the phase compensation parameter, and function *f* is the signal strength at the point B.

In the ideal case, the above optimization problem has the unique minimum point. Using the algorithm, such as gradient descent method [4], the optimal solution of the optimization problem can be found. But in practice, there are multiple minimum points for the optimization problem due to noise and interference. At this point, the gradient descent method is no longer applicable because it is difficult to find the global minimum point. In this case, heuristic search

algorithms, such as GA, can be used to find the optimal solution for the optimization problem.

### B. Genetic Algorithm

GA is a random search algorithm that draws on the natural selection of natural circles and the natural genetic mechanism [5]. GAs are used to simulate reproduction, crossover and mutation in natural selection and natural inheritance. In each iteration, a set of candidate solutions is preserved and the better individuals are selected from the solution group by a certain metric. These individuals are combined using genetic operators (selection, crossover and mutation) to produce a new generation of candidate solution group. Repeat this process until a certain convergence criterion is met. Compared with the traditional heuristic optimization algorithm, the main characteristic of GA is the group search strategy and the simple genetic operator. The group search strategy enables then GA to break through the restriction of the search filed, so as to realize the distributed information collection and search on the whole solution space.

## Scheme Simulation

### A. Simulation Condition

This simulation uses MathWorks' Simulink software for simulation. The GA program used is from the Matlab Genetic Algorithm Toolbox, where the population size is set to 100 and the number of evolution is set to 64. In order to verify the effect of GA in this scheme better, a general gradient descent program is written as a comparison, where the search step is 0.0005, the termination precision is 0.000001 and the maximum number of searches is 15000.

### B. Simulation results

The actual simulation results are shown in Fig.2. In the simulation, additive white Gaussian noise (AWGN) is added to the channel. Under the condition of high signal-to-noise ratio (SNR), the GA result is not much different from the optimization result using general gradient descent method. Under the condition of low SNR, the optimization result using GA is better than the optimization result using general gradient descent method. Because of the low SNR conditions, there are multiple poles in the optimization problem, which leads to the solution of the general gradient descent method

easy falling into the local minimum point. Because GA has excellent global search ability, even if it falls into the local minimum point, it will quickly escape, so it can find the global optimal solution.

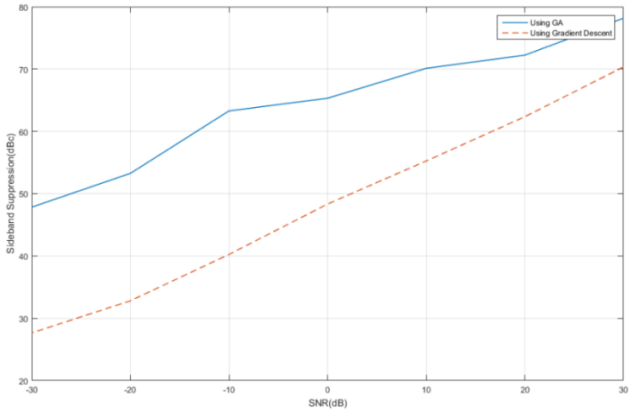


Fig.2. Sideband Suppression Using Different Method for Calibration.

## Conclusion

By utilizing the loop-back path of the transmitter RF end, combined with the excellent global search ability of GA, the proposed method can effectively complete the calibration of I/Q imbalance of the transmitter. Compared with the traditional method, the proposed method is easier to implement.

## References

1. Lerkvaranyu S, Miyanaga Y. Maximum likelihood detection of I/Q imbalance signal with self-organized clustering assistance[C] // International Symposium on Intelligent Signal Processing and Communication Systems. IEEE, 2004:660-664.
2. Chung Y H, Phoong S M. Joint estimation of I/Q imbalance, CFO and channel response for MIMO OFDM systems[J] // IEEE Transactions on Communications, 2010, 58(5):2573-2576. doi: 10.1109/TCOMM.2010.05.080627
3. Tsai Y, Yen C P, Wang X. Blind frequency-dependent I/Q imbalance compensation for direct-conversion receivers[J] // IEEE Transactions on

Wireless Communications, 2010, 9(6):1976-1986. doi: 10.1109/TWC.2010.06.090651
4. Fletcher R, Powell M J D. A Rapidly Convergent Descent Method for Minimization[J] // Computer Journal, 1963, 6(6):163-168.
5. Weile D S, Michielssen E. Genetic algorithm optimization applied to electromagnetics: a review[J] // IEEE Transactions on Antennas & Propagation, 1997, 45(3):343-353.
6. Harik G R, Lobo F G, Goldberg D E. The compact genetic algorithm[J] // IEEE Transactions on Evolutionary Computation, 2002, 3(4):287-297

## A NEW NONDESTRUCTIVE METHOD FOR DETERMINING THE COMPOSITION OF COMPONENTS IN BIOLOGICAL OBJECTS IN EXPRESS MODE

Myazin N.S.[1], Rukin E.V.[1], Davydov V.V.[1, 2, 3], Yushkova V.V.[4]
[1]Peter the Great St. Petersburg Polytechnic University, St. Petersburg, Russia
[2]The Bonch-Bruevich St. Petersburg State University of Telecommunications, St. Petersburg, Russia
[3]All-Russian Research Institute of Phytopathology, Moscow Region, Russia
[4]St. Petersburg University of Management Technologies and Economics, St. Petersburg, Russia
E-mail: myazin.n@list.ru

**Abstract.** A new method for determining the components composition and their concentration in express mode in biological objects and liquid suspensions is proposed. It allows us to measure not only the relaxation constants $T_1$ and $T_2$, using which it is possible to determine the deviation degree of the medium from the standard state, but also the concentrations of the components included in the medium composition, at the site of sampling by a compact NMR spectrometer.

**Keywords:** Nuclear magnetic resonance, NMR, monitoring in the express mode, spectroscopy

**Introduction**

Currently one of the urgent problems before conducting experiments with various biological solutions and liquid media is defining their suitability in the express mode [1–6], characterized by the longitudinal and transversal relaxation times [6–10]. In addition, such control is, of course, should not cause any irreversible changes in the environment [1, 2, 4–7, 10–13]. This is especially important for the space station, where samples for various tests are delivered by cargo vessels passing through the various layers of the atmosphere, at high overloads, as well as different emergency situations arising while loading or unloading the vehicle may occur in the conditions of outer space. The samples for the study can be corrupted while you move them around the station or accidental violation of the storage conditions. Since in the space environment, long-term experiments are mostly carried out and hence using samples with deviations from the standard state, can lead to losses of time, and the failure of the planned scientific program of flight (stay time of the crew on the space station is limited and some experiments must be serial).

One of the possible solutions to this problem is the small-sized nuclear magnetic spectrometer (relaxometer) considered in [1, 5, 6]. We can determine the degree of deviation from the standard state in the express mode using measured values of the relaxation constants $T_1$ and $T_2$. Recently before conducting various studies, especially when working with biological solutions and suspensions, as well as acids and salts, it has increasingly become necessary to determine in express mode not only the medium state but also the components concentration of which it is made (e.g., HCl, NaF, NaOH or $FeCl_3$), acidity (pH), etc. Experiments have shown that this is especially important if the medium is used after prolonged storage, transportation, container changes, etc.

In previously developed NMR spectrometer (relaxometer), registration of the NMR signal was possible only at the resonant frequency $f_p$ of protons contained in the researched medium. It did not allow solving new tasks of express control.

**Compact NMR spectrometer and measurement methods**

To solve the considered new problems, we developed a new small-size design of the magnetic system of the spectrometer and a scheme for registering the NMR signal (fig. 1)

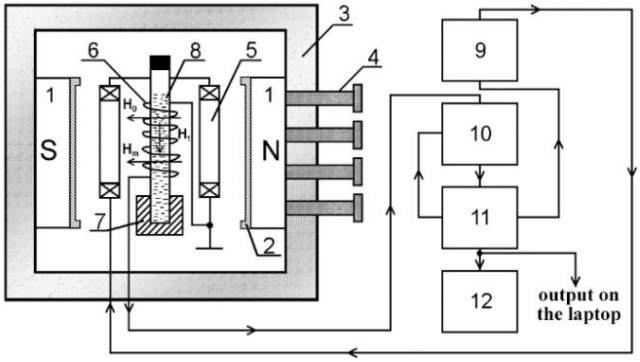


Fig. 1 Structural scheme of compact NMR spectrometer: 1 — permanent magnet; 2 — inserts; 3 — neutral for the placement and alignment of the magnets; 4 — adjusting screws; 5 — modulation coil; 6 — NMR signal registration coil; 7 — locking device for the container with the researched medium; 8 — container with the researched medium; 9 — RF generator; 10 — registration scheme; 11 — processing and control unit; 12 — oscilloscope.

In the new design of compact NMR spectrometer, S/N of the detected NMR signal is increased by 13 times by reducing the degree of inhomogeneity of the magnetic field more than tenfold and increasing the induction $B_0$ by several times in the registration coil placement area 6. This made it possible to register the NMR signal at the resonance frequencies of the other elements nuclei, for example, sodium or chlorine. For mediums consisting only of elements containing nuclei with magnetic moments (for example, HCl, NaF, or $ZnCl_2$) we have created a method that allows determining concentration of elements in a medium using amplitudes of the registered NMR signals from different nuclei.

However, the most significant result obtained on newly developed design is NMR signal registration with amount of "wiggles" (oscillating peaks) not less than six. This allows us to carry out many measurements with higher precision and to develop a new

method for determining components concentrations of a mixture, which is formed by substances that not enter into a chemical reaction (e.g., fats, multicomponent medical suspensions, oils, gasoline, etc.). NMR signal from such mixtures technique is the total signal from each of the components due to specific of its registration with use of modulation.

Our experiments showed that the shape of the line $G(t)$ of the registered NMR signal from the substance in a weak magnetic field when tuning the autodyne detector circuit to the maximum of the S/N ratio is described by the following relation:

$$G(t) = \sqrt{Av^2(t) + BU^2(t)}, \tag{1}$$

where $v(t), U(t)$ — the absorption and dispersion signals resp., $A$, $B$ — coefficients determining the contributions of the absorption and dispersion signals to the NMR signal.

The obtained solution (1), which is in good agreement with the experimental results, made it possible to develop a technique for simulating the detected NMR signal from the mixture, by dividing the received signal into signals from its constituent components. Following expression can represent the shape of the registered NMR signal $G_m(t)$ from the mixture:

$$\begin{aligned} G_m(t) &= \sqrt{A_m v_m^2(t) + B_m U_m^2(t)} \\ &= \sum_{i=1}^{k} V_i \cdot N_i \sqrt{A_i v_i^2(t) + B_i U_i^2(t)} \\ &\sum_{i=1}^{k} V_i = V_r \end{aligned} \tag{2}$$

where $v(t), U(t)$ — the absorption and dispersion signals resp., $A$, $B$ — coefficients determining the contribution to the NMR signal of the absorption and dispersion signals (m — mixture, i — mixture components).

In our case the only thing that influences on $v(t)$ and $U(t)$ is the relaxation constants. For the mixture itself, $T_1$ and $T_2$ can be determined using NMR signal detected from it. In addition, we know relaxation constants for one of the mixture components, because

initially this mixture should be this component in its pure form. The relaxation constants of the remaining components of the mixture, as well as the volumes in which they are contained in the researched medium, are chosen so that

(2) is satisfied, the temperature of the researched mixture is known. When eq.

(2) is fulfilled, we can determine mixture components through relaxation constants, as well as their relative concentrations through their volumes.

**Results and discussion**

Fig. 2 shows the sodium NMR signals from sodium hydroxide NaOH registered by the NMR spectrometer of new design.

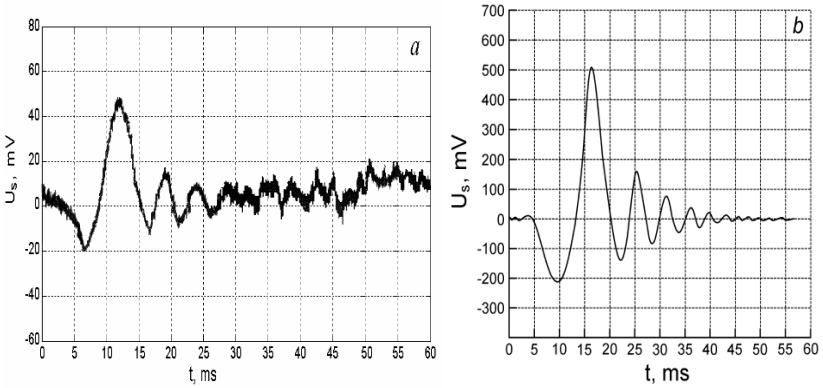


Fig. 2 The registered NMR signal from sodium hydroxide at T = 291.3 K: a) without accumulation; b) output of accumulation scheme.

The analysis of NMR signals presented in fig. 2 shows that when they are registered at the resonance frequency of sodium nuclei $\omega_{Na}$, signal-to-noise ratio is more than 1.3. This makes it possible to perform the AFC on the resonance of sodium nuclei. However, it is impossible to carry out measurements of $T_1$ and $T_2$ with an error no more than 1.0% (which is necessary for unambiguously determining the medium state [1–4, 6, 8]) without usage of an accumulation scheme since the SNR is less than 3.0 (fig. 2, a). In addition, there are

noises at peaks of the NMR signal. The subsequent accumulation of the NMR signal makes it possible to obtain SNR > 10.0 (fig. 2, b), which ensures measurement of $T_1$ and $T_2$ with the required accuracy. Moreover, the relative concentrations of protons and sodium in sodium hydroxide can be determined using ratio of their amplitudes $U_s$ in registered NMR signal.

Fig. 3 gives an example of the possibility of determining the components and their concentrations in a mixture of two gasolines AI-95 and A-76 using our method.

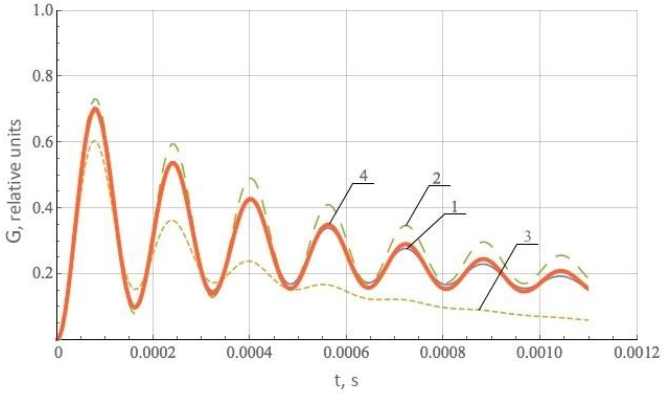


Fig. 3 NMR signal line forms. Graph 1 corresponds to the experimental signal from a mixture of gasoline AI-95 and A-76 (75 to 25 %). The NMR signal simulation: from pure gasoline AI-95 (2) and A-76 (3), mixture of gasoline AI-95 and A-76 75:25% (4).

Comparison of the results of NMR signals simulation from gasoline AI-95 and A-76, as well as their mixture, with experimental data shows the reliability of proposed method. The calculated concentrations of gasolines AI-95 and A-76 in the studied medium are in agreement with the concentrations which we have used to prepare this mixture within the measurement error.

## Conclusions

The obtained results show that the usage of proposed method while carrying out studies with a new design of a small-size NMR spectrometer allows obtaining information on the composition of the medium at the site of sampling, and making conclusions about its

further use without additional measurements in a stationary laboratory. Earlier in [1, 5, 6], the measurements of $T_1$ and $T_2$ provided information only on the presence of deviation from the medium standard state that required its additional study in a stationary laboratory to make a reliable decision on the further use of this medium.

In addition, in the new design of the spectrometer, the NMR signal registration from various magnetic nuclei expands its functional capabilities greatly both in the number of possible studied mediums and in the information obtained about the state of the medium.

## References


1. Karseev A Yu, Cheremiskina A V, Davydov V V, Velichko E N 2014 J. of Physics: Conference Series **541** 012006
2. Arkhipov V V 2012 Instruments and Experimental Techniques **55** 692
3. Kashaev R S, Gazizov E G 2010 Journal of Applied Spectroscopy 77 321
4. Mussil V V, Pilipenko V V, Lemeshevskaya E T, Keremzhanov K D 2011 Instruments and Experimental Techniques **54** 397
5. Karseev A Yu, Vologdin V A, Davydov V V 2015 J. of Physics: Conference Series **643** 012108
6. Davydov V V, Velichko E N, Dudkin V I, Karseev A Yu 2015 Instruments and Experimental Techniques **58** 234
7. Alexandrov A S, Archipov R V, Ivanov A A, Gnezdilov O I, Gafurov M R, Skirda V D 2014 Applied Magnetic Resonance **45** 1275
8. Zaporozhets O V, Shkurdoda V F, Peregudov O N, Zaporozhets V K 2010 Instruments and Experimental Techniques **53** 718
9. Ryzhov V A, Pleshakov I V, Nechitailov A A, Glebova N V, E.N. Pyatyshev E N 2014, Applied Magnetic Resonance **45** 339
10. Panchenko P A, Fedorov Y V, Perevalov V P, Jonusauskas G P, Fedorova O A 2010 Journal Phys. Chem. A. **114** 4118
11. Nikolaeva M V, Puzyk M V 2014 Optics and Spectroscopy **116** 589
12. Erdogru Y M, Manimaran D K, Gulluolu M T, Amalanathan M K, Hubert J I, Yurdakul N S 2013 Optics and Spectroscopy **114** 525
13. Davydov V V, Dudkin V I, Karseev A Yu 2014 Measurement Techniques **57** 912

# OPTIMAL BALANCED SINR TRACKING FOR MULTI-CHANNEL CDMA BASED RANGING SYSTEM

Xu Jiuling, Zhang Chaojie, Wang Chunhui, Huangjiajun
Micro-Satellite Research Center, Zhejiang University, Hangzhou, China
E-mail: zhangcj@zju.edu.cn.

**Abstract**: Code Division Multi-Access (CDMA) is suitable technique for one to multi-point ranging, but it suffers from the Near-Far effect (NFE) i.e. the signal of a farther one will be masked by the nearest one. Unlike the territorial CDMA system aiming at achieving the acceptable lowest Signal to Interference plus Noise ratio (SINR) for a large number of users, the space CDMA ranging system requires higher SINR for a better ranging performance. Consequently, the method of dynamically tracking the Optimal Balanced SINR based on fuzzy logic control is proposed for satellite cluster relative position recognizing.

**Keywords**: CDMA, multi-channel ranging, Optimal Balanced SINR Tracking, fuzzy logic control.

## Introduction

Future space missions are envisioned to become more complex and diversed, such as gravity mapping, tracking of forest fires, finding water resources, etc. [1], this demand may be beyond the capability of a traditional monolithic satellite. Consequently, the distributed satellite system is proposed to overcome this drawback [2]. The most successful applications of distributed satellite system are GRACE [3] and TanDem-X [4], which is based on two satellites only. Nowadays, clusters consisting of more than two micro-satellites are becoming attractive due to their fast development and low costs. The knowledge of relative distance among satellites is one of the most important observations for relative position recognizing and collision avoidance [5]. Consequently, the point to point ranging system is no longer suitable for this requirement. Code Division Multi-Access is qualified for one to multi-point ranging, and it can also support data communication. However, CDMA system will suffer from the Near-

Far effect (NFE) when the signal of a farther one is masked by the nearest one. The territorial CDMA system uses Power Control (PC) [6] to mitigate NFE, and the goal of territorial PC is to reach the acceptable lowest SINR for the largest number of user access. However, the space CDMA system is totally different, firstly, the number of access points is limited and fixed, secondly, the accuracy of ranging depends on Signal to Interference plus Noise ratio (SINR), so higher SINR is required for the optimal ranging performance. Additionally, the scale of inter-satellite distance varies from several hundred meters to hundreds kilometers, the SINR is changing from time to time. Therefore, the Optimal Balanced SINR Tracking (OBST) is proposed to solve this problem. We use a cluster of four satellites to verify the OBST method, the simulation result shows that the optimal SINR can be always tracked.

**System model**

Let us define a basic cluster with four satellites, the one connected directly to other satellites is designated as the master (denoted as A), and the other three serve as the slaves (denoted as B,C,D) as shown in Fig. 3.

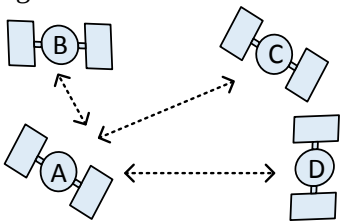


Fig. 3 Basic cluster with four satellites.

The ranging system is based on CDMA, so all the connections can be held simultaneously with little interference by code division. In order to acquire optimal performance, the receiving SINR of each slave should be balanced and be as large as possible. The optimization can be achieved by synchronous maximizing of the receiving power of each slave according to the Power Limiting Condition (PLC) of the smallest receiving power. Therefore, the block diagram of Optimal

Balanced SINR Tracking is like that proposed in

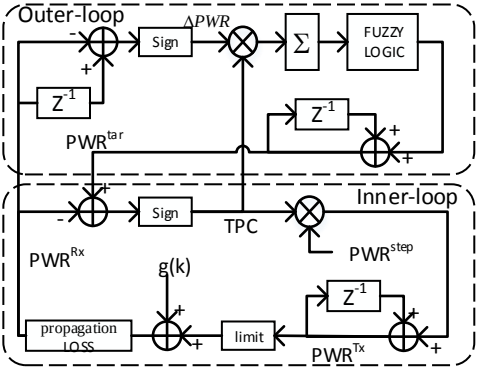


(a) Block diagram for OBST

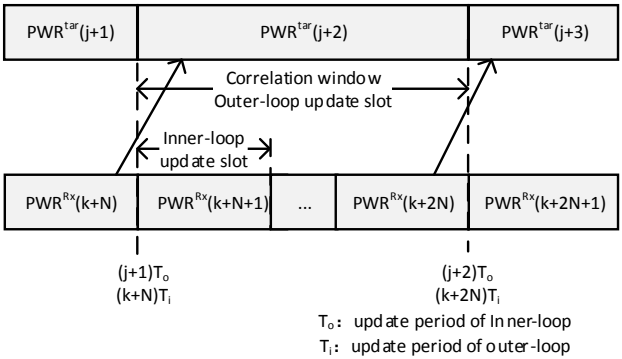


(b) Inner/outer-loop updating diagram

Fig. 4(a).

In OBST, the target power ( $PWR^{tar}$ ) can be tunable referring to the relative distance between the satellites. For the inner-loop control, the slave adjusts its transmission power ( $PWR^{Tx}$ ) referring to the Transmit Power Command (TPC) provided by master,

$$PWR^{Tx}(k) = PWR^{Tx}(k-1) + TPC(k-1) \cdot PWR^{step} \quad , \qquad (22)$$

where $PWR^{step}$ is the adjusting step, $k \in \mathbb{Z}$, representing the *k*-th inner-loop update slot. In order to save the transmission data bandwidth, the TPC is a one bit sign generated by comparing the receiving power ( $PWR^{Rx}$ ) to the $PWR^{tar}$ ,

$$TPC(k) = \mathrm{sgn}[PWR^{tar}(j) - PWR^{Rx}(k)] \ , \tag{23}$$

where $j \in \mathbb{Z}$, representing the $j$-th outer-loop update slot whose period is usually integer multiplies of inner-loop update period, as shown in

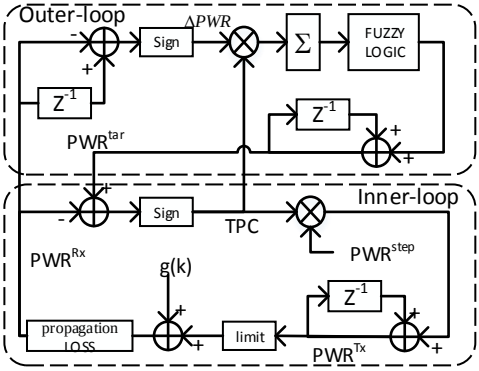


(a) Block diagram for OBST

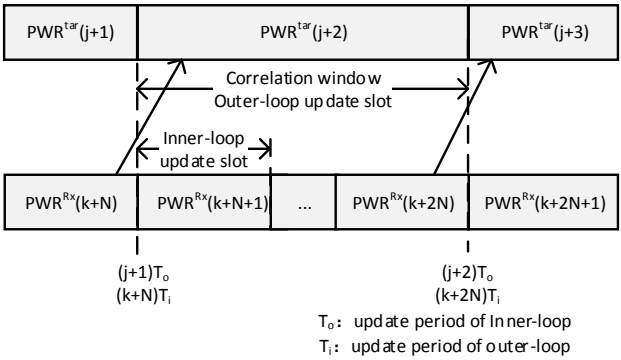


(b) Inner/outer-loop updating diagram

Fig. 4(b). $g(k)$ is the sum of white noise and receiving power estimate jitter, $L(k)$ is the propagation loss. So the power estimation at receiver can be expressed as

$$PWR^{Rx}(k) = PWR^{Tx}(k) + L(k) + g(k) \tag{24}$$

For the outer-loop control, the master calculates the correlation between TPC and the sign of $\Delta PWR^{Rx}$, where

$\Delta PWR^{Rx}(k) = PWR^{Rx}(k) - PWR^{Rx}(k-1)$. The correlation ($R_N$) implies the relationship between $PWR^{tar}$ and the minimum PLC which is usually decided by the farthest slave due to the largest propagation loss. Assuming that the PLC were not reached, $R_N \approx 1$, since $\text{sgn}[\Delta PWR(k)] = TPC(k-1)$, otherwise, $R_N \approx 0$ due to inner-loop control is invalid. Consequently, $R_N$ can be used as a flag to indicate whether the PLC is reached or not. But unfortunately, $R_N$ only tells us the $PWR^{tar}$ can be set higher or lower, there is no strict expression to describe their relationship, so we use a fuzzy logic controller to achieve the maximum power tracking.

$$R_N(j) = \frac{1}{N}\sum_{k=jN-N+1}^{jN} \text{sgn}[\Delta PWR(k)] \cdot TPC(k-1) \qquad (25)$$

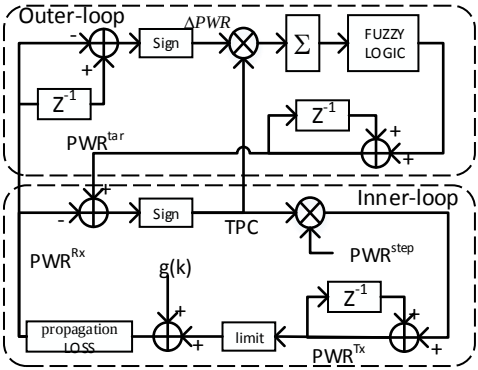


(a) Block diagram for OBST

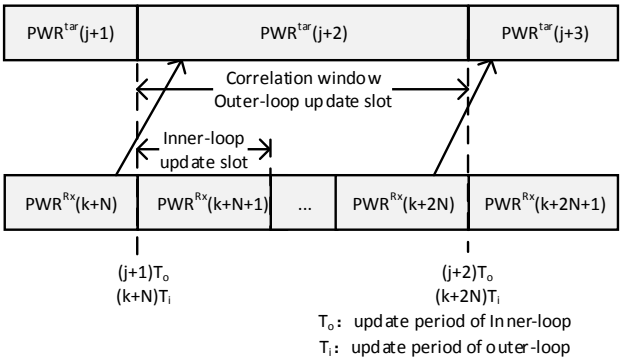


(b) Inner/outer-loop updating diagram

Fig. 4 Block diagram for OBST & inner/outer-loop updating diagram.

Theoretically, the sign of $\Delta PWR^{Rx}(k)$ will be the same as TPC(k-1) since transmit power is decided by TPC, as shown in Eq. (22). However, the false judgment of $\Delta PWR^{Rx}$ may occur when the error of power estimation is too large or $PWR^{step}$ is too short. We assume that power estimation obeys normal distribution $X \sim N(\mu_k, \sigma^2)$, where $\mu_k$ represents the real receiving power, and $\sigma^2$ is the variance. Therefore, $\Delta PWR^{Rx}$ obeys normal distribution $Y \sim N(\mu_k - \mu_{k-1}, 4\sigma^2)$, and the probability of false judgment is:

$$\begin{aligned} P_{err} &= P(Y<0 \mid \mu_k - \mu_{k-1} > 0) + P(Y>0 \mid \mu_k - \mu_{k-1} < 0) \\ &= \Phi\left(\frac{-\Delta\mu}{2\sigma}\right) = 1 - \Phi\left(\frac{\Delta\mu}{2\sigma}\right) \end{aligned} \quad , \quad (26)$$

where $\Delta\mu = \mu_k - \mu_{k-1} = PWR^{step}$, $\Phi$ is the Cumulative Distribution Function of standard normal distribution. If the transmitter power did not reach its up-limit and with the consideration of false judgment probability, $R_N$ can be expressed as:

$$R_N = \frac{(1-P_{err})N - P_{err} \cdot N}{N} = (1-2P_{err}) \quad (27)$$

If current $PWR^{tar}$ were larger than the PLC, $\Delta PWR^{Rx}$ would obey normal distribution $Y_1 \sim N(0, 4\sigma^2)$ since $\mu_k = \mu_{k-1}$, which leads

the probability of false judgment to be $P_{err1} = \Phi(0) = 0.5$. So that, the correlation would be

$$\overline{R}_N = \frac{(1 - P_{err1})N - P_{err1} \cdot N}{N} = 0 \tag{28}$$

In fact, $\overline{R}_N$ usually is around zero due to the limited length of correlation window. The gap between $\overline{R}_N$ and $R_N$ is large enough to set a threshold to decide $PWR^{tar}$ to be increased or decreased.

**Fuzzy logic controller**

In this paper, a Fuzzy Logic Controller (FLC) is employed for tracking the largest receiving power. The structure is shown in Fig. 5. There are three parts, i.e., fuzzification, knowledge base and inference engine.

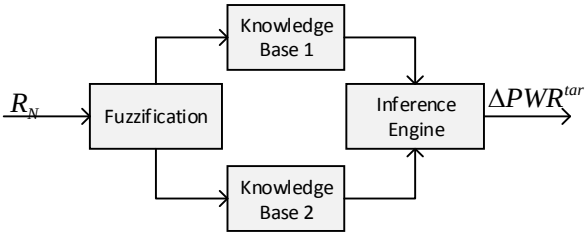


Fig. 5 Structure of fuzzy logic control.

1. *Fuzzification*: This component converts the input value into fuzzy value. In order to speed up the maximum power convergence process, we define the unchanged times of fuzzied $R_N$ (denoted as $Q_N$) as a second input. The bounds of $R_N$, $Q_N$ are [0,1], [1,5] respectively. The corresponding fuzzy sets are Large (L), Medium (M), and Small (S).

2. *Knowledge Base*: This step defines the linguistic control rules for an FLC by IF-THEN statement. The design of target-power tracking should achieve the goal of fast rise time and small steady-state error in outer-loop. Therefore, the bound of target power step ($\Delta PWR^{tar}$) is [-1 dB,1 dB], and the corresponding fuzzy sets are Large Positive (LP), Small Positive (SP), Zero (ZE), Small Negative (SN),

and Large Negative (LN). The membership functions are shown in fig. 6.

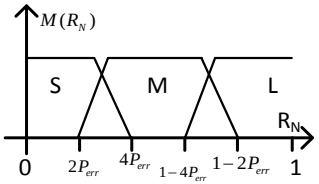


(a) $R_N$

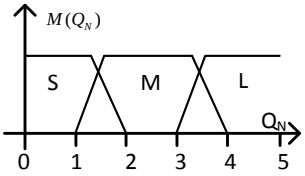


(b) $Q_N$

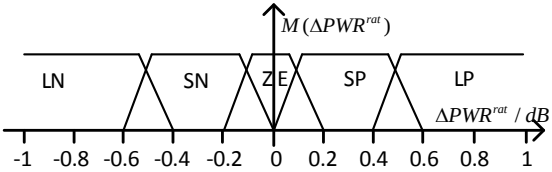


(c) target power step

Fig. 6 Membership function for FCL.

3. *Inference Engine*: This is the decision-making part of FLC, it infers fuzzy control action by employing fuzzy implication and fuzzy control rules. According to Fig. 3, the target power step is given by FLC and the target power can be updated as

$$PWR^{tar}(j+1) = PWR^{tar}(j) + \Delta PWR^{tar}(j) \tag{29}$$

for

$$\Delta PWR^{tar}(j) = FLC\{R_N(j), Q_N(j)\} \tag{30}$$

where $FLC\{\bullet\}$ is the fuzzy inference function, which can be decided by simulation and the knowledge of experts. According to aforementioned rules, $FLC\{\bullet\}$ has been summarized in Table 1, so that, the controller can be easily realized by look-up table.

Table 1 Fuzzy control rules of the FLC

| $R_N \setminus Q_N$ | L | M | S |
|---|---|---|---|
| L | LP | LP | SP |
| M | SN | SN | ZE |
| S | LN | LN | SM |

**Simulation results**

Although the optimal SINR tracking could be achieved by OBST, the initialization of the system is totally different since all the slaves have to connect to master before enabling OBST. Consequently, the $PWR^{tar}$ is set to be a low value until all the connections have been established. After that, the $PWR^{Rx}$ of all slaves is rising synchronously to a certain level which equals to the minimum PLC of these slaves. Consequently, the receiving power will be tracking up to the minimum PLC, as shown in Fig. 7. The dotted lines represent the PLC of slaves, and all the $PWR^{Rx}$ coincide together since inner-loop control when initialization is made.

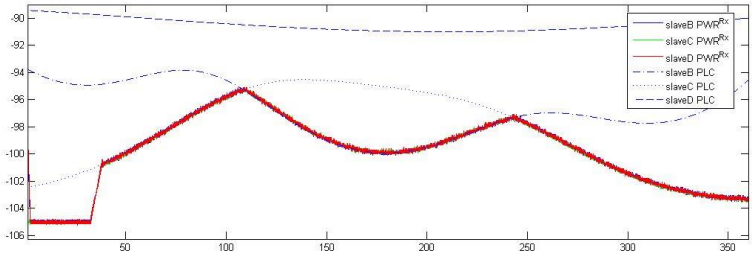


Fig. 7 Simulation result.

**Introduction**

In this work, a novel OBST system is proposed to optimize the receiving SINR, it is meaningful for CDMA ranging system since the performance can be enhanced. The correlation between TPC and $\Delta PWR^{Rx}$ is built to detect whether the current $PWR^{tar}$ has been reached power limiting condition, after which a fuzzy logic controller is employed to complete the minimum PLC tracking. The effectiveness of OBST is validated by a cluster of four satellites.

## References

1. Radhika, Radhakrishnan, William W. Edmonson, Fatemeh Afghah, Ramon Martinez Rodriguez-Osorio, et al. Survey of Inter-Satellite Communication for Small Satellite Systems. IEEE COMMUNICATIONS SURVEYS & TUTORIALS, 2016, 18(4): 2442-2473.
2. Marco D'Errico, et al. Distributed Space Missions for Earth System Monitoring. Microcosm Press and Springer, California, 2013.
3. Bertiger W, Bar-Sever Y, Desai S, Dunn C, Haines B, Kruizinga G, Kuang D, Nandi S, Romans L, Watkins M, Wu S, Bettadpur S. GRACE: millimeters and microns in orbit. Proceedings of ION-GPS-2002, Portland, Oregon, USA, 2002: 2022–2029.
4. G. Krieger, "TanDEM-X: A satellite formation for high-resolution SAR interferometer," IEEE Transactions on Geosciences and Remote Sensing, 2007, 45(11): 3317-3341
5. Casey Lambert and Alfred Ng, Intersatellite Separation Mechanism for the JC2Sat Formation-Flying Mission. Journal of Spacecraft & Rockets, 2011, 48 (4) :654-663.
6. F Lin, X Huang, Y Wu. An uplink power control scheme in CDMA mobile communication system. IEEE Vehicular Technology Conference, 1998, 3(3): 2479-2482.


# SIMULATION OF QPSK LARGE FREQUENCY OFFSET CARRIER RECOVERY BASED ON FFT


ZHANG Gu-hong, ZHAO Chang-chang, YU Zhuo-qun,
JIN Zhong-he
Zhejiang university micro-satellite research center, Hangzhou, China
ghzhang@zju.edu.cn



**Abstract:** In aerospace telemetry, there is usually a large Doppler frequency offset, and the receiver QPSK demodulator cannot perform carrier recovery. So the large frequency offset compensation is needed. In this paper, a large frequency offset extraction method using fast Fourier transform and phase lock loop is proposed. Based on the QPSK modulation signal, a complex signal containing frequency offset information is constructed, and then the value and the sign of frequency offset is calculated by fast Fourier transform.

At last, the phase error will be eliminated by PLL. The utility model has the advantages of high estimation accuracy, large capture range and short lock time. The good performance of this method for large frequency offset carrier recovery is manifested in the simulation. It can be applied to signal synchronous demodulation in satellite communication.

**Keywords:** quadrature phase shift keying (QPSK); large frequency offset; carrier recovery; fast Fourier transform (FFT); simulation

## Introduction

QPSK modulation is easy to implement and has good anti-jamming performance and spectrum utilization, so it is widely used in digital satellite communication systems. Coherent signal demodulation technology is usually used to demodulate QPSK signal. This technology has strict requirements for synchronization of the carrier signal, so carrier recovery is a key part for coherent demodulation. In the spaceflight communication system, the Doppler large frequency offset caused by the relative motion between the ground receiver and the spacecraft has a great influence on the carrier recovery, which can cause the failure of receiver demodulation. The traditional large frequency offset capture technologies are: the frequency lock loop (FLL), the frequency scanning and so on. The FLL technology is proposed in reference [1]. Carrier frequency will be traced directly by FLL, and its discriminator outputs the carrier frequency error and has good dynamic performance. But frequency lock loop has poorer performance than PLL in precision. A method of combining FLL and PLL is proposed in the paper [2].Taking into account the frequency discrimination range and tracking accuracy, this method will make the carrier tracking loop order and parameters increase resulting in difficulties in design and adjustment. The frequency scanning method is proposed in the work [3], the method is simple, and it can be used in high and low signal to noise ratio of the occasion. But it needs pre-established scan range and step size. In this paper, a large frequency offset carrier recovery method based on FFT is proposed, it uses FFT algorithm to calculate the absolute value and symbol of the carrier frequency offset accurately. Then the carrier

frequency offset will be compensated, combined with the PLL to improve phase accuracy. Fewer parameters, larger capture range, and less lock time are the advantages of this method.

**Carrier recovery design and principles**

The design block diagram of QPSK large frequency offset carrier recovery based on FFT is shown in Fig. 1. First of all, QPSK signal will multiply with local carrier generating two signals by passing low-pass filter. The lock detector is used to detect whether the carrier frequency offset is within the bandwidth of the PLL filter or not, and if not, the carrier frequency offset can be identified as a large frequency offset. The FFT processing module will be switched on by lock detector. A complex signal containing frequency offset information is constructed with two signals mentioned above by the FFT processing module. FFT operator will be done to get the spectrum after collecting in a certain number of points, the spectrum is single sideband spectrum related to sign of carrier frequency offset. The value and sign of carrier frequency offset can be calculated by searching for the peak which corresponds to the frequency in the spectrum. Finally, the frequency offset will be compensated to the numerically controlled oscillator (NCO), the offset between the NCO center frequency and input carrier frequency will be within PLL bandwidth. After the large frequency offset compensation, FFT processing module will be switched off. The phase offset will be eliminated by PLL. When the discriminator output error tends to be zero, QPSK carrier frequency offset recovery is achieved. Each module principles are illustrated below.

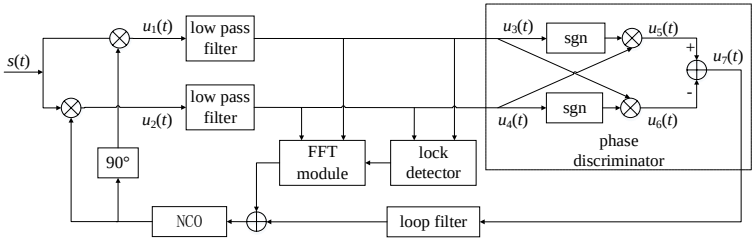


Fig.1. Realization diagram for QPSK large frequency offset carrier recovery.

### A. COSTAS cross loop

The basic principle for carrier recovery is to use a modified Costas loop -- COSTAS cross loop, suppose the QPSK signal $s(t)$ received is :

$$s(t) = I(t)\cos(\omega_c t + \varphi_0) + Q(t)\sin(\omega_c t + \varphi_0) \tag{1}$$

In the above equation, $I(t)$ and $Q(t)$ are divided in accordance with the even and odd order, they can be +1 or -1; $\omega_c$ is the carrier frequency; $\varphi_0$ is the modulation carrier initial phase.

$sin(\omega_c t + \varphi_1)$ is the local carrier, $\varphi_1$ is the local carrier initial phase. The low-pass filters output are:

$$u_3(t) = \frac{1}{2} I(t)\sin(\Delta\varphi) + \frac{1}{2} Q(t)\cos(\Delta\varphi) \tag{2}$$

$$u_4(t) = \frac{1}{2} I(t)\cos(\Delta\varphi) - \frac{1}{2} Q(t)\sin(\Delta\varphi) \tag{3}$$

In the above equations, $\Delta\varphi = \varphi_1 - \varphi_0$ is the phase offset between the local coherent carrier and the received carrier.

Phase detector output is as follows:

$$u_7(t) = \mathrm{sgn}[u_3(t)] \cdot u_4(t) - \mathrm{sgn}[u_4(t)] \cdot u_3(t) \tag{4}$$

Through calculation, discriminator output can be obtained as below:

$$u_7(t) = \begin{cases} -\sin\Delta\varphi & \Delta\varphi \text{ in the 8th and 1st regions} \\ \cos\Delta\varphi & \Delta\varphi \text{ in the 2nd and 3rd regions} \\ \sin\Delta\varphi & \Delta\varphi \text{ in the 4th and 5th regions} \\ -\cos\Delta\varphi & \Delta\varphi \text{ in the 6th and 7th regions} \end{cases} \tag{5}$$

COSTAS cross loop phase curve is similar to a saw tooth wave, and the subarea of $\Delta\varphi$ and the phase curve are given in the paper [4]. In addition, the ideal second-order ring performance is far superior to

other second-order ring loops, so ideal second-order ring is adopted as loop filter in this paper.

**B. Lock detector**

FFT processing module will be calculated only once and will get an accurate value of carrier frequency offset, so a lock detector that can detect the carrier frequency offset is needed. When the carrier frequency offset is within the PLL filter bandwidth, the FFT processing module will be switched off. The FFT processing module will be switched on by the lock detector only when the carrier frequency is too large. This will reduce the resource overheated and improve the performance of the carrier recovery system when the carrier frequency is too small. The block diagram of the lock detector is shown in Fig. 2.

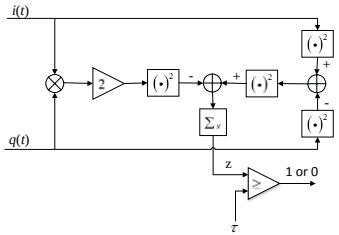


Fig.2 Structure diagram for lock detector.

The two signals input to the lock detector which are mixed and filtered by low-pass filter are:

$$i(t) = \frac{1}{2} I(t)\cos(\Delta\omega t + \Delta\varphi) - \frac{1}{2} Q(t)\sin(\Delta\omega t + \Delta\varphi) \tag{6}$$

$$q(t) = \frac{1}{2} I(t)\sin(\Delta\omega t + \Delta\varphi) + \frac{1}{2} Q(t)\cos(\Delta\omega t + \Delta\varphi) \tag{7}$$

In the above equations, $\Delta\omega$ is the frequency offset between the local coherent carrier and the received signal, and $\Delta\varphi$ is the phase offset between the local coherent carrier and the received signal.

The lock detector performs the following operations to remove the influences of $I(t)$ and $Q(t)$ so that the output is only related to the frequency offset and phase:

$$\left[2i(t)q(t)\right]^2 - [i^2(t) - q^2(t)]^2 = \frac{1}{4}\cos[4(\Delta\omega t + \Delta\varphi)] \tag{8}$$

When the loop is in the unlocked state, and the value of $\Delta\omega$ is not zero and the mathematical expectation of the above formula will be zero. In contrast, when the loop is locked, the mathematical expectations are not zero. So when the carrier frequency offset is large, lock detector will output 1, and the FFT processing module will be switched on. After the carrier is recovered, lock detector will output 0 and the FFT processing module will be switched off.

**C. FFT frequency offset estimation algorithm**

As a common tool for digital signal processing, FFT has been widely used in the field of spectrum analysis with its fast operation and low signal to noise ratio threshold.

On the basis of equations (10) and (11), sinusoidal signals including frequency offset and phase offset are obtained by the following operation:

$$2q(t)i(t)\cdot[q^2(t)-i^2(t)]=\frac{1}{4}\sin[4(\Delta\omega t+\Delta\varphi)] \tag{9}$$

Equation (11) and (12) are combined to be a complex signal $x$(t):

$$x(t)=\frac{1}{4}\cos[4(\Delta\omega t+\Delta\varphi)]+\frac{j}{4}\sin[4(\Delta\omega t+\Delta\varphi)] \tag{10}$$

Amplitude-frequency characteristic $X(\omega)$ of $x(t)$ can be obtained by FFT:

$$X(\omega)=\frac{\pi}{4}\delta(\omega-4\Delta\omega) \tag{11}$$

where $\delta(t)$ is the impulse function and its expression is:

$$\delta(t)=\begin{cases}1 & t=0\\ 0 & t\neq 0\end{cases} \tag{12}$$

The estimated value $\Delta\omega$ of the corresponding carrier frequency offset is obtained by searching the peak value in the amplitude-frequency characteristic, and this is added as the carrier recovery compensation to the frequency control of the NCO. In practical applications, the above operations are performed in discrete domain. It is supposed that the signal $x(t)$ corresponds to the discrete domain signal $x(n)$, and the amplitude-frequency characteristic $X(\omega)$ corresponds to $X(k)$. The amplitude-frequency characteristic $X(k)$ of

$x(n)$ can be obtained by N points FFT operation. When $X(k)$ reaches the maximum value, the frequency value which the value of $k$ corresponds to is the carrier frequency offset estimated absolute value, and because the discrete Fourier transform of the complex signal is a unilateral spectrum, so when the k value is between 0 and $N/2$, the sign of carrier frequency offset is positive, and when the k value is between $N/2$ and $N$, the sign of carrier frequency offset is negative.

**Simulation and validation by Simulink**

The carrier recovery loop simulation model built in Simulink is shown in Fig. 3. In the model, the QPSK modulation signal with symbol rate of 1Mbps, carrier frequency of 10MHz and sampling rate of 40MHz is generated by QPSK Modulator. AWGN Channel is the additive white Gaussian noise channel, and can control the signal to noise ratio of input. An integral shaking filter is introduced as the Low.., and reduces the occupation of resources. According to the Doppler frequency offset range given in citation [5], the maximum carrier frequency offset absolute value in this design is set to 200 kHz. In addition, in order to ensure a certain frequency offset estimation accuracy and reduce the FFT calculation, the value of FFT calculation point is set to 1024, and the FFT resolution is about 391 Hz.The residual frequency error will drop into the bandwidth of loop filter after compensation. FFT Processor, Lock Detector, Loop Filter module are FFT processing module, lock detector, loop filter, the model of the internal structures can refer to their principle. The loop filter bandwidth is set to be 1 kHz.

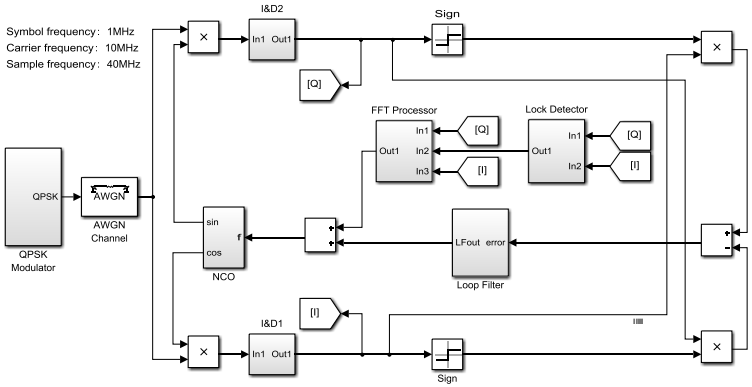


Fig.3 Simulation model for QPSK carrier recovery in Simulink.

In the simulation process, the frequency offset between local carrier and received carrier is set to 10 kHz, and the effectiveness of the FFT algorithm is simulated. In order to get better simulation results, the simulation time is set to 0.15 s when the carrier algorithm does not use FFT recovery. As the FFT algorithm is used, the simulation time is set to 0.015 s. The final simulation result of the carrier recovery model is shown in Fig. 4.

From the error output curve of the phase detector in Fig. 4, the error convergence process can be clearly seen. The design of the carrier recovery is verified by the simulation. At the same time, a comparison between using and not using the FFT algorithm is made by the simulation results. The lock time of the PLL is reduced by FFT algorithm from about 0.1 s to 0.01 s, and the effectiveness of the FFT algorithm is proved.

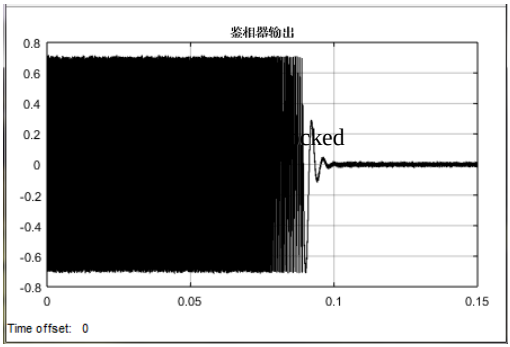


(a) Discriminator output when no using the FFT algorithm, simulation time is 0.15 s

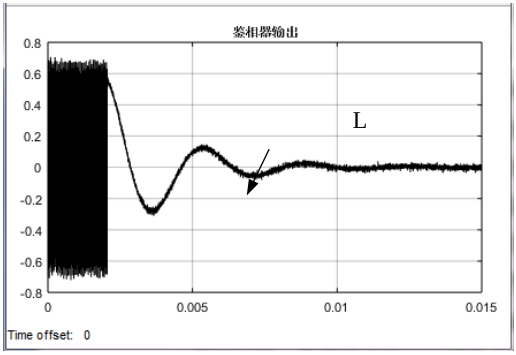


(b) Discriminator output when using FFT algorithms, simulation time is 0.015 s

Fig.4 Simulation results for carrier recovery model.

## Conclusions

In this paper, a QPSK large frequency offset carrier recovery method based on FFT is introduced. This method is designed on the basis of COSTAS cross-ring; the lock detector and FFT spectrum estimation algorithm are added to improve the carrier acquisition speed and range. By simulation, the feasibility of this method is proved, and it can meet the requirement of QPSK large frequency offset carrier recovery. Compared with other large frequency offset carrier recovery methods, the advantages of this method are that the design idea is simple and the loop lock time can be greatly reduced. So it can be applied to the satellite communication signal receiving system.

**References:**

1. Kaplan E D. Understanding GPS: principles and application [M]. Boston: Artech House, 2006.
2. WANG Jun, SUI Xin. Carrier tracking loop with improved frequency discrimination and its performance analysis [J]. Systems engineering and electronic technology, 2012, 34(12): 2438-2443.
3. E H Satorius, Z Ye, T Ely. Carrier Acquisition and Tracking Requirements for Doppler Navigation[C].Aerospace Conference, 2003, 4:4_1631-4_1638.
4. WANG Wei, CHEN Hui. Principle and Simulation of carrier recovery in high speed data transmission [J]. Radio Engineering, 2005, 35(5): 43-44.
5. XIE Yan-hua. Estimation and compensation of Doppler frequency shift based on satellite mobile communication system [D]. Dalian: Dalian University, 2013: 21-22.

## A STRUCTURE OF EXPERIMENT ON PROCESSING SIGNALS RECEIVED FROM SHIP NAVIGATION EQUIPMENT BY MEANS OF "S-AIS" PAYLOAD

Malygin D.V., PopovE.N., Nguyentan H.P.
Peter the Great St. Petersburg Polytechnic University, St. Petersburg, Russia
office@spbstu.ru

**Abstract.** The study focuses on the idea of experiment on processing signals received from ship navigation equipment by means of "S-AIS" payload.

**Keywords:** small spacecraft, nanosatellite, picosatellite, platform, cubesat, onboard communication system, ais

The term "nanosatellite" is applied to ultra-small spacecraft (USSC) with a mass less than 10 kg and the volume of basic unit smaller than 1 $m^3$. Construction of USSC has become clearly possible according to electronic components, which enables us to create spacecraft with mentioned sizes. During the last 15 years, hundreds of spacecraft have been launched, and a large number of them have been successfully exploited. The main problem of USSC construction refers

to the question how to achieve the rational relation between quality, cost and efficiency indexes. These characteristics are accomplished only by considering the major physical and technical performance factors. The most significant advantage of USSC lies in the fact that it can be designed and constructed by a small group of researchers.

Development in micro-electronics has facilitated rapid progress in USSC area, which became a flexible instrument for conducting scientific, technological and educational experiments in space. On the other hand, these spacecraft have not yet made their way from student projects to full-fledged players on space service market: until now, there is a perception that this area is purely entertaining activities (PR for space technology), or these products might be used as testing stands for developing and/or demonstrating various technology solutions (ideas, conceptions, etc.). There are several reasons behind this. Firstly, because of the very conception of USSC: small production cycle, lack of support by classical standards of aerospace industry, inexperience of researcher team and modest financing. Secondly, the reliability indicators are low because initially non-specialized electronic components of the class "industrial" are used. Finally, the space field has generally been too conservative. In order to overcome these mentioned barriers, it is reasonable to carry out a series of experiments based on USSC for addressing principal scientific and technological problems.

The aim of this study is to conduct scientific and technical experiments in space by means of nanosatellite developed in the laboratory "Space communication technologies" of Peter the Great St. Petersburg Polytechnic University.

The automatic identification system (AIS) is an automatic system designed to identify ships, their sizes, GPS position, course, speed and other ships' information, which are transmitted to terrestrial base station by using VHF band radio signals. As being a terrestrial-based system, the AIS has its limitation in territorial attachment of operating range to the coasts, where the ground transmitter stations are located. One way to deal with the situation is receiving and retransmitting AIS signals from LEO spacecraft. In the long term, global marine surveillance can be accomplished by deploying inexpensive orbital groups of existing or specially constructed AIS spacecraft.

The central issue of space-based AIS is message collision, which occurs when the spacecraft receives simultaneously messages from different ships from close TDMA cells. The amount of lost information in space-based AIS could reach 90%.

The shipborne mobile station AIS broadcasts static, dynamic, voyage information, and also safety messages periodically. Static data (ship IMO number, name, type, etc.) is entered in installation stage. Dynamic data (position, time, course, speed, etc.) is determined by ship measuring equipment. Voyage data (destination, cargo type, waypoints, etc.) is registered before the trip. The safety message is a short text. The AIS equipment broadcasts messages within different time periods depending on the type of information and the ship moving mode.

The operational principle of AIS is shown in fig. 1. AIS carrying ships, situated on the open seas or coastal areas, automatically broadcast standard messages containing ship information in the radio band of marine mobile service. Received AIS information is decoded and visualized on the computer of ships or coastguard, then represented on the digital maps of the sea surface.

Due to the fact that coastal AIS stations cannot receive signals from ships, which are located farther than 75–80 km from the coast, it was suggested to use LEO micro and nanosatellites as the AIS receiver-retransmitters (fig. 2). To date, more than 20 AIS micro and nanosatellites have been launched.

The first obvious problem is low energy of radio channel "ship-satellite", which imposes a restriction on signal reception procedure. Moreover, radiation pattern (RP) of ship antenna allows the connection with spacecraft only by the side lobes. However, that is not a big problem because the low speed of information transmission (9.6 kbit/s) and the narrow bandwidth of GMSK signal ensure a high enough signal-to-noise ratio for reliable reception of information from all ships in the field of view of low-gain antenna on microsatellite. The essential problem is overlapping messages from different ships (collision), which is considered as intersystem interference.

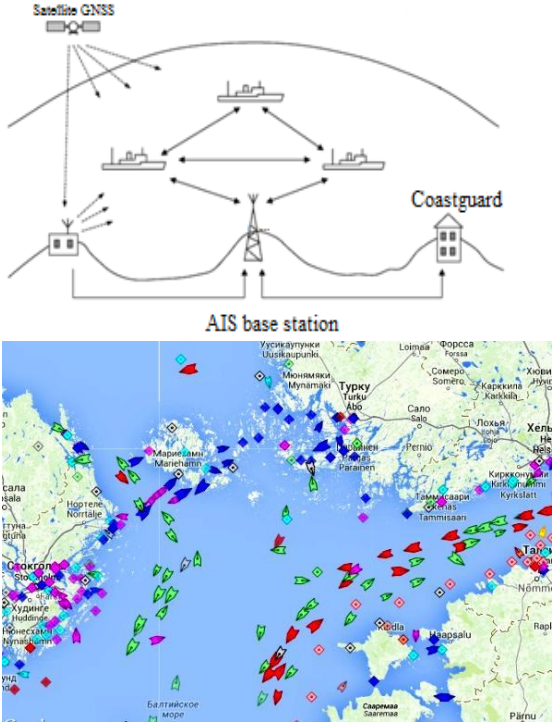


Fig. 1. The operational principle of AIS and the visualization result.

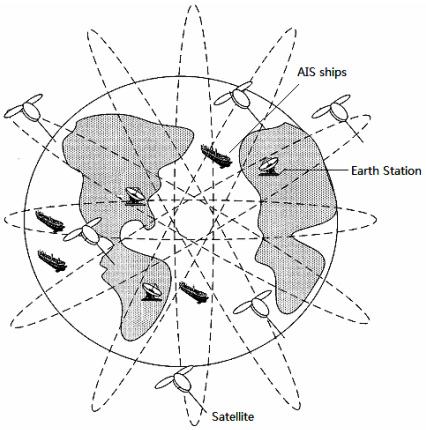


Fig. 2. The principle of retransmission AIS signals from satellites.

When using on ground AIS equipment, the radius of the cell, in which the algorithm SOTDMA operates to prevent message collision [1], does not exceed 75 km. In space-based AIS systems, field of view of the satellite is significantly higher and there is a possibility of overlapping messages from different ships of several cells. Obviously, the more cells covered by the field of view of microsatellite, the higher possibility of collision is. Thus, the main advantage of satellite signal retransmission in S-AIS, expansion of the field of view and increase in the number of physically "be seen" ships, eventually becomes its disadvantage: signals collide and get distorted. As a result, rejection and loss of position and service information (up to 90%) take place in on-board receiver.

On-board Doppler filtering can be used as an alternative way to deal with the collision. By applying narrow-band filter to linear path of satellite AIS receiver, only signals from ships, which are located in traversable band of the filter, can be caught by receiver though the filter bandwidth (fig. 4).

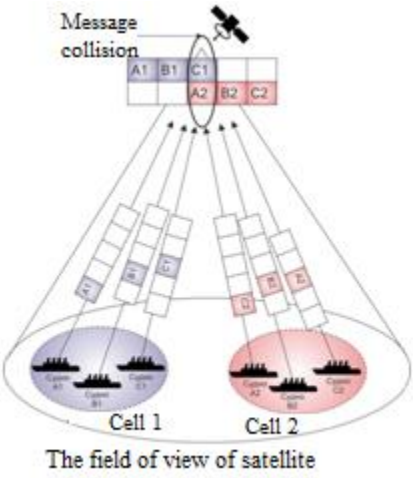


Fig. 3. Package collisions in signal reception in S-AIS.

Signals from other ships in the same field of view are not able to reach linear path, since their carriers are above or below central frequency of filter bandwidth. In this way, the number of interfering

signals decreases significantly. Unlike practical narrowing radiation pattern beam, in this case, the field of view remains wide. Spacecraft, flying on the orbit and shifting the traversable band by its way, can ensure a covering zone inside the “footprint” of the on-board antenna. The possibility that ships, located inside the traversable band from the same inclined distance to spacecraft, simultaneously send their messages in the same time slot is close to zero. Therefore, the problem with collision can be solved. The filtered signal can be processed on-board by AIS receiver. Then, the result is sent to the ground reception station by low-speed channel 9.6 kbit/s.

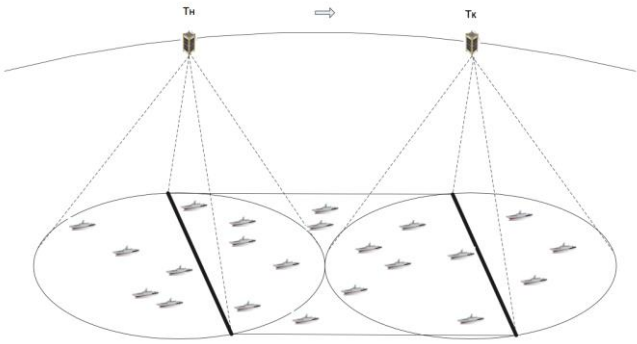


Fig. 4. The operating principle of S-AIS by using Doppler filtering.

## References

1. Space-Based AIS: Contributing to Global Safety and Security. J.S. Cain, E. Meger / ISU 13th Annual Symposium – “Space for a Safe and Secure World”.
2. Establishment And Simulation of the Model for Space-Based AIS. Liu Chang, Cao Ming-zh. Advances in information Sciences and Service Sciences, vol.3, no.22.– pp. 589-596

# METHODS OF COMPUTER-AIDED DESIGN OF SPACE SYSTEMS

Korobeynikov A.[1], Grishentcev A.[1], Fedosovsky M.[1], Velichko E.[2], Golovan O.[2]
[1]ITMO University, St. Petersburg, Russia
[2]Peter the Great St. Petersburg Polytechnic University, St. Petersburg, Russia
[1]E-mail: grishentcev@ya.ru
[2]E-mail: velichko-spbstu@yandex.ru

**Abstract:** This article reviews the basic statements of using apparatus of mathematic Category Theory in the theory of Computer-Aided Design of space systems and conceptual mathematical models (categories) for the phase of conceptual modeling. We present a formal description of a general conceptual representation, which specifies the structure of the system knowledge at different levels of abstraction, and the conceptual view of the subject task, which is determined by the construction of a system of knowledge for a specific subject area.

**Keywords**: Computer-Aided Design, Category Theory, Conceptual modeling.

## Introduction

Main trends of scientific and technological progress require improvement in the qualitative and quantitative characteristics of the projected space systems with an increase in the productivity of a designer and it is one of the main reasons why the theory and methods of Computer-Aided Design (CAD) of space systems have reached a completely new level. It should be noted that the basis for this is the theory of Computer-Aided Design Systems (CAD/CAM) [1–3].

The experience of development and exploitation of CAD/CAM of space systems showed that despite the big costs, connected with the creation of object-oriented CAD/CAM, these systems pay off fairly quickly. This is primarily due to a sharp increase in the productivity of designers and increased quality of projects.

The theoretical basis provides ideological unity, the completeness of solved tasks, the optimality of the separation of functions. The difficulty of its development is explained by the impossibility of solving the problem by simple translating into the "machine language" of traditional methods and design techniques that are focused on the creative, heuristic nature of human work. It is necessary to develop a formalized theory of CAD and operation of space systems, their mathematical models (MM), which play the role of objects of Computer-Aided Design, processing methods of these models focused on machinery, numerical processing and using possibilities of modern applied mathematics. MM and developed techniques must satisfy incompatible requirements of accuracy, versatility, efficiency and simplicity.

It follows that the problem of development of theoretical provisions and development of methods of the theory of computer-aided design object-oriented CAD/CAM is relevant.

**Direction of development of the theory of Computer-Aided Design.**

Nowadays one of the directions of the development of the theory of CAD is the addition methods of mathematical Category Theory (CT) to the theory of CAD [4, 5]. The application of CT makes it possible to present explicitly and compactly all the main points of the theory of CAD. For example, objects of a specific category (formal MM) correspond to technology artifacts. Many technological processes are represented in the form of morphism.

The possibility of generation of sequences of mappings into formal MM was taken as the basic position of the methodology of automation of intellectual labor. These mappings were created in advance and have three levels of abstraction (abstract, object, concrete) of conceptual models.

In this article the results that correspond to the stage of conceptual modeling are presented.

**Conceptual modeling**

The development of conceptual and mathematical models (CMM), or categories for the stage of conceptual modeling, which serves as the basis for representation of the system knowledge design task included the following tasks [6]:

- detection of theoretical, methodological and practical grounds;
- evaluation of the structure and composition of the CMM;
- detection of dependencies that arise during the formation and integration of the CMM.

As a result of the analysis, it was shown that the base of methodological justifications consists of:

- methodology of creation of CAD/CAM, the basis of this is that the quality of automated design of a complex system directly depends on the quality and interaction of design, technological and production environments;
- the structure of the abstract problem of the projected complex system, which is a construction that enables the presentation of any process of Computer-Aided Design with a specified degree of detail;
- knowledge theory.

As a result of the research, the base of theoretical justification was determined:

- mathematical Category Theory
- artificial intelligence theory
- concepts theory.

The results of conceptual modeling of complex systems contain three levels of abstraction— abstract, objective and concrete.

At the abstract level, a general representation of knowledge systems is provided.

At the object level, the subject area is provided by representations of the specificity of knowledge systems.

At a particular level, the factographic information is used.

In this research, the model at any level of abstraction is the main primary information. The models are presented as mathematical categories.

The set of representations of conceptual models consists of two parts: a common conceptual representation (CCR) and the conceptual representation of the subject task (SRST). The structure of the knowledge system at different levels of abstraction is set using the CCR, and the construction of a knowledge system for a particular subject area is determined using the CRST. Conceptual models of all 3

levels of abstraction, which are interconnected by component, belong to the CCR. Conceptual models of the object and concrete levels of abstraction, which are also interconnected by component, belong to the CRST. Each of the representations is considered in more detail below in the article.

CCR can be expressed as

$$CCR = (CCR_1, CCR_2, CCR_3) \quad (1)$$

Here, $CCR_1$ – abstract level, $CCR_2$ – object level, $CCR_3$ – concrete level.

$CCR_i$ at the i-th level of abstraction can be expressed as

$$CCR_i = (Ob\_CCR_i, Mor\_CCR_i) \quad (2)$$

Where, $Ob\_CCR_i$ – the set of models at the i-th level;

$Mor\_CCR_i$ – the set of morphisms at the i-th level;

$Mor\_CCR_i = S\_CCR_i \cup D\_CCR_i$;

$S\_CCR_i = (B\_CCR_i, P\_CCR_i, B\_CCR_i)$ – static relations at the i-th level; $B\_CCR_i \subset Ob\_CCR_i \times Ob\_CCR_i$ – binary relations on $Ob\_CCR_i$;

$P\_CCR_i$ – scheme on $Ob\_CCR_i$;

$BP\_CCR_i \subset P\_CCR_i \times P\_CCR_i$ – binary relations on $P\_CCR_i$; $D\_CCR_i = (V\_CCR_i, BV\_CCR_i)$ – dynamic relations on objects;

$V\_CCR_i$ – restrictions of the i-th level of abstraction;

$BV\_CCR_i \subset V\_CCR_i \times V\_CCR_i$ – binary relations on $V\_CCR_i$.

Restrictions reflect the existence of mappings (morphisms):

$$f : Ob\_CCR_i \to V\_CCR_i \quad (3)$$

The presence of a non-empty ensemble of dependencies for the formation of models is based on the following fundamental positions:

- the directions of the processes of cognition, from specific observations to abstract thinking, from general to selected, from abstract to particular;
- the law of the negation of negation, analysis of specific, synthesis of a single;
- the law of cyclicality of scientific knowledge.

The abstraction mechanism is the base for the existence of relations between the cmm on the ccr of different levels of abstraction.

The transition from the general level to the particular one can be expressed as

$$CCR_i \to CCR_{i+1} \quad (i = 1,2) \text{ i. e.} \tag{4}$$

$$Ob\_CCR_i \to Ob\_CCR_{i+1}, \qquad B\_CCR_i \to B\_CCR_{i+1},$$

$$P\_CCR_i \to P\_CCR_{i+1},$$

$$BP\_CCR_i \to BP\_CCR_{i+1}, \qquad V\_CCR_i \to V\_CCR_{i+1},$$

$$BV\_CCR_i \to BV\_CCR_{i+1}.$$

The methods of relational algebra are the justification of the interconnection of categories at different levels.

A procedure called a "natural connection" is expressed for any objects $A_1$ and $A_2$ as $A = A_1 \bullet A_2$. The use of this operation makes it possible to obtain new information from the initial relations.

From these facts, one may conclude that

$$B\_CCR_{i+1} = Ob\_CCR_i \bullet Ob\_CCR_{i+1} \bullet B\_CCR_i,$$

$S\_CCR_{i+1} = S\_CCR_i \bullet B\_CCR_i \bullet B\_CCR_{i+1}$ – for a set of static operations,

$BV\_CCR_{i+1} = V\_CCR_i \bullet V\_CCR_{i+1} \bullet BV\_CCR_i$ – for a set of dynamic operations.

On this basis, one can define laws of transition from the CMM that belong to the abstract level to the CMM that belong to the object level, and the CMM that belong to the object-level to CMM that belong to a concrete level.

CRST for the n-th task is represented in the following form:

$$CRST(n) = (CRST_2(n), \{CRST_3(n)\}) \tag{5}$$

Here, $CRST_2(n)$ – CMM n-th substantive tasks at the object level of abstraction;

$\{CRST_3(n)\} = (CRST_{31}(n), CRST_{32}(n), ..., CRST_{3k}(n))$ – CMM for the k-th realization of the n-th subject of the task;

$$CRST_2(n) = Ob\_CRST_2(n) \cup Mor\_CRST_2(n) \quad (6)$$

Where, $Ob\_CRST_2(n)$ – subject entities;

$Mor\_CRST_2(n) = S\_CRST_2(n) \cup D\_CRST_2(n)$ – set of morphisms;

$S\_CRST_2(n) = (B\_CRST_2(n), P\_CRST_2(n), BP\_CRST_2(n))$ – set of static relations on objects;

$B\_CRST_2(n) \subset Ob\_CRST_2(n) \times Ob\_CRST_2(n)$ – set of binary relations on $Ob\_CRST_2(n)$;

$P\_CRST_2(n)$ – -set of schemes on $Ob\_CRST_2(n)$;

$BP\_CRST_2(n) \subset P\_CRST_2(n) \times P\_CRST_2(n)$ – set of binary relations on $P\_CRST_2(n)$;

$D\_CRST_2(n) = V\_CRST_2(n) \cup BV\_CRST_2(n)$ – set of dynamic relations on objects;

$V\_CRST_2(n)$ – set of restrictions of object level of abstraction;

$BV\_CRST_2(n) \subset V\_CRST_2(n) \times V\_CRST_2(n)$ – set of binary relations on $V\_CRST_2(n)$.

$$CRST_{3i}(n) = Ob\_CRST_{3i}(n) \cup Mor\_CRST_{3i}(n) \quad (7)$$

Where, $Ob\_CRST_{3i}(n)$ – representatives of subject entities;

$Mor\_CRST_{3i}(n) = S\_CRST_{3i}(n) \cup D\_CRST_{3i}(n)$ – set of morphisms;

$S\_CRST_{3i}(n) = (B\_CRST_{3i}(n), P\_CRST_{3i}(n), BP\_CRST_{3i}(n))$ – set of static relations on objects;

$B\_CRST_{3i}(n) \subset Ob\_CRST_{3i}(n) \times Ob\_CRST_{3i}(n)$ – set of binary relations on $Ob\_CRST_{3i}(n)$;

$P\_CRST_{3i}(n)$ – set of schemes on $Ob\_CRST_{3i}(n)$;

$BP\_CRST_{3i}(n) \subset P\_CRST_{3i}(n) \times P\_CRST_{3i}(n)$ – set of binary relations on $P\_CRST_{3i}(n)$;

$D\_CRST_{3i}(n) = V\_CRST_{3i}(n) \cup BV\_CRST_{3i}(n)$ – set of dynamic relations on objects;

$V\_CRST_{3i}(n)$ – set of restrictions of object level of abstraction, which are representatives of subject dependency;

$BV\_CRST_{3i}(n) \subset V\_CRST_{3i}(n) \times V\_CRST_{3i}(n)$ – binary relations on $V\_CRST_{3i}(n)$.

Dependence of the models can be represented as

$$V\_CRST_2(n) \to \{V\_CRST_3(n)\} \text{ i.e.} \quad (8)$$

$$Ob\_CRST_2(n) \to \{Ob\_CRST_3(n)\},$$

$$P\_CRST_2(n) \to \{P\_CRST_3(n)\},$$

$$BP\_CRST_2(n) \to \{BP\_CRST_3(n)\},$$

$$V\_CRST_2(n) \to \{V\_CRST_3(n)\},$$

$$BV\_CRST_2(n) \to \{BV\_CRST_3(n)\}.$$

The substantiation of the connection between models at different levels is performed using the relational algebra:

$B\_CRST_{3j}(n) = Ob\_CRST_2(n) \bullet Ob\_CRST_{3j}(n) \bullet B\_CRST_2(n)$,

$S\_CRST_{3j}(n) = S\_CRST_2(n) \bullet B\_CRST_2(n) \bullet B\_CRST_{3j}(n)$ – static relations,

$BV\_CRST_{3j}(n) = V\_CRST_2(n) \bullet V\_CRST_{3j}(n) \bullet BV\_CRST_2(n)$ – dynamic relations.

Integration at the object level is represented as

$$Ob\_CRST_2^0 = \cup_n Ob\_CRST_2(n),$$

$$B\_CRST_2^0 = \cup_n B\_CRST_2(n),$$

$$P\_CRST_2^0 = \cup_n P\_CRST_2(n),$$

$$BP\_CRST_2^0 = \cup_n BP\_CRST_2(n),$$

$$V\_CRST_2^0 = \cup_n V\_CRST_2(n),$$

$$BV\_CRST_2^0 = \cup_n BV\_CRST_2(n)$$

Integration at the concrete level is represented as

$$Ob\_CRST_3^0 = \cup_{n,m} Ob\_CRST_{3m}(n),$$

$$B\_CRST_3^0 = \cup_{n,m} B\_CRST_{3m}(n),$$

$$P\_CRST_3^0 = \cup_{n,m} P\_CRST_{3m}(n),$$

$$BP\_CRST_3^0 = \cup_{n,m} BP\_CRST_{3m}(n),$$

$$V\_CRST_3^0 = \cup_{n,m} V\_CRST_{3m}(n),$$

$$BV\_CRST_3^0 = \cup_{n,m} BV\_CRST_{3m}(n).$$

**Conclusions**

The regularities of the mappings are based on the identity of the use of abstractions during the process of forming links at the CMM at the same level of abstraction.

Description of the CCR and CRST allows us to solve the problems of systematization and description of models as specific design tasks, and integration of data representations into a single whole.

Description of the relationships between CMM CCR and CRST on the basis of the revealed regularities of the display provides the ability to:

- limit many kinds of connections and dependencies, if there is a verbal symbolic representation;
- apply semantic addition to formalized symbolic presentation of subject tasks, and make it full.

In the process of research, the modeling methods discussed in this article were implemented in the MATLAB and Maple systems [7–

10]. The developed software was used to solve various problems related to the design of systems with which space is explored [11–13].

## References


1. Grishentsev A.Yu., Guryanov AV, Tushkanov EV, Shukalov AV, Korobeinikov AG Virtualization and software in computer-aided design: Tutorial, SPb: ITMO University, 2017. - 60 p.
2. Grishentsev A.Yu., Guryanov AV, Kuznetsova OV, Shukalov AV, Korobeinikov AG Mathematical support in computer-aided design systems. - St. Petersburg: ITMO University, 2017. - 88 p.
3. Gatchin Yu.A., Korobeinikov AG Design of integrated automated technological complexes. - SPb: SPb GITMO (TU), 2000. - 171 p.
4. Guryanov AV, Korobeinikov AG, Fedosovsky ME, Shukalov AV, Zharinov I.O. Automation of the design of complex technical complexes on the basis of category theory // Questions of defense technology. Series 16: Technical Countermeasures to Terrorism - 2017. - № 3-4. - p. 9-16.
5. Korobeynikov AG, Fedosovsky ME, Gurjanov AV, Zharinov IO, Shukalov AV Development of the Conceptual Modeling Method for Solving the Tasks of Computer-Aided Design of the Difficult Technical Complexes on the Basis of the Category Theory // International Journal of Applied Engineering Research ISSN 0973 -4562 Volume 12, Number 6 (2017) p. 1114-1122.
6. Korobeinikov AG A method of conceptual modeling in problems of designing systems for collecting and processing information, Izv. Institutions of Higher Education, T. 44, № 2, 2001. - p. 8-13.
7. Korobeinikov AG Development and analysis of mathematical models using MATLAB and MAPLE // St. Petersburg: St. Petersburg National Research University of Information Technologies, Mechanics and Optics. - 2010. - 144 p.
8. A. G. Korobeinikov, A. Yu. Grishentsev. Development and research of multidimensional mathematical models using computer algebra systems. - SPb: SPbSU ITMO, 2014. - 100 p.
9. Korobeinikov AG Designing and research of mathematical models in MATLAB and Maple environments. - SPb: SPbSU ITMO, 2012. - 160 p.
10. Grishentsev A.Yu., Korobeinikov A.G. Statement of the Optimization Problem for Distributed Computing Systems // NB: Software Systems and Computational Methods. - 2013. - № 4. - p. 370 -375.
11. Grishentsev A.Yu., Korobeinikov A. G. Designing and technological preparation of networks of vertical sounding stations // SPb: University

ITMO. Scientific and technical herald of information technologies, mechanics and optics. - 2013. - № 3 (85). - p. 61 - 66
12. Grishentsev A.Yu., Korobeinikov A.G. An inverse problem of radio-frequency sounding of the ionosphere. // Journal of Radioelectronics. 2010. № 10. p. 6.
13. Grishentsev A.Yu., Korobeinikov A.G. Development of a model for the distribution of current densities during excitation of the ionosphere by high-frequency irradiation // Izvestiya Vysshikh Uchebnykh Zavedenii. Instrument making. 2010. P. 53. № 12. p. 41-47.

## AN ANALYSIS OF SOME WAVELET FUNCTIONS IN TERMS OF BROADBAND SYSTEMS SYNTHESIS

Grishentcev A.U.[1], Korobeynikov A.G.[1], Velichko E.N. [2], Putintseva M.V.[2]
[1]ITMO University, St. Petersburg, Russia
[2] Peter the Great St. Petersburg Polytechnic University, St. Petersburg, Russia
[1] E-mail: grishentcev@ya.ru

**Abstract**: This article deals with the issues of application of some wavelet functions for a wideband signal design on the basis of matrices of particular form of the autocorrelation function. The elements of such matrices are complex numbers with the module equal to one. The research objects are wavelet functions and wideband signals obtained on the basis of wavelet analysis. Numerous studies have displayed that rather explicit results of wideband signal design allow to receive following continuously differentiable wavelet functions: the b-spline wavelet, Morlet wavelet.

**Keywords**: wireless broadband connectivity, digital signal processing, wavelet functions.

### Introduction

Methods and broadband radio communication systems in comparison with a set of modern technologies have a rather long history. The first receptions and transmissions were carried out for the wideband signals being of spark nature, and meet the criteria of the

wideband signal TW>1, where T is a period, W is an emission frequency band (e.g., Popov lightning detector, Hertz spark-gap radio transmitter, Marconi transceivers and similar ones.) The subsequent development of a wireless communication, up to 1960s, was geared primarily towards narrowband signals. But unlikely, since the mid-twentieth century achieved technological capabilities and the radio communication theory allowed the implementation of the first spread-spectrum systems, mainly for the military radio communication and radio ranging use [1]. The development of outer space communication, as well as the necessity of rendering adequate transmitted data protection against the backdrop of the digital technologies developments and sustained growth of loading of an air fostered the proliferation of research and ubiquitous implementation of items of the spread-spectrum communication. Nowadays, the high-speed computing tools of signal processing (DSP digital signal processor) provide a significant potential for communication systems. The effective control of a spectrum with an equal signal drive distribution in time is a key concern of synthesis of the broadband signals (BS).

The effective control of a spectrum with an equal signal drive distribution in time is a key concern of synthesis of the broadband signals (BS).

The theoretical part of this study is devoted firstly to the exploration of the peculiarities of the spread-spectrum signal design on the basis of matrices with a particular form of an autocorrelation function using following continuously differentiable wavelet functions: b-spline wavelet, Morlet wavelet.

The main goal of the present work is to analyse the issue of a wideband signal design using wavelets on the basis of complex matrices with a particular form of an autocorrelation function (ACF). These groups of matrices were first considered by authors of this work [2–4]. ACF of such matrices has considerably larger size of the central element in comparison with side lobes. The distinctive feature of complex matrices and the ACF special form – value of complex elements. In this study [3] the possibility of division of complex-valued signals into imaginary and real components was shown by methods of digital processing on a receiving part. In research [5] the selection of the optimized shape of wavelet functions in the ACF [6,7]

was made. We opted for the b-spline wavelet (bSW) and Morlet wavelet (MW).

Some analytical wavelet functions characteristics

Equation of a class of compactly supported normalized [8–10] b-spline wavelets is defined as:

$$\varphi_{\mathrm{bSW}}(t) = \sqrt{\frac{f_b}{\pi}}\left(\mathrm{sinc}(\frac{f_b t}{Q})\right)^Q e^{\mathrm{j}2\pi f_c t}, \quad (1)$$

where $f_b$ is bSW frequency band; $f_c$ is the center frequency of the bSW in Hz (i.e., the frequency corresponding to the spectral peak of the wavelet); $Q$ is a damping ratio parameter of sinc-function ($Q = 1,2,3, ...$).

Spectrum of the bSW [5] within the interval $t \in [-T_{\mathrm{bSW}}/2, T_{\mathrm{bSW}}/2]$, differ substantially from spectrum within the interval $t \in [-\infty,\infty]$. It can be determined as:

$$\sqrt{\frac{f_b}{\pi}}\sqrt{\frac{1}{2\pi}}\int_{-\frac{T_{\mathrm{bSW}}}{2}}^{\frac{T_{\mathrm{bSW}}}{2}} \mathrm{sinc}(f_b t)\, e^{\mathrm{j}t(2\pi f_c t-\omega)} dt = $$

$$= \frac{1}{\pi\sqrt{2f_b}}\left(\int_0^{\frac{T_{\mathrm{bSW}}}{2}(f_b+2f_c\pi-\omega)} \frac{\sin(\mathrm{t})}{\mathrm{t}}\mathrm{dt} + \right.$$

$$\left. \int_0^{\frac{T_{\mathrm{bSW}}}{2}(f_b-2f_c\pi+\omega)} \frac{\sin(\mathrm{t})}{\mathrm{t}}\mathrm{dt}\right). \quad (2)$$

Equation of a class of compactly supported normalized WM is defined as:

$$\varphi_{\mathrm{WM}}(t) = \sqrt[4]{\frac{2}{\pi f_b}} e^{\mathrm{j}2\pi f_c t - \frac{t^2}{f_b}}, \quad (3)$$

where $f_{\mathrm{b}}$ is WM frequency band in Hz; $f_{\mathrm{c}}$ is the center frequency of the WM in Hz.

Spectrum of the WM [5] in the bounded interval $t \in [-T_{\mathrm{WM}}/2, T_{\mathrm{WM}}/2]$ can be determined as:

$$Y_{\mathrm{WM}}(\mathrm{j}\omega) = F\{\varphi_{\mathrm{WM}}(t)\} = \sqrt[4]{\frac{2}{\pi f_b}}\sqrt{\frac{1}{2\pi}}\int_{-\frac{T_{\mathrm{WM}}}{2}}^{\frac{T_{\mathrm{WM}}}{2}}\left(e^{j2\pi f_c t-\frac{t^2}{f_b}}\right)e^{-j\omega t}dt = \mathrm{j}\sqrt[4]{\frac{f_b}{2\pi^3}}e^{-\frac{1}{4}f_b(\omega-2\pi f_c)^2}\left(\int_0^{\frac{2f_bf_c\pi-\mathrm{j}T_{\mathrm{WM}}-f_b\omega}{2\sqrt{f_b}}}e^{-t}dt - \int_0^{\frac{2f_bf_c\pi+\mathrm{j}T_{\mathrm{WM}}-f_b\omega}{2\sqrt{f_b}}}e^{-t}dt\right). \quad (4)$$

**The synthesis of the signaling messages**

Firstly it is necessary to define the wavelet function $\varphi(t, f_c(y))$ of time $t$, as superposition of functions $\varphi(t)$ (wavelet) and $f_c(y)$ (function of carrier frequency). Then we can write the equation:

$$s(t) = \sum_{y=0}^{Y-1}\begin{pmatrix} Re\left[M[y][\left\lfloor\frac{t}{T_W}\right\rfloor]\right]Re[\varphi\left(f_c(y+1)(t-\frac{T_{\mathrm{W}}(1-2x)}{2}),f_c(y)\right)] + \\ +\mathrm{j}\cdot Im\left[M[y][\left\lfloor\frac{t}{T_{\mathrm{W}}}\right\rfloor]\right]Im[\varphi\left(f_c(y+1)(t-\frac{T_{\mathrm{W}}(1-2x)}{2}),f_c(y)\right)]\end{pmatrix}$$

Full signal duration $s(t)$ can be determined as: $T = XT_{\mathrm{w}}$, where $X$ is the column dimension of matrix **M**; $[-T_{\mathrm{w}}/2, T_{\mathrm{w}}/2]$ is the interval of the wavelet function. As a synthesizing matrix, we use matrix $MC_9$ [2] with the size equal to 2×4:

$$\mathbf{M} = \begin{pmatrix} -\frac{\sqrt{2}}{2}+\mathrm{j}\frac{\sqrt{2}}{2} & 1 & \frac{\sqrt{2}}{2}+\mathrm{j}\frac{\sqrt{2}}{2} & \frac{\sqrt{2}}{2}-\mathrm{j}\frac{\sqrt{2}}{2} \\ -\frac{\sqrt{2}}{2}-\mathrm{j}\frac{\sqrt{2}}{2} & -\mathrm{j} & 1 & 0 \end{pmatrix},$$ e.g., synthesize signals using bSW, WB and SC, on the basis of matrix **M** (fig.1) either. Synthesis and signal analysis were carried out in the environment of MatLab [11].

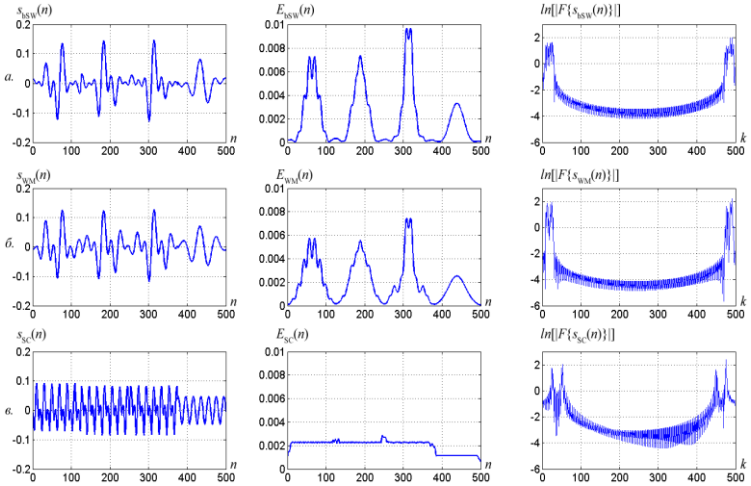

Fig.1. Comparison of signals, frequency content and averaged energy densities.

The first column of the first row (fig.1, *a*), contains signal message $s_{bSW}(n)$, obtained on the basis of bSW when $\frac{T_{\text{bSW}}}{2} = 2.85$, $f_b = 1$, $Q = 1$; the second column displays diagram $E_{bSW}(n)$ – averaged density of the energy distribution over $n$; in the third column it is reported that $\ln(|S_{bSW}(k)|) = \ln(F\{|s_{bSW}(n)|\})$. Similar charts were plotted for the signals synthesized on the basis of WM when $\frac{T_{\text{WM}}}{2} = 1.517$ and $f_b = 1$, (fig.1, *b*) (second line), as well as SC (fig.1, *c*) (third line), for the signal synthesized on the basis of matrix **M** using harmonic functions.

Figure (fig.1) analysis allows drawing following conclusions: when using wavelets (fig.1, lines a, b) high-frequency components of the signals decreasing more than threefold, in comparison with the signals, synthesized with the help of harmonic functions (fig.1, line c), it means that the application of wavelets redounds improvement of signal spectrum control. The best possible pattern of energy distribution enables to receive the signal, synthesized with the help of harmonic functions (fig.1, line c).

**Conclusions**

A larger time–frequency resource is required to provide equal peak signal-to-noise ratio, while transmitting signals that were synthesized with the help of wavelets and harmonic functions. It is noteworthy that the presence of ripple of energy distribution is not conducive to a signal identification, hidden in the airwave noise (subnoise signals). Thus, the application of wavelet functions for the organization of the hidden subnoise channels of a wireless communication is inexpedient. The wavelets for the synthesis of the broadband signals can find application in the systems in which concealing the fact of data transmission (steganography) is implemented not on the subnoise concealment, i.e. due to decrease of the signal level, but through other principles, including the use of a spatial time-frequency resource.

**References**

1. Noise-shaped signals in data-transmission systems. Edited by V. B. Pestryakova // M.: Sov. radio, 1973 – 424 p.
2. Grishentcev A.Yr., Korobeynikov A. G. Retrieval algorithm, some properties and application of complex-valued matrices for steganography and synthesis of the broadband signals // *Journal of Radio Electronics*. № 5, 2016. URL: http://jre.cplire.ru/jre/may16/11/text.pdf
3. Grishentcev A.Yr. On method of the separation in time of the autocorrelation of the harmonic components of wideband signals // *Journal of Radio Electronics*. № 9, 2016. URL: http://jre.cplire.ru/jre/sep16/2/text.pdf
4. Grishentcev A.Yr., Korobeynikov A. G., Velichko E. N., Nepomniashchaia E. K., Rosov S. V. Binary matrix synthesis for broadband communication signal shaping // Radiotechnics. 2015. № 9. P.: 51-58 T.
5. Grishentcev A.Yr., Korobeynikov A. G. Application of wavelets for broaband signals generation // Izv. vuzov. Priborostroenie. 2017. Vol. 60, № 8. P.: 712-720 T.
6. Grishentcev A.Yr., Korobeynikov A. G. On reduction of space dimension at digital signals correlation and convolution // Izv. vuzov. Priborostroenie. 2016. Vol. 59, № 3. P.: 211—218 T.

7. Dyatlov A. P., Kylbikayan B. H. Correlation processing of the broadband signals in the radiomonitoring automated complexes // M.: Gorachaya linya-Telecom, 2014. – 332 p.
8. Brayn V. O., Dolgyshin V. P., Loza V. N., Pampyha I. V. Research of possibilities and methods characteristics of abatement of noise during signal synthesis, based on wavelet technology // *Journal of Radio Electronics*. № 7, 2014. URL: http://jre.cplire.ru/win/jul14/6/abstract.html
9. Smolenintsev N. K. Wavelet analysis in MatLab // M.: DMK Press, 2010. – 448 p.
10. Bansai M., Sethi D. Denoising of speech and ecg signal by using wavelets // Lambert Academic Publishing, 2012. – 64 p.
11. MatLab, The MathWorks, Inc. URL: http://www.mathworks.com/

## THE ARCHITECTURE PAYLOAD "S-AIS" FOR SERIES OF EXPERIMENTS

Malygin D.V., Popov E.N., NguyentanH.P.
Peter the Great St.Petersburg Polytechnic University, St. Petersburg, Russia
office@spbstu.ru

**Abstract:** The paper considers a technology of design and architecture of the onboard communication system "S-AIS" for a series of experiments on processing signals received from navigational equipment of ships.

**Keywords:** smal spacecraft, nanosatellite, picosatellite, platform, cubesat, onboard communication system, ais

In order to examine the message collision preventing method, based on Doppler filtering [2], in space-based AIS system, a series of space experiments is planned to be conducted on Cubesat-3U format satellite developed in the laboratory “Space communication technologies” of Peter the Great St. Petersburg Polytechnic University.

The equipment, needed for the experiments, contains the following components: spacecraft in Cubesat 3U form; on-board AIS

receiver; ground station, consisting of rotating antenna system and retransmission point, for controlling spacecraft and receiving AIS information.

For controlling the satellite and receiving targeted information, a radio-technical complex, which consists of an ISM-band command-telemeter station and high-speed reception station working in L-K bands, has been developed. Controlling center is located in SPBPU. The complex has the following characteristics:

- Command radio link: 145/435 MHz
- Information transmission speed: 9.6 kbit/s
- Package protocol for data transmission: AX.25
- Modulation method: AFSK.

By examining the hardware realized methods, which allow us to implement Doppler filtering AIS signal, it is shown that the implementation by direct methods is impossible because there is no practicable bandpass filters with the required bandwidth (4.8 kHz) and central carrier frequency (161.975 MHz). Therefore, one possibility is offsetting the central frequency to the lower frequency and recovering it later.

A scheme (fig. 1) is suggested to carry out the experiment, which provides the data in two conditions: using filter and not using.

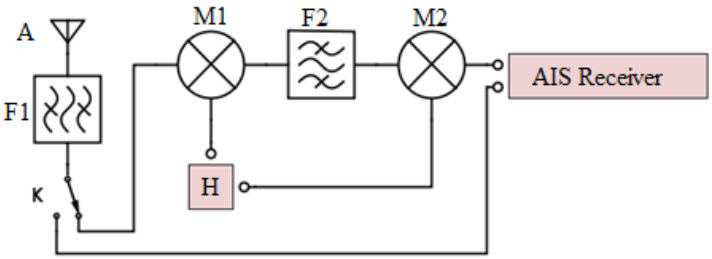


Fig. 1. Structure scheme of targeted equipment.

The signal received by the antenna A passes the primary filtering process (F1). An electromechanical switch is needed to consecutively realize the AIS signal reception in the conditions of using Doppler filtering and not using (when the signal is get on the AIS receiver directly after primary filtering). In the case of using

Doppler filtering, after primary filtering, the signal gets on the mixer 1, in which the frequency offsetting takes place by using the heterodyne H with a fixed frequency. Then, the signal passes the bandpass filter F2, which is configured on shifted central frequency and has fixed bandwidth, and gets recovered in mixer M2. The model BRTK "Polimorf", made by OOO "Laboratory Astronomikon", is used as an AIS receiver. The structural scheme of receiver is shown in Fig. 2.

The content of space experiment is carrying out the sessions of AIS message reception from zones with the same intensity of ships in 2 conditions: using Doppler filtering and not using. Then, the number of detected ships in these cases is compared. In this way, the experiment program provides the information about zones of view, the order of switching the onboard AIS equipment with and without the Doppler filtering, and the procedure of processing the information obtained by considering the data.

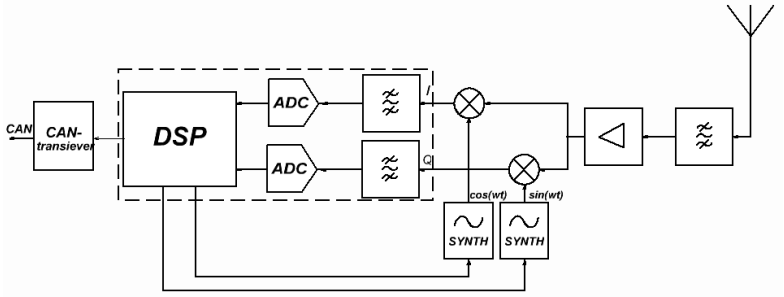


Fig. 2. The structural scheme of the AIS receiver.

Based on the analysis of the available information about the density of shipping traffic, it was found that a part of the Atlantic Ocean, which is enclosed by the northwestern shore of Africa and the eastern shore of the North America, is a potential zone to conduct the experiment. The potential area allows us to realize collecting information about positions of ships in two rounds. In one round, the switch K is turned on and activates the Doppler filtering process.

The process is continued by counting the number of ships, detected in the first and the second rounds, in the crossing area of the field of view of spacecraft. If the number of detected ships in crossing area with Doppler filtering is 3-4 times higher than without filtering,

the experiment will be considered successful and the novel method against collision could be recommended to be used in domestic space-based AIS systems.

## References

1. Space-Based AIS Receiver for Maritime Traffic Monitoring Using Interference Cancelattion. O.F.Haakonsen Dahl / NTNU, 2006.
2. An analysis of AIS signal collisions. J.K.E. Tunaley.

# POLARIMETRY OF ATMOSPHERE: EVIDENCE FROM CONDENSED MEDIUM

Trubin P.K., Velichko E.N., Aksenov E.T.
Peter the Great St. Petersburg Polytechnic University, St. Petersburg, Russia;
E-mail: ptk4815@yandex.ru

**Abstract:** Optoelectronic system for polarization measurements is presented. The system consists of channel of analysis that is based on the method of polarization visualization and of analysis of spatial distributions of polarized light back scattered by the turbid medium. The results which were obtained and developed methods can be used in lidar applications.

**Keywords:** polarized light, back scattering, air pollution, biotissue.

## Introduction

Nowadays one of the most socially important problem is the problem of air pollution. The analysis of nature of the pollution can be carried out rather efficiently by laser optoelectronic methods. There were developed the technologies on the basis of lidar probing that allowed to determine remotely the spatial contamination level.

There such is a wide variety of lidar systems, all of them are differ in the number of used lasers and the methods of detecting aerosol particles. They feature systems, based upon polarized measurements by which it is possible to define the type of aerosol

particles and, moreover, assess the spatial orientation of the scattering particles [1].

**Theory**

The functional principle of such systems is as follows. Partially polarized light can be most fully described within the Stokes-Mueller matrix formalism [1–2]. The condition of polarization of back dispelled signals resulting from scattering of the probing bunch in the atmosphere including on an atmospheric aerosol of various nature, is characterized generally by degree of a depolarization of the accepted radiation. The polarization of light scattered from different atmospheric aerosols can be characterized by the depolarization ratio of the incoming radiation. Backscattering matrix of the studied aerosols is measured by changing the polarization mode of the probe radiation, as well as using the polarimeter at the input of the lidar receiving system. The type of particles (spherical or non-spherical) and degree of spatial orientation (for example, of crystalline microparticles in the clouds of the upper tier) are determined by the structure of the backscattering matrix and ratio of individual elements. Since this matrix carries comprehensive information of the condition of the aerosol ensemble, thus, observing changes in matrix elements in time and space, it is possible to obtain data not only about the aerosol microstructure at a specific altitude, but also to estimate the parameters of external physical fields. Regular aerosol observations in the upper layers of the atmosphere allow promptly to detect the appearance of another type of aerosol above the observation point, that can give information about the atmospheric circulation and the trans-regional weather travel.

The studies in this field are of prime importance due to wide usage of optical models, that are used in calculation programs of the atmospheric radiation balance. Those programs use optical models in which the orientation property of non-spherical cloud particles, for example, ice crystals in cirrus clouds, is not taken into account. That's the reason why the model is used, at best, assuming a chaotic orientation of particles, which leads to a decrease in the accuracy of the calculations.

The enhancing of the optical model of clouds of the upper tier levels is extremely important for understanding the key issues of global climate change on our planet.

## Methods

The expansion and perfection of the polarimetric method of polarized light scattered from the object is connected with the increasing range of the materials of the investigated objects from gaseous to solid. In this paper, a technique for analyzing polarization parameters of light backscattered from a quite turbid media, a biological tissue is developed. In particular, the possibilities of the method of polarization imaging [3–4] of the subtissue were investigated, as well as the effect of absorption of multiply scattering media on the degree of polarization. Biotissues were chosen as the research objects.

These both methods are based on the analysis of spatial distributions backscattered from the media, polarized light. As a result, the image of a subtissue of increased contrast was obtained. The technique of correlation analysis of polarized images was developed, the parameters of residual polarization for the object were determined.

## Conclusion

On the basis of the results, the design of the polarimetric sensor is currently being developed and tested. It allows us to register the condition of both the surface tissues of the human body and intracavitary tissues, for example, of the oral cavity.

The results obtained and the methods developed can be used in lidar applications. Thereafter the techniques will be improved and we will be able to receive completely new information.

## References

1. Pal S.R., Carswell A.I. Polarization anisotropy in lidar multiple scattering from atmospheric clouds. // Appl. Opt. Vol. 24, No.21, 1985
2. Samokhvalov I.V. Detection of crystalline particles in the atmosphere by the method of polarization laser sensing. National Research Tomsk State University, Russia, 2013

3. Tuchin, V. V., Wang L. L., Zimnyakov D. A.,2006, Optical Polarization in Biomedical Applications, Springer, New York.
4. Zimnyakov D. A. and Sinichkin. Y.P. , 2000, A study of polarization decay as applied to improved imaging in scattering media , Journal of Optics A: Pure and Applied Optics, Vol. 2,pp. 200-208.

# Contents

**Section Astrophysics and Cosmology ..... 3**

Yeghikyan, A.G. The origin of life from the astrophysical point of view ..... 3

Telikova K.N., Balashev S.A., Shternin P.S. An estimation of the temperature-density relation in the early universe ..... 10

Kropotina J., Bykov A., Krassilchtchikov A., Levenfish K. Hybrid modeling of quasiparallel collisionless shocks in two-species plasmas: trajectories of suprathermal particles ..... 16

Kalyashova M.E., Bykov A.M., Osipov S.M. Modeling of x-ray stripes in tycho's supernova remnant ..... 21

Tsybin O.Yu. Analytical time-dependent instantaneous frequency theory of charged particle motion in electromagnetic fields in space ..... 26

**Section Tools of Modern (Radio) Astronomy ..... 31**

Amelchenko A.O., Karpichev A.S. A synchronization of sessions of vlbi-observations by means of the global navigation satellite systems ..... 31

Khachatryan A., Sargsyan A. A research of different deformations influence on rot-54/2.6 radio telescope antenna ..... 35

Drozhzhov K.A., Ilin G.N., Ivanov S.I. A development of signal processing algorithm for water vapour radiometer operating in intensive precipitation ..... 48

**Section Remote Sensing System and Spacecraft Technologies ..... 53**

Dyubo D., Tsybin O.Yu. A novel photodiode in on-board micro receiver in 400-800 nm range ..... 53

HUO Jun-hai, MENG Tao, JIN Zhong-he Relative orbit and attitude coupled control based on sliding-mode variable structure control ..... 57

Sagitov E.A., Lezhennikova K.A., Semenov V.V., Fatkhutdinova L.I. A relative influence of low-frequency and microwave radio-optical resonances in alkali atoms vapor ..... 64

**Section Satellite Communications, Navigation Systems and Technologies ..... 71**

Chen Lu, Wang Hao, Wang Bendong A new fast algorithm for micro-satellite attitude determination based on panoramic annular lens.....71
Tsybin O. Yu. Selected challenges in space ion physics research and technology .....78
Petrov A.A., Davydov V.V., Popov A.S., Lukashev N.A. Cesium atomic clock for glonass satellite navigational system .....83
Sagitov E.A., Ermak S.V., Semenov V.V. A short-scale quantum frequency standard based on two quantum magnetometers for on-board applications .....89
SUN Shu-jian, MENG Tao, JIN Zhong-he A review on the development of micro-nano satellite constellation and formation flying technologies .....94
**Section Signal Processing, Systems Simulation and Complex objects control for Space Applications .....102**
Dubov V.V., RoshchupkinS.P. An influence of strong pulsed laser fields on the resonant processes of quantum electrodynamics .....102
HUANG Jia-jun, ZHANG Chao-jie, JIN Zhong-he, XU Jiu-Ling I/Q imbalance calibration using a genetic algorithm approach .....111
Myazin N.S., RukinE.V., Davydov V.V., Yushkova V.V. A new nondestructive method for determining the composition of components in biological objects in express mode.....116
Xu Jiuling, Zhang Chaojie, Wang Chunhui, Huangjiajun Optimal balanced sinr tracking for multi-channel cdma based ranging system .....123
ZHANG Gu-hong, ZHAO Chang-chang, YU Zhuo-qun, JIN Zhong-he Simulation of qpsk large frequency offset carrier recovery based on fft .....132
Malygin D.V., Popov E.N., Nguyentan H.P. A structure of experiment on processing signals received from ship navigation equipment by means of “s-ais” payload .....141
Korobeynikov A., Grishentcev A., Fedosovsky M., Velichko E., Golovan O. Methods of computer-aided design of space systems.....147

Grishentcev A.U., Korobeynikov A.G., Velichko E.N., Putintseva M.V An analysis of some wavelet functions in terms of broadband systems synthesis. ..... 156

Malygin D.V., Popov E.N., Nguyentan H.P The architecture payload "s-ais" for series of experiments ..... 162

Trubin P.K., Velichko E.N., Aksenov E.T. Polarimetry of atmosphere: evidence from condensed medium..... 165

# The First Joint International Conference on Astrophysics for Young Scientists

October 3–7, 2017, Byurakan

Book of proceedings

Sent for the press 20.11.2017. Format 60×84/16. Digital press.
conv. pr. sh. 10,75. pressrun 29 cop. Order 16084b.
It is printed from a ready dummy,
provided by organizing committee of a conference,
in the Publishing center of the Polytechnical university.
Russia, 195251, St.Petersburg, Polytechnicheskaya, 29
Tel.: (812) 552-77-17; 550-40-14.